INNER-SURF AND SWASH-ZONE HYDRODYNAMICS AND SEDIMENT TRANSPORT PROCESSES DURING ACCRETIVE CONDITIONS AND LOCAL WIND FORCING

by

Patricia Chardón-Maldonado

A dissertation submitted to the Faculty of the University of Delaware in partial fulfillment of the requirements for the degree of Doctor of Philosophy in Civil Engineering

Fall 2016

INNER-SURF AND SWASH-ZONE HYDRODYNAMICS AND SEDIMENT TRANSPORT PROCESSES DURING ACCRETIVE CONDITIONS AND LOCAL WIND FORCING

by

Patricia Chardón-Maldonado

Approved: ____
Harry W. Shenton III, Ph.D.
Chair of the Department of Civil and Environmental Engineering

Approved: ____
Babatunde A. Ogunnaike, Ph.D.
Dean of the College of Engineering

Approved: ____
Ann L. Ardis, Ph.D.
Senior Vice Provost for Graduate and Professional Education

I certify that I have read this dissertation and that in my opinion it meets the academic and professional standard required by the University as a dissertation for the degree of Doctor of Philosophy.

Signed: ____
Jack A. Puleo, Ph.D.
Professor in charge of dissertation

I certify that I have read this dissertation and that in my opinion it meets the academic and professional standard required by the University as a dissertation for the degree of Doctor of Philosophy.

Signed: ____
Jens Figlus, Ph.D.
Member of dissertation committee

I certify that I have read this dissertation and that in my opinion it meets the academic and professional standard required by the University as a dissertation for the degree of Doctor of Philosophy.

Signed: ____
Alec Torres-Freyermuth, Ph.D.
Member of dissertation committee

I certify that I have read this dissertation and that in my opinion it meets the academic and professional standard required by the University as a dissertation for the degree of Doctor of Philosophy.

Signed: ____
Tian-Jian Hsu, Ph.D.
Member of dissertation committee

I certify that I have read this dissertation and that in my opinion it meets the academic and professional standard required by the University as a dissertation for the degree of Doctor of Philosophy.

Signed: ______________________________

James T. Kirby, Ph.D.
Member of dissertation committee

ACKNOWLEDGEMENTS

First, I thank God, for giving me the desire, will, ability, guidance, hope, and drive along this fructiferous journey.

I would like to thank my advisor, Jack A. Puleo, who gave me an outstanding opportunity to fulfill one of my goal, obtain a PhD. I am immensely grateful for the many enlightening discussions, the advice, and all the opportunities he has given me to develop myself professionally through field work, travel, and teaching. I will always cherish the countless great memories during these three years, especially during my field work in the freezing cold (*no bueno*). His level of care, dedication and interest is unsurpassed by anyone I have ever met in the academia. It has been an honor to work with him and to learn from him. As a graduate student, I could not have asked for a better advisor. I also want to thank my co-advisor, Jens Figlus, for the advice and support during my PhD. I must also thank my doctoral committee members, Alec Torres-Freyermuth, Tom Hsu, and James Kirby for all the help and input in my research.

I am immensely grateful to my soon-to-be husband, Francisco, for his indefatigable encouragement and support. Throughout my PhD adventure we have shared all my ups and downs, my doubts and triumphs. He supported me during my time at UD, regardless of the fact that my stress levels spilled over to him. Special thanks to my mother, father and sister, though being so far away from home, their unconditional support and love kept me going through this dissertation process.

Thanks to the best friends I could ever ask for, who made my time in Newark unforgettable, Ryan, Nick, Babak, Yaroo, and Dimitrios... you guys are the best!. Lastly but not least, many thanks also go to my friends, fellow students and colleagues who help me during the field experiments and to the staff at the Ocean Engineering

Lab at the University of Delaware and at Universidad Nacional Autónoma de México for the great work experience.

This work was supported by the National Science Foundation, University of Delaware, University of Texas A&M at Galveston, and Instituto de Ingeniera UNAM.

TABLE OF CONTENTS

LIST OF TABLES

LIST OF FIGURES

LIST OF SYMBOLS AND ABBREVIATIONS

ϵ_b	Efficiency bed load factor
ϵ_s	Efficiency suspended load factor
η	Free surface elevation
κ	von Karman constant
ρ	Fluid density
τ_i	Bed shear stress
ε	Turbulence dissipation rate
ξ	Iribarren number
a	Swash excursion length
C	Empirical constant
c_f	Friction coefficient
$D(z_s, r, t)$	Structure function
D_p	Wave direction
d_{50}	Median grain size
dz	Vertical elevation difference between beach profiles
dz_s	Elevation difference above the bed

H_s	Significant wave height
h_{OBS}	Elevation of the highest submerged OBS
i	x and y component
k_s	Bed roughness
m	Slope of the least squares fit
p	Pressure
Q_i	Suspended sediment transport rate
r	Separation distance between velocity bins in the probe
R^2	Correlation coefficient
$R_{2\%}$	2% Runup Exceedence
t	Time
T_p	Wave period
$tan\beta$	Foreshore slope
U	Free stream or depth-average flow velocity
u_*	Friction velocity
U_{10}	Wind speed
U_θ	Wind direction
w'	Fluctuating vertical velocity component
z_0	Bed roughness
z_s	Height above the bed

A	Decorrelation of the velocity field
Fr	Froude number
f	Frequency
h	Water depth
MSL	Mean sea level
N	Doppler noise
SSC	Suspended sediment concentration
u	Cross-shore flow velocity
v	Alongshore flow velocity
w	Vertical flow velocity
x	Cross-shore coordinate
y	Alongshore coordinate
z	Vertical coordinate
ACVP	Multi-frequency Acoustic Concentration and Velocity Profiler
ADCP	Acoustic Doppler Current Profiler
ADPV	Acoustic Doppler Profiling Velocimeter
Aquadopp	Aquadopp Acoustic Doppler Current Profiler
CCM	Conductivity Concentration Meter
CCP	Conductivity Concentration Profiler
EMCM	Electromagnetic Current Meter

FOBS	Fiber Optical Backscatter Sensor
GPS	Global Positioning System
LDA	Laser Doppler Anemometry
LIDAR	Light Detection and Ranging
LIF	Laser-induced Fluorescence
NCSAL	Nearshore Coastal Dynamics on a Sea-breeze dominated microtidal beach
NLSW	Non-linear Shallow Water Equations
OBS	Optical Backscatter Sensor
PIV	Particle Image Velocimetry
PT	Pressure Transducer
SUV	Surface tracking and U & V velocity method
TKE	Turbulent Kinetic Energy
UDM	Ultrasonic Displacement Meters

ABSTRACT

The inner surf and swash zones are highly dynamic regions of the nearshore zone, characterized by unsteady, turbulent, sediment- and bubble-laden flows. Hydrodynamic and sediment transport processes occurring in these zones control sand exchange between the surf zone and foreshore, leading to foreshore morphological variation. Increased scientific interest and technological advances have contributed to the more recent advances in understanding of inner-surf and swash-zone processes. However, there is still the need of near-bed measurements of hydrodynamic and sediment transport to identify the role that small-scale inner-surf and swash-zone processes have on the beach during storm beach recovery (accretive conditions) and mesoscale meteorological phenomena (wind forcing mechanism). Therefore, two field-based studies were conducted to acquire detailed observations to address these needs. First, a field experiment was conducted on a steep sloping beach at South Bethany Beach, Delaware, USA in an attempt to quantify the foreshore morphological change during post-storm recovery. Near-bed, highly resolved hydrodynamic and sediment concentration measurements were collected at five cross-shore locations across the foreshore. Suspended sediment transport rates were estimated using instantaneous measurements of flow velocity and suspended sediment concentrations. A spatial and temporal variation of suspended sediment transport rates across the foreshore was identified. The larger transport events resulted from flow interactions that localized suspension and advection of sediment from the point of bore collapse and deposited landward (mostly by the cross-shore component). Net sediment transport and the associated foreshore morphological change were quantified via cross-shore suspended sediment transport rate gradients and an energetics-based suspended sediment transport model. Net suspended sediment transport rate gradient estimates exceeded by two orders of magnitude the

net transport quantified via bathymetric difference over each tidal cycle, highlighting the difficulty of predicting transport processes even under weak accretion conditions. This discrepancy implies that all potential mechanisms that enhance sediment transport (e.g. turbulence generated by swash bores, sediment advection) and complete measurements for the full flow duration and throughout the water column are needed to improve sediment transport rate estimates in the inner-surf and swash zone. However, these analyses served to relate the small-scale processes to large temporal and spatial scale accretive patterns.

A second field study was conducted on a microtidal, low wave energy, sea breeze dominated sandy beach in Sisal, Yucatán, Mexico to investigate the effects of local (land/sea breeze) and synoptic (Norte) scale meteorological events on inner-surf and swash-zone dynamics. Flow velocities and suspended sediment concentrations were measured concurrently at three cross-shore locations. The high-resolution data allowed the quantification of bed shear stress, turbulent dissipation rate and sediment transport rates. The change in wind speed and direction induced pronounced changes to the inner-surf and swash-zone dynamics. Field observations showed that strong inner-surf and swash-zone bed shear stresses, turbulence intensity and sediment suspension occur during sea breezes and Norte. Similarities between cross-shore and alongshore hydrodynamic parameters estimated during sea breezes and the Norte indicate that during sea breezes a significant amount of sediment can be mobilized inducing foreshore morphological changes similar to or greater than the effects generated by a short duration small storm. However, despite the milder energy conditions during land breezes, when these coincide with high tides, the estimated instantaneous hydrodynamic and sediment transport parameters often had similar orders of magnitude to sea breezes. These observations suggest that land breeze, under ideal conditions, can mobilize considerable amounts of sediment across the foreshore.

Chapter 1

INTRODUCTION

Puleo and Butt [2006] and Puleo and Torres-Freyermuth [2016] identified several key areas governed by inner-surf and swash-zone processes in need of better understanding. Several recommendations encouraged the work presented in this dissertation, including the need for near-bed measurements of hydrodynamics and sediment transport to understand the relation of small-scale inner-surf and swash-zone processes to post-storm beach recovery (accretive conditions) and mesoscale meteorological phenomena (wind forcing mechanism). This dissertation introduces field-based studies that acquired detailed observations to address these major key areas. Arrays of sensors were used to simultaneously measure fluid velocities and sediment concentrations at multiple cross-shore locations across the foreshore and estimate hydrodynamics and sediment transport parameters. Data obtained from these endeavors were used to better predict and understand sediment transport in these zones, through kinematic and statistical relationships.

The first portion of this dissertation (Chapter 2) provides a thorough background on the studies that have been undertaken in the swash zone in the last few decades. Extensive research efforts in the last decade have improved knowledge of swash-zone processes. This paper reviews and synthesizes from 2004 onward the research advances of small-scale hydrodynamics and sediment transport processes considering field, laboratory and numerical modeling efforts. Swash-zone hydrodynamics are examined by means of shoreline motions, fluid velocities, flow structure, bed shear stress, friction coefficients and turbulence. Subsequently, advances related to sediment transport mechanisms and morphological changes are described. Detailed descriptions of measuring techniques, novel findings, and the strengths and weaknesses of the different approaches are discussed. The review also acknowledges the major advances in the development of instrumentation to collect highly resolved flow and sediment concentration measurements in direct proximity of the bed. This work has since been published in Coastal Engineering (vol 115, 825. https://doi.org/10.1016/j.coastaleng.2015.10.008, 2015).

Following this review, two field-based studies are explored with the aim to better understand inner-surf and swash-zone dynamics under different forcing conditions. Chapter 3 uses field data from a steep sloping beach at South Bethany Beach, Delaware, USA, to try to better understand the hydrodynamic and morphodynamic processes controlling the accretional patterns of the foreshore. The measurements provided an opportunity to illustrate a number of inner-surf and swash-zone phenomena on a steep foreshore under accretive conditions. Suspended sediment transport rates were estimated using instantaneous measurements of flow velocity and suspended sediment concentrations. Net sediment transport and the associated foreshore morphological change were quantified via cross-shore suspended sediment transport rate gradients and an energetics-based suspended sediment transport model. The estimated parameters served to relate the small-scale processes to large temporal and spatial scale accretive patterns. This work is *in Review* in Continental Shelf Research.

Chapter 4 uses field data from a microtidal, low wave energy, sea-breeze dominated sandy beach at Sisal Beach, Sisal, Yucatán, México to investigate the effects of local (land/sea breeze) and synoptic scale metereological events on inner-surf and swash-zone dynamics. Studies focused on the understanding of inner-surf and swash-zone dynamics in such environments are scarce despite the important role of sea breezes on coastal dynamics. Prior studies have shown that surf zone wave energy intensifies during sea-breeze conditions [Sonu et al., 1973] and the impact on the coast can be similar to a small storm [Masselink, 1998]. However, to the author's knowledge, only one study has focused on swash-zone processes, although this zone is a natural defense for the backshore and dune from the full brunt of ocean waves. Therefore, this field study was aimed to obtain highly resolved near-bed hydrodynamic and sediment transport observations during different wind forcing conditions. The main emphasis was to provide estimations of small-scale inner-surf and swash-zone hydrodynamics and sediment transport processes on a sea-breeze dominated beach. This chapter will be submitted to Marine Geology. Finally, Chapter 5 provides a summary and conclusions.

Chapter 2

ADVANCES IN SWASH-ZONE RESEARCH: SMALL-SCALE HYDRODYNAMIC AND SEDIMENT TRANSPORT PROCESSES

2.1 Introduction

The active swash zone (Figure 2.1) is a dynamic region separating land from inner surf zone coastal processes. There are many reasons why the swash zone is important: it is a primary area for beach recreation, it is a region of active beach accretion and erosion, beach nourishment activities often extend into the swash zone, nutrient/chemical species cycling between groundwater/oceanic flows occurs across the foreshore, and certain types of fauna are prevalent in or use the swash zone (e.g. birds, horseshoe and sand crabs). The swash zone is an integral part of the nearshore and represents a landward boundary condition for large-scale numerical models. Hence, there is a general scientific interest in the physical processes taking place within this region. Swash-zone processes occur across the foreshore with the cross-shore extent modulated by individual waves, infragravity energy and tidal fluctuations. This region is where wave energy is finally dissipated or reflected implying that the swash zone serves in a buffer capacity for hydrodynamic forcing.

The swash zone on most beaches is readily accessible, but this accessibility does not translate into a wide knowledge of the underlying physical processes. This zone exhibits some of the most challenging attributes in the coastal ocean with regard to measurement and modeling campaigns. Flows in the swash zone reverse direction with the reversal timing varying across the foreshore extent. Flows are rapid and contain large sediment loads and void fraction. Turbulence is acknowledged as important for energy considerations and sediment mobility but quantification is hampered through non-stationarity and signal discontinuity (for instance due to intermittent submergence of instrumentation and/or to flows laden with bubbles and sediment). Fluid/sediment processes are further complicated by a highly variable sea bed with elevation variability occurring across a wide range of frequencies.

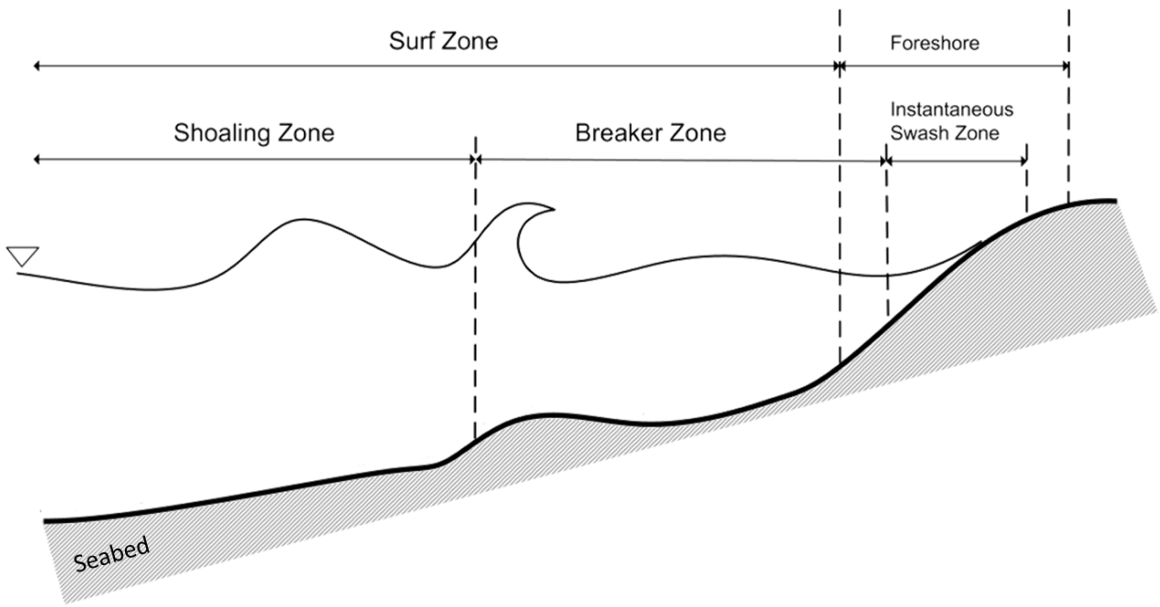

Figure 2.1. Schematic of the cross-shore beach profile showing surf and swash zones.

Increased societal/scientific interest and technological advances have contributed to the more recent advances in understanding of swash-zone processes. The increased interest in swash-zone research resulted in the publication of several review papers [Bakhtyar et al., 2009; Brocchini and Baldock, 2008; Butt and Russell, 2000; Elfrink and Baldock, 2002; Longo et al., 2002; Masselink and Puleo, 2006; Puleo and Torres-Freyermuth, 2016; Chardón-Maldonado et al., 2016; Briganti et al., 2016] related to hydrodynamics, sediment transport and morphodynamics, through laboratory, field and numerical efforts. The present work provides an overview of the most recent advances related to swash-zone research. This review paper addresses short time-scale hydrodynamics, and small-scale sediment transport and morphology.

2.1.1 Hydrodynamics

Natural beaches are dynamic and complex with high temporal and spatial variability, leading to difficulties in quantifying swash-zone hydrodynamic processes. Numerous research efforts have reduced their temporal scope of interest to focus on processes occurring on a wave-by-wave time scale. In laboratory studies, the isolation of such processes occurs for a single swash event via solitary wave [e.g., Alsina et al., 2009; Barnes et al., 2009; Barnes and Baldock, 2007; Sumer et al., 2011], dam break forcing [Kikkert et al., 2013, 2012; O'Donoghue et al., 2010; Othman et al., 2014; Steenhauer et al., 2011; Yeh and Ghazali, 1988], or ensemble averaging of swash events under regular or irregular wave forcing [Cowen et al., 2003; Mihoubi et al., 2012; Pedrozo-Acuna et al., 2011; Sou and Yeh, 2011]. In field studies, the analysis may be simplified by using only a single swash event or a typical swash event through ensemble averaging. A single event in the field is identified by periods of zero water depth, zero up crossings in a velocity time series, or the time between submergence and emergence of an elevated current meter [e.g., Austin et al., 2011; Baldock and Hughes, 2006; Butt et al., 2004; Hughes and Baldock, 2004; Lanckriet et al., 2014; Masselink et al., 2009; Masselink and Russell, 2006; Raubenheimer et al., 2004]. Individual swash events have received attention in part due to repeatability in laboratory studies. Repeatability 1) allows for spatial coverage of the cross-shore swash extent by laterally and/or vertically shifting measurement instrumentation, 2) increases confidence of measurements and 3) enables quantification of the turbulence field via ensemble-averaging techniques.

The evolution of hydrodynamic properties (i.e., water depths, velocities, bed shear stresses, turbulence) in the swash zone varies throughout the swash event. The different flow conditions are sometimes categorized using the Froude number ($Fr = u/\sqrt{gh}$) in terms of the cross-shore flow velocity (u), a length scale given by the water depth (h), and the gravitational acceleration (g). The different phases of the swash motion are: (i) bore arrival at the seaward boundary where the velocity is onshore-directed with $Fr > 1$; (ii) an uprush phase where the flow decelerates with $Fr < 1$;

(iii) a flow reversal phase where the velocity reduces until it eventually reverses direction (Fr $<$ 1); and (iv) a backwash phase where the velocity is offshore-directed and accelerating, evolving from $Fr < 1$ to $Fr > 1$ late in the backwash phase [Baldock and Hughes, 2006; Brocchini and Baldock, 2008; Butt et al., 2004; Guard and Baldock, 2006; Masselink and Russell, 2005; Mory et al., 2011], until the flow decelerates during the last portion of the event.

In the following subsections, the main hydrodynamic properties are described during the different flow phases, together with descriptions of new measuring techniques and numerical model findings. Quantitative results are provided where possible. However, it is acknowledged that the reported values may be applicable only to a specific study. No mathematical descriptions of the numerical schemes are given. Instead, the reader is referred to Briganti et al. [2016] for in-depth description regarding numerical formulations.

2.1.1.1 Water level and shoreline motions

Figure 2.2 depicts a typical free swash event including water depth, cross-shore velocity, and sediment transport. The term free is used here to describe a swash event with little interaction between the backwash and ensuing uprush (i.e., dam break scenario). Water depth for a swash event (Figure 2.2) is asymmetric, rising rapidly upon initial inundation and reaching a maximum shortly before flow reversal [Barnes et al., 2009; Hughes and Baldock, 2004; Kikkert et al., 2012; O'Donoghue et al., 2010]. The maximum water depth is related to variations in momentum of the different parcels of fluid. The inflow of additional momentum is important as it shifts the location of the maximum water depth experienced at a given location to later instants after bore arrival [Baldock et al., 2005]. Fluid parcels at the bore front experience larger friction and converge at the bed while the parcels behind the bore front with higher momentum are continuously injected into the front [Baldock et al., 2014; Barnes and Baldock, 2010]. Water depth decreases during backwash at a slower rate relative to the increase during uprush and ultimately pinches to zero at the end of the backwash if the free swash event is unencumbered by a subsequent uprush. Water depth time series are more symmetric in the landward direction as the bore head and overall momentum of the uprush are progressively reduced.

Water depth can be quantified using *in situ* or non-intrusive approaches. *In situ* pressure transducers measure water depth based on the assumption of hydrostatic pressure distribution. These transducers are commonly positioned just below or in direct vicinity of the bed. Capacitance and resistance gauges measure water depth, but are commonly restricted to laboratory settings. *In situ* resistance runup wires are used to measure the runup excursion across the foreshore. Non-intrusive techniques used to measure free surface elevations consist of ultrasonic displacement meters (UDM), laser-induced fluorescence (LIF), light detection and ranging (LIDAR), laser Doppler anemometry (LDA or LDV), and video imagery for shoreline position. UDMs measure free surface or bed level when the water either covers or uncovers a particular cross-shore location. Therefore, they are often deployed in cross-shore arrays. LIF techniques are used in laboratory studies because the water must be dyed and illuminated to enhance water reflection. LIDAR is a continuously scanning laser beam that detects swash-zone water surface and exposed bed when the incident angle of the beam is approximately perpendicular to the surface [Blenkinsopp et al., 2010a; Vousdoukas, 2014]. Video imagery through the side wall of a laboratory flume can be used to determine water levels [Erikson et al., 2005; Sou et al., 2010; Sou and Yeh, 2011].

Water depth measurements over time and space allow the estimation of hydrodynamic parameters such as bore front velocity and cross-shore pressure gradients. The relative position of the instrumentation within the swash zone can be estimated in terms of the percentage of time the bed is inundated in the measured signal over a given period (e.g., tide) or by considering the mean water level [Aagaard et al., 2006;

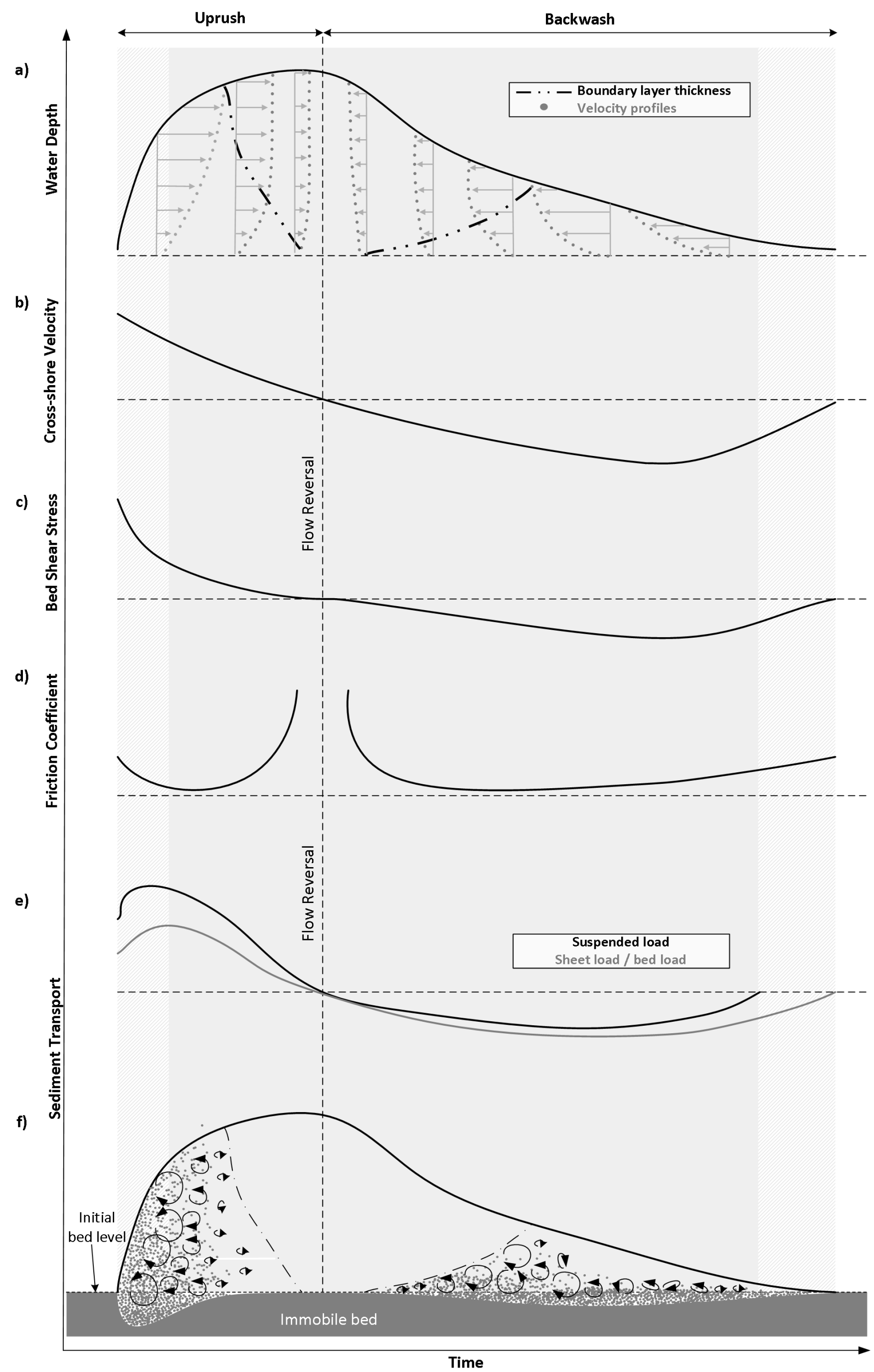

Figure 2.2. Schematic of hydrodynamic and sediment transport processes occurring within a single free swash event. The gray area depicts the duration of *in situ* measurements generally acquired in field and laboratory studies. The line pattern area depicts the duration of measurements acquired with numerical approaches or a few other techniques (*in situ* or remote) that can sample the entire swash duration.

Hughes and Moseley, 2007; Masselink and Russell, 2005, 2006]. Hence, estimates of shoreline minima and maxima [e.g., the 2.5 and 97.5 percentiles of inundation time; Hughes and Moseley, 2007] can be used to delimit the swash zone extent over time. Additionally, free surface elevation and shoreline motion time series enable the identification of swash-swash interactions [Alsina and Caceres, 2011; Brocchini and Baldock, 2008; Jackson et al., 2004].

Shoreline motions are driven by incident and infragravity waves. Incident-band related motions result from wind waves and swell (roughly $f > 0.05$ Hz; where f is frequency). Water depth and shoreline motions in the incident band are largely related to foreshore slope where the energy in the surf zone is typically saturated [Guza and Thornton, 1982; Hughes et al., 2014; Ruessink et al., 1998; Senechal et al., 2011]. Infragravity related motions correspond to long-waves (roughly $f < 0.05$ Hz) often associated with edge waves [Holman and Sallenger, 1985; Hughes et al., 2014; Ruggiero et al., 2004]. Water depth and shoreline motions in the infragravity band increase with increasing offshore energy [Guza and Feddersen, 2012; Holland et al., 1995; Hughes et al., 2014; Ruggiero et al., 2004].

Shoreline motions, composed of wave setup and swash, are influenced by offshore wave characteristics, foreshore slope and morphology. The maximum elevation is reached during storm events influenced by storm surge and infragravity components within the surf zone. Prediction of runup height (including both wave setup and swash) is of particular interest in engineering applications (i.e., improve coastal morphology response and flooding hazard models and design of coastal structures). Although the aim of this review paper is to focus on small-scale swash-zone processes, a brief overview of statistical and spectral analysis of runup is given. Readers are directed to the cited papers for in-depth description.

Runup on dissipative beaches is linearly proportional to the offshore significant wave height with variability in the empirical coefficients [Guza and Feddersen, 2012; Ruggiero et al., 2004; Ruessink et al., 1998; Ruju et al., 2014]. Statistical approaches identified a dependence of the 2% runup exceedence ($R_{2\%}$) [Stockdon et al., 2006] to dimensional forms of the Iribarren number [ξ; Iribarren and Nogales, 1949] relating the foreshore slope to offshore wave steepness. The ($R_{2\%}$) provides a quantitative method to predict flooding hazards and morphodynamic changes [Stockdon et al., 2007]. Stockdon et al. [2006] evaluated a wide range of beach types and non-storm conditions to develop an empirical formulation for $R_{2\%}$. $R_{2\%}$ correlates well with Iribarren number on reflective/intermediate beaches but only with offshore significant wave height and wavelength on dissipative beaches. Stockdon et al. [2007] used numerical modelling to extend the applicability of the Stockdon et al. [2006] empirical model to storm conditions. Runup heights can also be affected by offshore frequency and directional spread of incoming waves [Guza and Feddersen, 2012]. Hughes et al. [2014] performed spectral analyses on numerous time series from a variety of beaches with foreshore slopes ranging from 1:6 to 1:60 and offshore wave heights of 0.5 to 3.0 m. They found that swash energy in the incident band is dominant on steep and intermediate foreshores whereas that in the infragravity band is dominant on shallow sloping foreshores. The results are cast into a morphodynamic beach state model [Wright and Short, 1984] such that there is a shift in the spectral signatures under increasing or decreasing wave energy as: 1) the incident band spectrum is fairly constant for all beach states with an f^{-4} roll off and controlled by the foreshore slope, 2) the width of the energy roll off varies with offshore energy and inversely with foreshore slope, and 3) the infragravity portion of the spectrum varies for all beach states and is related to offshore energy and beach morphology.

2.1.1.2 Cross-shore and alongshore swash-zone velocities

Swash-zone flows are shallow, short-lived and regularly laden with bubbles and sediment. Cross-shore swash-zone flow (Figure 2.2) is typically initiated by a collapsing bore that moves a pulse of turbulent water up the foreshore inducing a sudden increase in velocity. During the majority of the uprush the flow decelerates due to bottom friction, gravitational acceleration and the pressure gradient force acting in tandem [Baldock and Hughes, 2006]. Backwash flow accelerates under favorable gravity and pressure gradient force with bottom friction acting in opposition. These forces acting in the same direction (uprush) or in opposition (backwash) cause asymmetry in the swash-zone velocity time series. The asymmetry is particularly evident in the latter stages of backwash where the bottom friction begins to dominate the flow causing the velocity to decrease [Barnes and Baldock, 2007; O'Donoghue et al., 2010].

Many efforts have focused on measuring swash-zone velocities to quantify flow structure over the foreshore enabling the estimation of hydrodynamic parameters such as bed shear stress [Aagaard et al., 2006; Inch et al., 2015; Kikkert et al., 2012, 2013; Masselink and Russell, 2005; O'Donoghue et al., 2010; Puleo et al., 2012], friction coefficients [Barnes et al., 2009; Inch et al., 2015; Puleo et al., 2014a; Raubenheimer et al., 2004] and turbulence [Kikkert et al., 2012, 2013; Lanckriet and Puleo, 2013; O'Donoghue et al., 2010; Raubenheimer et al., 2004; Sou et al., 2010]. Velocities are obtained using *in situ* sensors and non-intrusive techniques. *In situ* sensors consist of impeller current meters, electromagnetic current meters (EMCM), acoustic Doppler velocimeters (ADV), and acoustic Doppler profiling velocimeters (ADPV). Impeller current meters measure the signed velocity magnitude; usually cross-shore but alongshore motions cannot be separated due to the mechanics of the sensor. The sensor diameter ($\sim$0.04 m) does not allow deployment in close proximity to the bed [Puleo et al., 2000]. EMCMs provide two-dimensional velocity measurements (usually u, v corresponding to the cross-shore, x, and alongshore, y, directions, respectively) at a fixed elevation with low-sampling rate ($\leq$ 8 Hz). EMCMs have a small measuring volume in the vertical direction enabling sensor deployment within a few centimeters of the bed. ADVs and ADPVs utilize the Doppler shift of acoustic returns and are capable of sampling at high frequency (100 Hz or more). Side-looking ADVs can be deployed just above the bed. Other ADVs are deployed in the downward-looking direction providing all three velocity components (including w in the vertical, z, direction). ADPVs [e.g. Vectrino II by Nortek; Craig et al., 2011] deployed downward-looking can profile all the three velocity components over a range of 0.03 m at 0.001 m bin spacing. The minimum elevation for downward-looking acoustic sensors is about 0.05 m. One difficulty with acoustic sensors is the inability to return robust velocities when the sensor is initially inundated by bubbly flow. EMCMs and impellers have fewer difficulties under intermittent submersion conditions but impellers may be slowed under sediment-laden flow. All *in situ* current meters require elevation adjustment under conditions with active morphological change if the distance relative to the bed is meant to be similar throughout a particular study. In addition, data are only obtained when the water depth reaches or exceeds the sensor elevation. Thus, elevated (relative to the bed) sensors cause artificial truncation of swash event duration (see the line pattern areas in Figure 2.2 for example).

There are a variety of non-intrusive sensing techniques that can be used to measure or infer swash velocities. Particle image velocimetry (PIV) is a non-intrusive flow measurement technique that relies on optical sensors to capture variations in image texture usually provided by seeded particle patterns [Adrian, 1991; Stevens and Coates, 1994]. PIV uses statistical techniques to quantify the shift of pixel intensity patterns captured in sequential frames of video imagery. The inferred velocity varies depending on the camera position, whether pointed through a glass flume wall or bed or from above imaging the water surface. In laboratory experiments, the camera is typically located outside the wave tank and captures successive images of sediment particles, fluorescent particles or silver-coated hollow glass spheres. The water is illuminated by a laser system that delivers a light sheet [Kikkert et al., 2012, 2013; O'Donoghue et al., 2010] along a particular plane, generally x, z. Kikkert et al. [2012, 2013]; O'Donoghue et al. [2010] reported that velocities cannot be measured near bore arrival due to the high percentage of entrained air. Cowen et al. [2003] used fluorescent particles and optical filters such that only the particles were imaged overcoming the difficulty with bubbles. Puleo et al. [2003a] imaged the swash-zone free surface in the field using cameras deployed on a building roof top. Uprush velocities were quantified via PIV using natural aeration and bubbles as tracers, but backwash velocities were difficult to quantify due to insufficient surface texture. Other non-intrusive techniques use laser Doppler anemometry or velocimetry (LDA or LDV) that measures fluid velocities by detecting the frequency shift of laser light scattered by particles suspended in the translucent and non-aerated fluid [Shin and Cox, 2006]. These sensors are positioned outside the wave tank and emit the laser pulse through the glass side wall. The authors are unaware of LDA or LDV techniques being used in swash-zone field studies.

Swash-zone velocity measurements can be collected across the foreshore but are often divided into regions for simplicity. The outer swash zone is the region with wave-swash interactions, while the inner swash zone consists of solely swash motion [Hughes and Moseley, 2007] . These regions are relative cross-shore locations on the foreshore and vary with tidal modulations. Sensor elevation may also dictate whether or not the potential for wave-swash interaction is captured. For example, velocities may be recorded for a large portion of the swash event duration if deployed close to the bed, but only a short portion of the swash event duration if farther away (note that the difference between close to the bed and farther away may only be 0.1 m; for example). The relative cross-shore position and elevation vary from study to study. The reader is cautioned that the following comparisons from multiple studies do not account explicitly for the potential spatial differences in sensor deployment. Rather, maximum observed values are given where appropriate.

Maximum uprush velocities measured on moderate to gently sloping natural sandy foreshores varied from 1.0 m s^{-1} to more than 2.0 m s^{-1}, while backwash velocities varied from 0.5 to 2.0 m $^{-1}$ [e.g., Aagaard et al., 2006; Butt et al., 2009; Masselink et al., 2009; Masselink and Russell, 2006; Puleo et al., 2014a; Tinker et al., 2009]. Meanwhile, on steep sandy foreshores maximum uprush velocities of 1.5 to 3.0 m s^{-1} and 1.0 to 2.2 m s^{-1} for backwash velocities were measured [Conley and Griffin, 2004; Houser and Barrett, 2010; Shanehsazzadeh and Holmes, 2007]. Maximum uprush velocities of 1.5 m s^{-1} to 2.0 m s^{-1} and backwash velocities exceeding 2.0 m s^{-1} have been reported on steep foreshores composed of fine gravel [Austin et al., 2011; Masselink et al., 2010]. It is generally found that maximum uprush velocities are either similar to or slightly larger than the maximum backwash velocities. Swash-zone uprush and backwash velocities recorded in laboratory dam break experiments vary from 1.5 to 2.0 m s^{-1} and 1.0 to 1.5 m s^{-1} respectively on immobile rough beds under the same forcing conditions [Barnes et al., 2009; Kikkert et al., 2012; O'Donoghue et al., 2010]. Maximum velocity magnitudes exceeding 1.5 m s^{-1} were recorded in laboratory experiments with swash motion forced by irregular waves [e.g., Alsina et al., 2012; Briganti et al., 2011].

Alongshore flows are mostly unidirectional and have received less attention compared to cross-shore flows [Austin et al., 2011]. Alongshore flows on gentle and steep foreshores can reach maximum velocities of 1.5 m s^{-1}, often exceeding cross-shore velocities [Austin et al., 2011; Puleo et al., 2014a]. Therefore, it may be critical to incorporate alongshore velocities into calculations of the bed shear stress and predictions of swash-zone sediment transport.

2.1.1.3 Depth-averaged cross-shore velocity

The previous section highlighted the difficulty in obtaining swash-zone velocity time series for the full duration of a swash event. The volume continuity method using spatial and temporal measurements of water depth can partially overcome this difficulty. The method enables estimation of the depth-averaged cross-shore velocity by dividing cross-shore volume flux by local water depth (for example using UDM or LIDAR). The volume continuity method has been used in numerical models [e.g., Hughes and Baldock, 2004; Turner and Masselink, 1998], laboratory studies [Baldock and Holmes, 1997], and field studies [e.g., Baldock et al., 2004; Blenkinsopp et al., 2010a,b; Houser and Barrett, 2009a, 2010]. Cross-shore velocities estimated in this manner compare well with *in situ* measurements in terms of velocity magnitude (root-mean square velocity differences of 0.2 m s^{-1}) and the timing of flow reversal [Blenkinsopp et al., 2010b; Hughes and Baldock, 2004]. The estimated velocity may be larger at the initiation of uprush and end of backwash relative to *in situ* velocity measurements due to the spacing of the *in situ* or non-intrusive sensors (EMCM or UDM). Differences in the sampling rates between sensors may also cause phase inconsistencies in the signals. The advantage of the volume continuity technique is the ability to provide cross-shore velocity time series for an entire swash event and at multiple locations across the foreshore. However, 1) no information about the vertical velocity structure is obtained, 2) a fixed bed level must be assumed, and 3) uncertainties from LIDAR during the extremely shallow backwash flows may yield exaggerated velocity asymmetry. Additionally, this method does not account for fluid infiltration/exfiltration and alongshore flows.

2.1.1.4 Bed shear stress and friction coefficients

Bed shear stress and friction coefficients are important hydrodynamic parameters associated with sediment transport processes. Different methods have been proposed to estimate these parameters in the swash zone, such as the quadratic drag law [Barnes et al., 2009; Masselink et al., 2009; Masselink and Russell, 2005; Puleo et al., 2012; Raubenheimer et al., 2004] the von Karman-Prandtl relationship using near bed velocity profiles [e.g., Austin et al., 2011; Inch et al., 2015; Miles et al., 2006; Puleo et al., 2014a, 2012], and direct measurements using a shear plate or thermal techniques [Barnes et al., 2009; Conley and Griffin, 2004]. The shear plate approach relates bed shear stress from a linear relationship to plate displacement. Hot film anemometry quantifies the shear stress based on temperature changes within the sensor.

The quadratic drag law is given as

$$\tau_i = 0.5\rho c_f u_i |u_i|, \tag{2.1}$$

where $u_i (= u; v)$ velocity component, $i = x; y$ component τ_i is the shear stress, c_f is the friction coefficient, and || indicate absolute value. Equation (2.1) is widely applied in studies where the velocity was collected at a single elevation above the bed. The embedded friction coefficient should mostly depend on grain size and flow conditions [Swart et al., 1974] but frictional resistance may also depend on the sediment transport regime [Wilson, 1987]. Using equation 2.1 in the swash zone often relies on a constant friction coefficient [Barnes et al., 2009; Barnes and Baldock, 2007; Conley and Griffin, 2004; O'Donoghue et al., 2010; Puleo et al., 2014a; Puleo and Holland, 2001]. But, c_f may change with time and space [Barnes et al., 2009; Inch et al., 2015; Puleo et al., 2014a, 2012; Raubenheimer et al., 2004]. When velocity profile data exist, c_f is estimated by

$$c_f = (2u_* |u_*|)/(u_i |u_i|), \tag{2.2}$$

where u_* is the friction velocity that can be determined by calculating the slope (m) of the least squares regression between the velocity profiles and $ln(z)$ as

$$u_* = m\kappa, \tag{2.3}$$

Alternatively, if only two velocity time series from different elevations are collected, u_* can be calculated as,

$$u_* = \kappa \frac{u_i}{(ln(z_u/z_l))}, \tag{2.4}$$

where $\triangle u$ is the velocity difference between the upper and lower sensor, located at z_u and z_l, respectively [Austin et al., 2011]. If only one velocity time series from a single elevation is collected, u_* may be calculated by fitting a logarithmic model and assuming a value for the bed roughness z_0 (= 0.004 m) [Raubenheimer et al., 2004].

$$u_* = \frac{\kappa u_i}{(ln(z_s/z_0))}, \tag{2.5}$$

where z_s is the height above the bed with $z_s = 0$ at the instantaneous bed level. The fundamental definition of u_* is

$$u_* = \sqrt{\tau_i/\rho} \tag{2.6}$$

Hence, the bed shear stress is obtained by algebraic rearrangement of equation (2.6).

Furthermore, when bed shear stress (i.e., hot film and shear plate) and velocity profile data are known, c_f can be estimated using equation (2.1) as [Conley and Griffin, 2004]

$$c_f = \tau_i \frac{2}{\rho u_x^2} \tag{2.7}$$

The friction coefficient has a local minimum after uprush initiation and at mid stages of backwash (Figure 2.2d), while, a local maximum c_f occurs near flow reversal. Friction coefficient estimates determined from equation (2.2) range from 0.003 to 0.06 for flows on natural beaches [e.g. Puleo et al., 2014a; Raubenheimer et al., 2004]. On rough, impermeable beds, c_f ranges from 0.01 to 0.1 [Kikkert et al., 2012; O'Donoghue et al., 2010] and from roughly 0.002 to 1.0 on smooth beds [Cowen et al., 2003; O'Donoghue et al., 2010]. Over rough, permeable beds, c_f ranges from 0.009 to 0.5 [Kikkert et al., 2013]. Friction coefficients estimated from equation (2.7) under field conditions range from 0.002 to 0.004 [Conley and Griffin, 2004], 5 to 10 times smaller than estimates obtained from equation (2.2). Meanwhile, c_f estimates using equation (2.7) vary from 0.003 to 0.04 on smooth, impermeable beds to 0.002 to 0.06 on rough, impermeable beds [Barnes et al., 2009]. The large range of c_f can be attributed to differences in cross-shore measurement location, instrumentation, bottom type and the elevation above the bed from which the velocity was collected. For example, errors in the assumed elevation of a velocity measurement can lead to errors in c_f by 40 % [Raubenheimer et al., 2004]. This error, consequently, has a direct effect on the bed shear stress estimated by equation 2.1 [Puleo et al., 2014a].

Studies have shown the same general evolution of the bed shear stress within an individual swash event regardless of the method used (Figure 2.2c). Bed shear stress is maximum at uprush initiation and decreases to zero through flow reversal [Barnes and Baldock, 2007]. Bed shear stress peaks again near the mid- to late-backwash [Austin et al., 2011; Inch et al., 2015; Masselink and Russell, 2005; Puleo et al., 2012] and then decreases to zero at the end of the backwash [Barnes et al., 2009; Barnes and Baldock, 2007; Conley and Griffin, 2004].

Maximum bed shear stress estimates using the von Karman-Prandtl approach vary from 4 to 50 N m^{-2} on dissipative beaches [Austin et al., 2011; Inch et al., 2015; Masselink and Russell, 2005; Puleo et al., 2014a]. On moderate sloping foreshores, bed shear stress can reach 150 N m^{-2} [Miles et al., 2006]. Weaker forcing conditions (smaller swash-zone velocities) are, not surprisingly, associated with smaller bed shear stresses. Under low wave-energy conditions, Conley and Griffin [2004] using hot film anemometry, estimate a maximum bed shear stress of 3.2 N m^{-2} and 1.2 N m^{-2} during the uprush and backwash, respectively. Uprush bed shear stress exceeds backwash bed shear stress in most cases [Austin et al., 2011; Barnes et al., 2009; Barnes and Baldock, 2007; Butt et al., 2005; Conley and Griffin, 2004; Miles et al., 2006; Puleo et al., 2014a]. An exception was in the Puleo et al. [2012] study, but the acoustic sensor was often unable to obtain velocities or allow for bed shear stress estimation for much of the short uprush duration due to aeration. Thus, larger bed shear stresses expected in the uprush were not measured. Maximum bed shear stresses over rough, impermeable beds can reach $O(10^2)$ N m^{-2} [Barnes et al., 2009; Kikkert et al., 2012; O'Donoghue et al., 2010], while the bed shear stress is $O(10)$ N m^{-2} over smooth beds [Barnes et al., 2009;

O'Donoghue et al., 2010]. Maximum bed shear stresses over permeable beds [Kikkert et al., 2013] were similar to those reported by Kikkert et al. [2012] over impermeable beds. The aforementioned field and laboratory studies have focused on estimating bed shear stress variability from cross-shore velocities. However, bed shear stress on sandy beaches estimated using alongshore velocities can have similar magnitudes (12 to 15 N m^{-2}) to those estimated from cross-shore velocities only [Austin et al., 2011; Puleo et al., 2014a].

2.1.1.5 Turbulence structure

Turbulence in the swash zone arises from plunging breakers and wave-driven bores collapsing/arriving at the shoreline (externally advected, referred to as bore-related), and due to the bottom presence (locally generated, referred to as bed-related) [Aagaard et al., 2006; Cowen et al., 2003; Longo et al., 2002; Petti et al., 2001; Puleo et al., 2000; Sou et al., 2010; Zhang and Liu, 2008]. The bed-related source of turbulence is present during uprush and backwash. The bore-related turbulence exists during the uprush phase of the flow only. Turbulence characterization in the swash zone is related to turbulent kinetic energy TKE or the turbulent dissipation rate per unit mass (ε).

Turbulent kinetic energy

The separation of velocity fluctuations from the mean flow in the swash zone is difficult [Petti and Longo, 2001] and standard approaches used in the surf zone are challenging to apply in the swash zone owing to flow discontinuities and accelerations [Longo et al., 2002]. Turbulence generation due to vortex shedding around sensors can also lead to difficulty when estimating TKE. One approach used to investigate TKE is via spectral analysis of the velocity components, where the macro (at similar wave frequencies) and micro (shorter frequencies) vortices are related to the energy transfer and energy dissipation, respectively [Petti and Longo, 2001]. Butt et al. [2004] estimated TKE using ADV time series collected near the surf-swash zone transition to minimize discontinuities in the time series. The maximum TKE was related to the interaction between a receding backwash and incident bore with TKE values on the order of $O(10^{-1})$ m^2 s^{-2}. The contribution of each component of the velocity to the total velocity variance accounted for 65 %, 28 % and 7 %, corresponding to the cross-shore, u, alongshore, v, and vertical, w, velocity components respectively, suggesting that the use of u and v may suffice for TKE estimates. The cutoff frequency separating turbulence motions may affect the estimated TKE levels. For instance the TKE increased by 37 % using a 0.5 Hz cut off, or decreased by 23 % using a 2 Hz cut off.

Aagaard et al. [2006] assumed that TKE scales with the vertical velocity variance [TKE $\propto w' \mid w' \mid \propto w \mid w \mid$; Svendsen, 1987] as obtained from ADV measurements at three locations across the foreshore. The reported values were mostly negative with values in the range -0.35 m^2 s^{-2} $< w \mid w \mid <$ 0.05 m^2 s^{-2} suggesting the formation and down bursting of coherent structures at the bore front and strong shear in the water column near the swash-swash interaction region (i.e., hydraulic jumps). Aagaard et al. [2006] also concatenated swash events, essentially removing portions of the time series when the sensor was exposed, before performing spectral analysis. An $f^{-5/3}$ roll off was found in the inertial subrange (0.1 Hz $\leq f \leq$ 2.0 Hz) with turbulence accounting for up to 95 % of the vertical velocity fluctuations. The existence of a characteristic $f^{-5/3}$ roll off in the inertial subrange indicates that the turbulence is concentrated in this frequency range, accounting for 74 % to 95 % of the total w variance.

Another approach to estimate TKE is through phase or ensemble averaging [Longo et al., 2002] of swash events with a high degree of similarity. This approach is most easily applied for laboratory studies under controlled forcing (dam break, regular or solitary waves) and fixed impermeable bed [Cowen et al., 2003; Kikkert et al., 2012; O'Donoghue et al., 2010; Sou and Yeh, 2011] or fixed permeable slopes [Kikkert et al., 2013]. Velocity fluctuations used in the TKE estimate are obtained as the deviations from the ensemble average. In particular, O'Donoghue et al. [2010] report increases in TKE on the order of $O(10^1)$ m^2 s^{-2} due to increases in roughness for dam break-driven swash events over smooth and rough beds. Moreover, Kikkert et al. [2013] document diminished turbulence levels (TKE and turbulent shear) due to infiltration that depends on grain size.

Findings from laboratory and field efforts indicate TKE during uprush is bore-related [Aagaard et al., 2006; Butt et al., 2004; Butt and Russell, 1999; Jackson et al., 2004; Kikkert et al., 2013, 2012; Masselink and Russell, 2005; O'Donoghue et al., 2010; Petti et al., 2001; Puleo et al., 2000] with magnitudes ranging from 0.02 to 0.4 m^2 s^{-2}. Consequently, the production of TKE appears to result from shear forces inside the flow during bore collapse [Sou et al., 2010] and the main TKE mechanism during uprush is production [Zhang and Liu, 2008] and sinking of TKE into the bed [Kikkert et al., 2013; Pintado-Patiño et al., 2015]. Most of the TKE content during uprush is dissipated by the time of flow reversal, decaying homogeneously [Kikkert et al., 2013, 2012; O'Donoghue et al., 2010] and similar to grid turbulence [Cowen et al., 2003; Sou et al., 2010]. Backwash begins from rest with minimal initial TKE content. TKE is continuously generated at the bed [Cowen et al., 2003; Sou et al., 2010; O'Donoghue et al., 2010; Desombre et al., 2013] until the end of the backwash. The formation of a backwash bore [Zhang and Liu, 2008] and hydraulic jumps due to swash-swash interactions [Aagaard et al., 2006; Butt and Russell, 2005] contribute as additional sources of TKE that can be advected back into the swash zone and/or exported to the surf zone [Butt et al., 2004; Petti et al., 2001]. The infiltration and exfiltration of water at the sediment water interface may also increase TKE on a permeable bed [Kikkert et al., 2013; Pintado-Patiño et al., 2015]. It is anticipated that enhanced understanding of swash-zone TKE will come from more elaborate laboratory studies focusing on swash-swash interactions.

Turbulence dissipation

Turbulence dissipation is quantified to estimate the rate at which TKE is converted to smaller scales and ultimately thermal energy. Different methods (direct and indirect) exist to calculate ε using field and laboratory measurements. An example of the direct method is based on PIV-generated data from repeatable swash events in the laboratory [Sou et al., 2010]. The turbulent dissipation rate is quantified from

$$\begin{aligned} \varepsilon \;=\; \nu \Bigg[& 4\left\langle\left(\frac{\partial u'}{\partial x}\right)^2\right\rangle + 4\left\langle\left(\frac{\partial w'}{\partial z}\right)^2\right\rangle + 3\left\langle\left(\frac{\partial u'}{\partial z}\right)^2\right\rangle + 3\left\langle\left(\frac{\partial w'}{\partial x}\right)^2\right\rangle \\ & +6\left\langle\left(\frac{\partial u'}{\partial z}\frac{\partial w'}{\partial x}\right)\right\rangle + 4\left\langle\left(\frac{\partial u'}{\partial x}\frac{\partial w'}{\partial z}\right)\right\rangle\Bigg] \end{aligned} \tag{2.8}$$

where ν is the kinematic viscosity, $'$ denotes the velocity turbulent component, and $\langle\ \rangle$ denotes phase averaging. The time evolution of ε exhibits a decay rate in the form of a power law with an exponent of 2.3 during the majority of the swash event and consistent with expectations for grid turbulence [Sou et al., 2010]. Dissipation rate magnitudes of $O(10^{-2})$ m^2 s^{-3} were observed for plunging waves (H$_o$ = 0.246 m ; ξ = 0.56) on a 1:20 slope.

Indirect methods employ the Kolmogorov hypothesis and rely on the frequency spectrum [Aagaard et al., 2006; Raubenheimer et al., 2004], wavenumber spectrum [Cowen et al., 2003], or the structure function [Lanckriet and Puleo, 2013]. The frequency spectrum requires a special treatment of the spectral domain due to the non-periodicity of the swash signal and related noise [Sou et al., 2010]. Raubenheimer et al. [2004] pre-set to null values the velocity measurements during times of sensor exposure. This procedure served to eliminate the spectral contribution of the exposure times when performing spectral calculations. Swash-zone velocity spectra showed an $f^{-5/3}$ roll off in the inertial sub range denoting the dissipation of energy. The analysis resulted in turbulence dissipation rates of $O(10^{-2})$ m^2 s^{-3} and $O(10^{-1})$ m^2 s^{-3} for the inner surf zone and swash zone respectively.

Lanckriet and Puleo [2013] and Brinkkemper et al. [2015] estimated ε using the structure function [Pope, 2000; Wiles et al., 2006] applied to swash-zone ADPV data. The structure function relies on vertical profiles of w', where the vertical component is typically used due to a lower noise floor. The second-order longitudinal structure function (D) is defined as

$$D(z,r,t) = \langle \{w'(z+r,t) - w'(z,t)\} \rangle = C\varepsilon(z,t)^{\frac{2}{3}} r^{\frac{2}{3}}, \tag{2.9}$$

where r is the separation distance between velocity bins in the profile, C=2.0 is an empirical constant, and $\langle\ \rangle$ denotes time averaging. Curve fitting and algebraic rearrangement of equation 2.9 provides the dissipation rate. Lanckriet and Puleo [2013]; Brinkkemper et al. [2015], applied this technique to data obtained from 3 ADPVs co-located in the cross-shore direction and at different elevations. Dissipation rates range between $O(10^{-5})$ m^2 s^{-3} to $O(10^{-3})$ m^2 s^{-3} and increase towards the surface during uprush and towards the bed during backwash corroborating expectations of turbulence generation and dissipation related to the dominant forcing (bore-related and bed-related, respectively). Uprush dissipation away from the surf-swash transition is bed-related and does not show an obvious increase towards the surface as was found by Lanckriet and Puleo [2013]. Dissipation rates tend to increase with decreasing water depth [Lanckriet and Puleo, 2013; Raubenheimer et al., 2004; Sou et al., 2010].

2.1.2 Sediment transport and morphology

2.1.2.1 Sediment fluxes

Sensors do not exist to measure directly sediment flux. Instantaneous fluxes are derived from the product of concentration and velocity measurements [Aagaard and Hughes, 2006; Alsina and Caceres, 2011; Butt et al., 2009; Caceres and Alsina, 2012; Masselink et al., 2005; Masselink and Russell, 2006; Puleo, 2009]. Total load fluxes are obtained via vertical integration of the instantaneous fluxes. Net sediment transport at a particular horizontal location is quantified via time integration of the total load sediment flux. Net sediment transport over some time duration can also be obtained using sediment traps [Horn and Mason, 1994; Masselink et al., 2009], sediment tracers [e.g., Masselink and Russell, 2006] or pump sampling, truncated foreshores [Alsina et al., 2009; Othman et al., 2014], or spatially and temporally dense morphology measurements [Blenkinsopp et al., 2011; Masselink et al., 2009; Weir et al., 2006].

2.1.2.2 Suspension measurements

The main approach for measuring suspended sediment concentration (SSC) in the swash zone uses optics. Optical Backscatter Sensors [OBS; D&A and Campbell Scientific; Downing, 2006] and Fiber Optical Backscatter Sensors (FOBS; custom built; University of Washington) sensors emit infrared light that is backscattered off of particles suspended in the water column and received by a photodetector. Some researchers have developed their own optical sensors analogous to the FOBS [e.g. Miniature optical backscatter sensors; Butt and Russell, 1999, and subsequent work by these authors]. The FOBS and its variation provide SSC measurements with as small as 0.01 m vertical resolution. Individual OBS can also be nearly co-located with vertical resolution near 0.01 m, but with a larger footprint within the flow field. Current meters or acoustic velocimeters provide the advection velocity that when multiplied by the concentration at each elevation yields the instantaneous suspended sediment flux.

Optical sensors must be calibrated using sediment within the water column where they are located. Calibration can be difficult for a variety of reasons. Sediment from the bed is usually collected and assumed to be the material that is in suspension. This assumption is generally valid unless the sediment distribution is poorly-sorted (well-graded), bi-(multi) modal, or contains a significant fines or shell fraction. Calibrations are typically performed in a re-circulating vessel. Only certain size fractions may be suspended under the natural conditions whereas laboratory calibrations may suspend all size classes yielding an overestimate of the true sediment concentration.

For coarse sediments, the grains settle quickly making homogenous suspensions difficult to generate in the laboratory. Errors in suspension concentration manifest directly in the calibration. These errors can be circumvented if a viscous liquid, such as glycerol, [Butt et al., 2002] is used. Relating the optical qualities of the viscous liquid to those of water is needed in a second calibration step. Additionally, there is still some debate as to the effect of bubbles on optical sensors in the swash zone [Downing, 2006; Puleo et al., 2006] with bubble size likely a key factor. Puleo et al. [2006] suggest that bubble presence could render concentrations from optical backscatter sensors in error by 25 %. Still, optical sensors are probably the most appropriate for use in the swash zone because they are rugged and can provide reasonable concentration estimates over a fairly wide range up to several hundred g l^{-1}. Acoustic sensors are not generally used to measure SSC in the swash zone due to signal attenuation via bubbles. However, new, acoustic sensors [multi-frequency acoustic concentration and velocity profiler; ACVP ; Chassagneux and Hurther, 2014; Hurther et al., 2011] show promise in quantifying sediment concentration near the bed.

2.1.2.3 Sediment concentration and transport within a swash event

Sediment concentrations, for a free swash event, spike when a particular location is inundated through a rapid rise in water level (Figure 2.2e). Uprush suspended sediment concentrations can approach or exceed 100 g l^{-1} on steep and dissipative beaches [Aagaard and Hughes, 2006; Alsina et al., 2012; Alsina and Caceres, 2011; Caceres and Alsina, 2012; Hughes et al., 2007; Masselink et al., 2005; Masselink and Russell, 2006; Puleo, 2009; Puleo et al., 2014a] and may be more homogenous over the lower portion of the water column [Masselink et al., 2005; Puleo et al., 2014a, 2015, 2000; Ruju et al., 2016]. Meanwhile, sheet flow concentrations increase rapidly as the bed is sheared and dilates [Lanckriet et al., 2013; Puleo et al., 2014a]. Concentrations extend from the packed bed maximum or the enduring contact region typically defined as a volumetric concentration of 0.51 [1350 g l^{-1}; Bagnold, 1966b] to a dilute suspension typically defined as a volumetric concentration of 0.08 [212 g l^{-1}; Bagnold, 1966b]. Sheet flow thickness may extend over several centimeters whereas sediment suspension tends to extend across the swash-zone water column. Without measurements, velocities in the sheet flow layer are assumed to vary linearly from a near bed velocity to zero at the immobile bed location [Puleo et al., 2014a, 2015; Ruju et al., 2016] similar to research suggesting the velocity decays to the $\frac{1}{2}$ [Wang and Yu, 2007] to $\frac{3}{4}$ [Sumer et al., 1996] power with distance into the sheet flow layer. Corresponding sediment transport rates also peak at uprush initiation (Figure 2.2e). Instantaneous sediment fluxes in the sheet layer exceed those in the water column [Puleo et al., 2015; Ruju et al., 2016]. Sheet load is quantified by vertical integration from the immobile bed to top of the sheet layer. Suspended load is quantified by vertical integration from the top of the sheet layer to the free surface or highest measurement location. The vertical range of integration causes the suspended load transport to dominate sheet load transport during the majority of uprush [Puleo et al., 2015; Ruju et al., 2016].

The contribution of both transport modes is similar near flow reversal as sediment settles out of the water column and the sheet flow layer thickness decreases. Suspended sediment concentrations increase during backwash [Hughes et al., 2007; Masselink et al., 2005; Masselink and Russell, 2006; Puleo et al., 2015; Ruju et al., 2016] but generally to less magnitude than during uprush. Sheet flow sediment concentrations also increase during backwash [Puleo et al., 2015; Ruju et al., 2016] where the concentration profile is well-described by a linear profile with a power law tail [Lanckriet et al., 2013; O'Donoghue and Wright, 2004] regardless of the sheet flow thickness. The self-similarity of the sheet flow concentration profile may enable future efforts to utilize a near bed sediment concentration to infer the entire sheet flow profile if only the sheet flow thickness via multiple CCMs or CCM+ [van der Zanden et al., 2015] with individual probes separated for vertical coverage or from a predictive model [Dong et al., 2013; Lanckriet and Puleo, 2015; Malarkey et al., 2003; Wilson, 1987] is known. Sheet load transport exceeds suspended load transport rates throughout backwash [Puleo et al., 2015; Ruju et al., 2016]. The importance of sheet load transport is likely manifest by the dominance of bed-related rather than surface-related turbulence (Section 2.7). Suspended load does not occur near the end of the backwash as the thinning and decelerating flow loses capacity to suspend sediment. Instead, near bed sediment transport likely occurs as bed load in the last stages of backwash before the event terminates.

The previous description of sediment transport was for a free swash event. Swash interaction on beaches is a common occurrence. The general description of the swash motion is similar but the level and type of interaction on the foreshore plays a role in the sediment suspension processes [Blenkinsopp et al., 2011; Brocchini and Baldock, 2008; Caceres and Alsina, 2012; Erikson et al., 2005; Hughes et al., 2007; Jackson et al., 2004; Masselink et al., 2009]. Irregular wave forcing causes irregular swash interactions and alters the surf-swash boundary condition [Brocchini and Baldock, 2008; Guard and Baldock, 2006; Pritchard and Hogg, 2005] for effects on varying the seaward swash zone boundary conditions.

Caceres and Alsina [2012] (Figure 2.3) categorize interaction conditions as:

- a) Swash overtake (capture) where a large (faster) bore overtakes the swash tip. An uprush has not had sufficient time to reach flow reversal before the subsequent bore is able to propagate to and overtake the original swash edge extending the uprush motion. It is expected that sediment in transport from the original uprush will be incorporated into the overtaking bore and be transported onshore.

- b) Weak backwash / bore interaction where the bore overrides a preceding backwash. Backwash flow in these cases is weak and may have only been active for a short duration. Eventually the bore overtakes the backwash landward edge and initiates the ensuing uprush event. Large-scale laboratory results indicate weak backwash / bore interaction occurs most frequently when related to the high SSC events [Caceres and Alsina, 2012] and generally experienced net onshore transport. These types of interactions are common in the transition zone of dissipative beaches where multiple incident band swash events within an infragravity scale motion have numerous uprushes with onshore-directed sediment transport [e.g., Masselink et al., 2005].

- c) Strong backwash / bore interaction where the ensuing bore may be partially or fully slowed down or move offshore depending on flow conditions [Froude number; see also Elfrink and Baldock, 2002]. Strong backwash / bore interaction could lead to hydraulic jumps that are efficient sediment mobilizers [Butt and Russell, 2005]. These strong events produce the largest instantaneous SSC signals and net offshore suspended sediment transport especially when occurring in the trough of infragravity waves [Caceres and Alsina, 2012]. High sediment concentrations result from flow separation under the bore and associated turbulence that effectively homogenizes the water column [Elfrink and Baldock, 2002]. Strong backwash / bore interactions, like those for the weak interaction, are also common on dissipative beaches. In fact, a long duration backwash following multiple incident band weak bore interaction events leads to high SSC and strong interaction at the surf-swash boundary [e.g., Masselink et al., 2005].

2.1.2.4 Sediment advection and the importance of bore turbulence

Sediment transport rates are generally related to local conditions whereby the assumption of cross-shore advection is neglected. However, advection of sediment from the surf zone and or cross-shore advection due to the level of swash interactions (Section 3.2) can alter the sediment concentration at a particular location [Blenkinsopp et al., 2011; Caceres and Alsina, 2012; Jackson et al., 2004; Masselink et al., 2009]. Thus, both

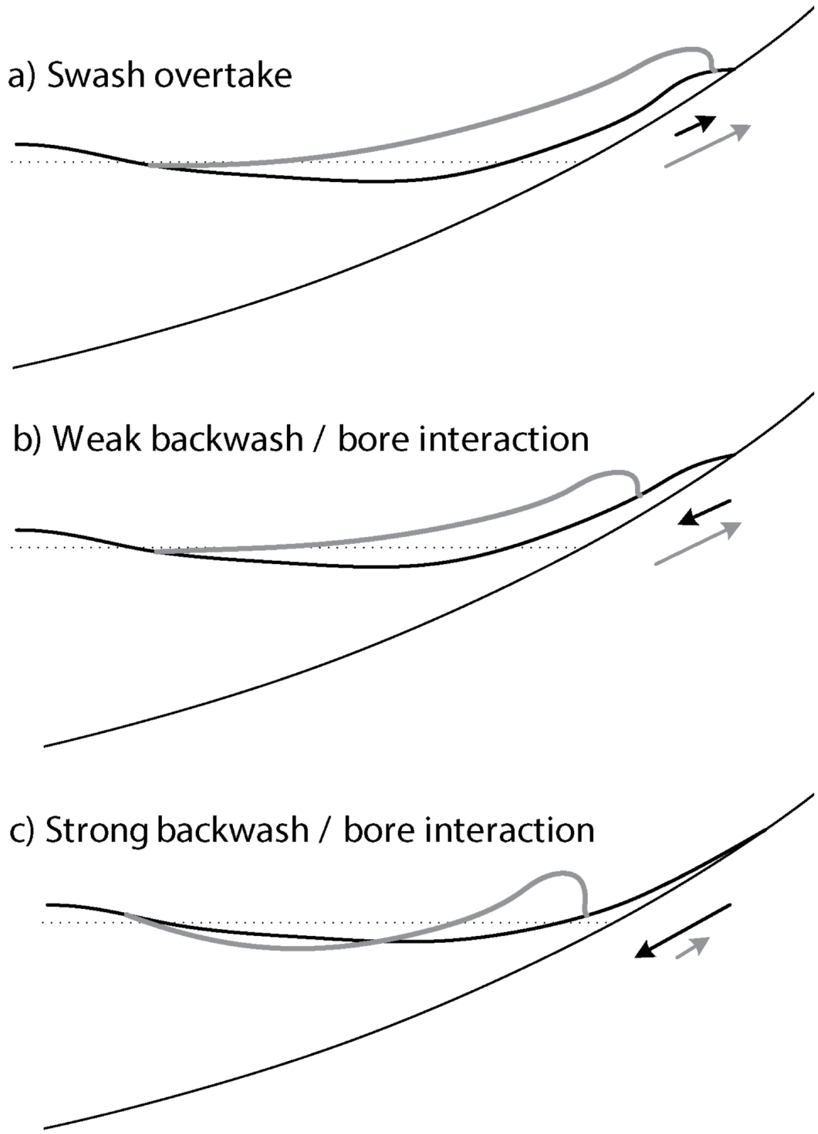

Figure 2.3. Schematic of interactions in the swash zone: a) swash overtake where a bore initializes a new swash event before the preceding swash event has experienced backwash; b) weak backwash / bore interaction where the bore propagates shoreward largely unimpeded by the preceding backwash; c) strong backwash / bore interaction where a rapid backwash flow collides with an ensuing bore possibly slowing the bore or causing a hydraulic jump. The thin black curve is the foreshore. The dotted line is the still water level. The thick black curve is the initial swash event. The thick gray curve is the ensuing bore motion. Arrows indicate the direction and scale of expected sediment flux. Adapted from Caceres and Alsina [2012].

mechanisms alter actual sediment transport rates. The sediment arriving at the swash zone from seaward is sometimes referred to as pre-suspended sediment [Hughes et al., 2007; Pritchard and Hogg, 2005]. Sediment trap data reveal that the maximum sediment transport load occurs just landward of the base of the swash zone for weak swash interactions and closer to mid swash locations for stronger swash interactions [Jackson et al., 2004]. These data suggest that sediment at the inner surf / swash zone transition are carried through the swash zone and may not have a swash zone origin. Masselink and Russell [2006] came to a similar conclusion using field data on dissipative and reflective beaches where the beaches accreted even though the mean flow was offshore-directed. The asymmetry of swash-zone velocities would seem to bias the net sediment flux offshore. This overshadows strongly sediment transport predictions as the net flux is commonly related to the mean velocity of the flow (e.g., Shields parameter) or to the velocity to some power (i.e., Bagnold type model). Some of the processes counteracting an offshore flux erosive tendency are the advection of pre-suspended sediment into the swash zone and settling lag effects of the sediment. Indeed, defining a settling lag parameter (e.g., ratio between the settling velocity of sediments and flow velocity) in numerical predictions together with an initial sediment concentration available for advection, can generate onshore net fluxes for a single swash event [Pritchard, 2009; Pritchard and Hogg, 2005]. The time-dependent suspended sediment supply at bore arrival and just after is a critical factor that has not been thoroughly examined. There is general agreement [Alsina et al., 2009; Brocchini and Baldock, 2008; Guard and Baldock, 2006; Hsu and Hanes, 2004; Hsu and Raubenheimer, 2006; Pritchard, 2009; Pritchard and Hogg, 2005] that the contribution of bore-related turbulence to sediment stirring capacity and sediment advection is dominant and must be investigated further. However, this contribution is rarely included in standard sediment transport models, and the turbulence field is absent or parameterized in most numerical model approaches for swash-zone sediment transport [Bakhtyar et al., 2009].

Bore turbulence is expected to affect the bottom when the bore height is less than half the local water depth [Hsu and Raubenheimer, 2006; Svendsen et al., 2000]. It follows that the active zone where the bore influence becomes relevant for sediment pickup and advection into the swash zone may be defined by physical characteristics of the bore (e.g., bore height and momentum) and a given (local) slope. The Pritchard and Hogg [2005] Lagrangian transformation of the SM63 solution, naturally allows the inspection of water parcel trajectories (that may also represent gross sediment motion) that are advected into the swash zone. Baldock et al. [2008] propose an advection length that is bounded within 0.4 to 0.5 times the runup distance seawards of the bore collapse limit. The advection length defines the pickup region from which fluid parcels can be carried into the swash zone. The ratio obtained from the analysis of laboratory and field data holds regardless of the forcing conditions [Baldock et al., 2008]. Alsina et al. [2009] conducted a novel laboratory experiment to address the concept of pre-suspended sediment. They utilized a fixed beach slope with a mobile bed near the bore collapse point. Traps could be installed at different locations on the foreshore to collect the pre-suspended sediment and determine how that sediment distributes across the swash zone during uprush. They found that 25 % of the pre-suspended sediment reaches the mid-swash position further demonstrating the importance of non-local sediment transport processes in the swash zone. The experimental results were also used to test a NLSW solver with an advection-diffusion equation for turbulence and suspended sediment in a Lagrangian reference frame. The advection-diffusion equation includes a settling velocity and eddy viscosity [following Kobayashi and Johnson, 2001]. A pre-suspended sediment concentration based on energy dissipation and stirring efficiency due to wave breaking and bed friction is supplied at the point of initial advection. The model although limited, (e.g. friction and turbulence efficiency factors are held constant), is able to predict an inflection point in the cross-shore distribution of sediment flux leading to beach accretion in the landward swash zone. Similar efforts are still needed in this regard under more resolved numerical approaches with less assumptions in the turbulence field (e.g. LES) or more appropriate parameterizations for the evolution of turbulence [e.g., rapid distortion theory vs. turbulent viscosity hypothesis, see molecular time scale responses for turbulent flows in Pope, 2000]. Moreover, the numerical modeling of swash-swash interactions and bound wave oscillations (e.g., surf beat) affecting the pre-suspended sediment loads is still an open topic for future research.

2.1.2.5 Sediment transport predictions

Predicting instantaneous or swash-event-integrated sediment transport has been attempted historically via energetics-type formulations [e.g., Bagnold, 1966a; Meyer-Peter and Müller, 1948]. The energetics formulations predict the total, suspended or bed load transport that is generally related to the velocity to some power. In the case of a power of 3 the transport is related to a shear stress velocity product where the shear stress arises from the quadratic drag law. Multiple recent papers have shown that this approach has limited applicability in the swash zone [Aagaard et al., 2006; Butt et al., 2005; Hughes et al., 2007; Masselink and Russell, 2006], although a few indicate moderate predictive capability [Masselink et al., 2009, 2005; Othman et al., 2014; Puleo et al., 2003b, some related to net sediment transport obtained via sediment traps or for ensemble-averaged events]. For example, some studies have shown the simple formulations fail to even predict the net sediment transport direction correctly, let alone the magnitude [Holland and Puleo, 2001; Masselink and Russell, 2006]. Other studies have shown the calibration coefficients between measured and predicted transport rates vary between uprush and backwash [Aagaard and Hughes, 2006] and discussed by [Masselink and Russell, 2006] and may vary depending on cross-shore location within the swash zone [Aagaard and Hughes, 2006]. On the one hand the inability to predict transport rates via the energetics approach is not totally surprising since the formulations were originally developed for steady, unidirectional flow conditions not met in the swash zone. On the other hand, incomplete measurements (coarse vertical resolution, lack of sheet flow measurements, incomplete temporal sampling for an entire swash event due to instrument difficulties) may hamper true testing of these simple formulations. The best validation may come from carefully controlled laboratory studies with high-resolution (vertical, cross-shore and time) measurements of the velocity profile, sheet flow transport, suspended sediment transport and morphological evolution.

A better representation of the processes controlling sediment transport can occur in more robust process-based numerical models. However, the time scale of interest will determine the degree of coupling (i.e., uncoupled, weakly or fully coupled) between hydrodynamic and sediment transport/morphological modules. The possibility for fully or weakly coupled approaches is suitable for individual swash events but the sediment transport estimates [Kelly and Dodd, 2010; Zhu and Dodd, 2013] may not differ from an uncoupled approach [Postacchini et al., 2014] given the short time scales involved. The improvements made from a fully coupled numerical approach become important under longer time scales. Recently, Zhu and Dodd [2015] developed a numerical model, coupling one-dimensional shallow water and bed evolution equations, with sediment advection (bed and/or suspended sediment load), to examine bed and suspended load transport. The numerical modelling of two swash events, a solitary wave and one event (overtopping wave) of Peregrine and Williams [2001], show the model capability to estimate swash-zone morphodynamics. The numerical solutions reveal that bed and suspended load have distinct morphodynamic signatures and that coupling both types of sediment transport does not affect significantly the solution. It is important to recall that these model results were based on idealized conditions where no flow interaction occurred and no bore turbulence effects were considered. Thus, more sediment would be entrained if these other processes were included. Other sediment transport models based on kinetic theory of collisional grain flow [e.g., Amoudry et al., 2008] may be suitable for predicting swash-zone sediment dynamics where sediment transport often occurs under large bed shear stress and large sediment concentrations. Under these conditions the particle-particle interactions become important and strongly coupled with fluid kinematics [Bakhtyar et al., 2009].

2.1.2.6 Modifications to simple transport formulations

Some studies acknowledged additional processes that are not included in the original energetics-type formulations that may enhance sediment transport. Differences between uprush and backwash calibration coefficients when calibrating the energetics-type formulations are more prevalent on steeper beaches. Bore turbulence [Aagaard and Hughes, 2006; Butt et al., 2004; Puleo et al., 2000] will enhance sediment transport and when included in the formulation as an additional mechanism increases the predictive ability [Aagaard and Hughes, 2006; Alsina et al., 2009]. Turbulence itself is not a force and thus must be included in conjunction with other terms. For instance, Aagaard and Hughes [2006] included the vertical velocity that was assumed to be largely related to turbulent fluctuations in their sediment transport estimate. Their approach quantifies bed shear stress as a product between the cross-shore velocity and the vertical velocity rather than through the typically used cross-shore velocity squared. The approach by Aagaard and Hughes [2006] is similar to that by Masselink et al. [2005] in that sediment transport predictions improved if a shear stress parameterization other than the quadratic drag law was used. Estimating the bed shear stress from a logarithmic velocity profile also caused there to be little variability between uprush and backwash calibration coefficients [Masselink et al., 2005]. Pedrozo-Acuna et al. [2006] found improvements to the predicted morphological response of a gravel beach, if friction factors dependent on flow phase are used. In their work however, the variation of the transport efficiency coefficients also served to parameterize other mechanisms such as infiltration effects. Hence the relative importance of varying friction coefficients was obscured by other more dominant processes as demonstrated in Jamal et al. [2014]. The inclusion of a simple infiltration model [Dodd et al., 2008; Packwood, 1983; Stoker and Dodd, 2006] resulted in significant improvements of the morphological response for the same case as Pedrozo-Acuna et al. [2006].

Butt et al. [2004] assumed the dissipated fluid power was related to turbulence and shear stress such that the sediment transport prediction was related to the cross-shore velocity times the sum of the shear stress and turbulence estimate. Although simple, the inclusion of turbulence in this manner improved the sediment transport prediction by 55 % when considering only bore events. However, more recent data from a large-scale laboratory study indicates that the suspended sediment concentration does not correlate well with TKE suggesting the empirical inclusion of TKE in swash-zone sediment transport formulations requires further study [Alsina and Caceres, 2011].

Cross-shore pressure gradients, mostly associated with a sloping sea surface, improved sediment transport predictions for coarse sand but not fine sands [Othman et al., 2014]. However, the transport coefficient was O(10) times larger than previously suggested values in the literature indicating that this effect may really serve as a proxy for some other process. Local accelerations, possibly related to pressure gradients, have also been hypothesized as enhancing sediment transport in the swash zone [Nielsen, 2002; Puleo et al., 2007] showing some improvement in predictions. But, local onshore-directed accelerations occur for only a limited portion of uprush near the location of swash initiation [Puleo et al., 2007] and cannot be related to the sloping sea surface pressure gradient that is seaward dipping for nearly the full duration of the swash event [Baldock and Hughes, 2006].

2.1.2.7 Total load from morphology

Subsection 2.1.2.3 described difficulties in quantifying sediment transport rates due to incomplete coverage throughout the water column. The sediment continuity equation can be used to infer net total load sediment transport rates across the swash zone from time-dependent morphology measurements [Alsina et al., 2012; Blenkinsopp et al., 2010b; Brocchini and Baldock, 2008; Masselink et al., 2010, 2009]. UDMs have been used to determine the bed level in between swash events [e.g., Blenkinsopp et al., 2011; Houser and Barrett, 2010; Masselink et al., 2009; Turner et al., 2008]. These sensors are appealing because they are inexpensive, robust, simple to use and can be deployed easily in an array to obtain cross-shore and alongshore variations in bed levels. LIDAR (Subsection 2.1.1.1) can also be used in this capacity to provide a dense cross-shore profile. Either data set, when differenced in time, yields a profile of the cross-shore gradient in sediment transport assuming alongshore uniformity. When measurements extend landward of the maximum runup region, the gradients are related to local total load sediment transport rates via discretization.

Masselink et al. [2009] and Blenkinsopp et al. [2011] used an array of UDMs across a high-energy beach to infer net sediment transport rates. Net sediment transport for a swash event could exceed 100 kg m-1 of beach. The inferred net sediment transport is only an order of magnitude smaller than the total sediment transport for the swash zone over an entire tidal cycle. Masselink et al. [2010] and Austin and Masselink [2006] found similar results for a steep beach fronted by a beach step. The fact that an individual swash event can transport such a large quantity of sediment relative to the total change over a tidal cycle is cause for concern given the current inability to predict swash-zone sediment transport rates. Large errors in any available sediment transport formulation will cause the predicted morphology to diverge rapidly from the true morphology.

2.1.2.8 Morphologic variability

Puleo et al. [2014b] provide an overview of the different techniques to quantify bed level change. UDMs, CCPs and LIDAR were already identified in earlier sections. The most straightforward approach to quantify bed level changes is the use of stakes embedded in the foreshore and sampled at some specific time interval [Austin and Buscombe, 2008; Austin and Masselink, 2006; Kulkarni et al., 2004]. Time-sequenced imagery through stereo-metric intersection [Holland and Puleo, 2001] has been used to map foreshore elevations as identified through successive shoreline position digitization. Data were compiled to identify the foreshore morphology every 15 minutes since errors in geometrical image rectification and the procedure were not conducive to identifying the bed level change for a particular swash event. Laboratory swash-zone studies using stereo-metric approaches provide highly accurate and dense morphology measurements in between swash events [Astier et al., 2012; Astruc et al., 2012]. This method is probably the most accurate of the non-intrusive methods with elevation errors < 1 mm. However, the technique requires careful instrument set up and imagery positioning. It is not clear the technique can be used under field conditions and like other non-intrusive methods can only measure the morphology when the beach surface is exposed. Other approaches use a combined imaging/LIDAR system to monitor the foreshore elevation on a wave-by-wave time scale [Vousdoukas et al., 2014]. The inclusion of LIDAR reduced image registration errors by an order of magnitude. The advent of UDMs, CCPs and LIDAR may indicate the imaging approach obsolete for short term field investigations of high-frequency bed level change in the swash zone.

Section 3.6 discussed a method to extract sediment transport rates from dense swash-zone morphology measurements. There are also interesting signals in the morphologic variability obtained from these detailed measurements. On beaches with little to moderate net beach change the local bed level can fluctuate up (accretion) or down (erosion) by up to several centimeters for a particular swash event [Blenkinsopp et al., 2011; Houser and Barrett, 2010; Masselink et al., 2010, 2009; Puleo et al., 2014b; Ruessink et al., 2016]. The ability for a particular swash event to cause these changes means that perhaps only one or a few swash events are able to alter the final morphological configuration of the foreshore over a tidal cycle [Blenkinsopp et al., 2011; Caceres and Alsina, 2012; Masselink et al., 2009; Puleo et al., 2014b].

Blenkinsopp et al. [2011] analyzed swash-zone bed level variability using UDM data collected from a high energy steep beach. The foreshore accreted at a particular location by 60 mm over one tidal cycle. Roughly 60 % of the individual bed level changes for individual swash events were within 2 mm relative to the initial bed level. Over 90 % of the bed level changes for a particular event were within 10 mm of the initial bed level. Distributions of single swash event bed level change for all measured tides were found to be nearly Gaussian regardless of whether or not the beach exhibited net erosion or accretion. Puleo et al. [2014b] found similar nearly Gaussian distributions of individual swash event bed level variability on a high energy macrotidal beach. The net change over a tidal cycle in the Puleo et al. [2014b] study was less than 10 mm but some individual swash event bed level changes exceeded 20 mm erosion or accretion. Puleo et al. [2014b] further categorized individual swash events as having negligible or large (7 mm) net elevation change. Swash events that exhibited negligible net elevation change had velocity time series that were symmetric with respect to uprush and backwash duration and uprush and backwash maximum cross-shore velocity. Large accretion events had a shorter uprush duration relative to backwash with weaker uprush vs. backwash cross-shore velocities. In contrast, large erosion events had longer uprush vs. backwash duration and stronger uprush velocities. These findings may be opposite of those expected. However, the cross-shore location where data were sampled likely plays a key role in overall bed level changes and how they may be related to underlying hydrodynamics [Aagaard and Hughes, 2006; Blenkinsopp et al., 2011; Houser and Barrett, 2010; Puleo et al., 2014b].

UDMs sample the bed level in between swash events when the bed becomes exposed. CCPs have the ability to also sample the bed level at high resolution during a swash event providing insight into intra-swash bed level variability [Puleo et al., 2014b; Ruessink et al., 2016]. Instantaneous bed level elevations were nearly normally-distributed similar to findings for inter-swash bed level changes. Spectral calculations of the bed level time series showed no significant peaks at the same frequencies as the peaks for incident or infragravity hydrodynamic parameters. The spectrum displayed an f^{-2} roll off across 2 decades of frequency with no inertial subrange. The f^{-2} roll off corroborates the roughly Gaussian distribution of bed level change observed in this and the other studies of bed level change using UDMs cited earlier.

The foreshore variability also has an interplay with the beach step dynamics [Austin and Buscombe, 2008; Austin and Masselink, 2006; Kulkarni et al., 2004; Masselink et al., 2010]. The step is more prominent on the rising tide and migrates landward as the tide rises. Its amplitude decreases and it migrates offshore during the falling tide. More detailed analyses suggest the step and foreshore evolve in different phases. Kulkarni et al. [2004] indicated an initial erosion phase of the foreshore upon tidal inundation before the foreshore accretes throughout the rest of the rising tide. There was then slight erosion with offshore step migration while the rest of the foreshore remained relatively stable. The different phases were tied largely to water table fluctuation in the coarse-grained beach. Austin and Buscombe [2008] indicated the initial change on the rising tide is step growth and foreshore erosion. The step continues to increase in volume with rising tide while the foreshore region experienced little to no change in volume. At high tide, the step and foreshore are in near equilibrium with the waves and experience little change in volume with some slight foreshore accretion. Both the step and foreshore experience a decrease in volume as the tide level drops. The study also indicated that grain size distribution at a particular location might change on the wave time scale. The grain size variability could enhance or hinder sediment transport for similar forcing conditions suggesting that knowledge of the time-dependent sediment distribution may be needed (e.g. friction factor) for accurate sediment transport predictions.

2.1.3 Summary

In the last decade, numerous research efforts have expanded our knowledge of small-scale swash-zone hydrodynamics and sediment transport processes. Recent descriptions of the complex and dynamic system have been possible thanks to advances in sensor technology and novel approaches in field, laboratory and numerical modeling studies. This review paper discussed recent advances that have occurred but there are still numerous knowledge gaps, for example:

1. Advances have been made regarding sediment concentration specifically in direct proximity of the bed. Sediment flux estimates near the bed and in the water column are less advanced due to coarse resolution or general lack of ability to quantify velocity in the sheet flow layer. Little advancement in predicting swash-zone sediment transport from simple formulations has occurred. This aspect of swash-zone research is viewed by the authors as one of the most pressing problems facing swash-zone researchers.

2. The approach of reducing the temporal scale to a single swash event (e.g. dam break) to focus on processes occurring on a wave-by-wave time scale has helped highlight the important processes occurring in the swash zone. However, less attention has been paid to the inherent interactions that take place near the surf-swash transition or through swash-swash interaction.

3. The majority of swash-zone research has focused on cross-shore processes including sediment transport, bed shear stress and turbulence. There has been limited progress on how alongshore flows affect these processes.

4. Recent research has focused generally on small-scale processes over short temporal durations. Upscaling understanding/predictions of these small-scale processes to longer term events such as storms is a major challenge.

5. Swash-zone numerical models span a broad range in degree of sophistication (e.g., depth-averaged, depth-averaged boundary layer, depth-resolving, LES). Selecting a numerical model may be more related to the subject of interest, time constraints and computational effort rather than to model limitations. The common numerical models have been validated and may be used to assist in understanding hydrodynamic parameters. However, the prediction of net sediment transport

fluxes and morphological response are still based on limited formulations. Potential improvements may come from fully (or weakly) coupled approaches but have yet to be tested for longer time scales and/or more realistic settings. Few depth-resolving models have focused on sediment transport prediction and their contribution may be limited to short time scales (several swash events).

Chapter 3

INNER-SURF AND SWASH-ZONE MORPHODYNAMICS DURING ACCRETIVE CONDITIONS ON A STEEP SLOPING BEACH

3.1 Introduction

The inner surf zone is characterized by periodic bores generated from breaking waves and extends to the instantaneous shoreline thereby encompassing the swash zone [Svendsen et al., 1978]. The swash zone is the area of the nearshore that is intermittently inundated [submerged less than 90 % of the time; Aagaard and Hughes, 2006; Blenkinsopp et al., 2011; Hughes and Moseley, 2007; Masselink et al., 2009; Masselink and Russell, 2005], as a result of wind- and wave-induced water level variability. The swash zone is characterized by highly variable shallow and ephemeral flows frequently laden with sediment and bubbles. The spatial extent and location of the swash zone is not constant and varies on times scales from incident waves to tides. Flows within the inner surf and swash zones control sand exchange between the surf zone and foreshore leading to foreshore morphologic variation. Quantifying, using *in situ* measurements, the hydrodynamic and sediment transport processes in these zones is difficult due to the high levels of turbulence and rapidly changing bed levels either leading to burial of instruments or instruments being located too far away from the bed to capture the majority of the flow cycle. However, progress in instrumentation and measuring techniques/approaches has improved understanding of inner-surf and swash-zone morphodynamic processes across a range of spatial and temporal scales.

Much of the knowledge on inner-surf and swash-zone sediment transport processes and morphologic change on sandy beaches arises from field studies that focus on cross-shore suspended sediment transport rates (or fluxes) or net cross-shore sediment fluxes. Suspended sediment transport rates are derived from the product of co-located concentration and velocity measurements [Aagaard et al., 2006; Butt et al., 2004; Masselink et al., 2005; Masselink and Russell, 2006; Puleo, 2009; Puleo et al., 2014a, 2000]. Suspended sediment concentrations were obtained using optics (i.e., optical or fiber optical backscatter sensors) and fluid velocities using electromagnetic current meters or acoustic Doppler sensors at a fixed elevation above the bed. Most studies using co-located instrumentation estimated sediment transport rates at a single or a few cross-shore locations [Aagaard and Hughes, 2006; Butt et al., 2009; Lanckriet et al., 2014; Masselink and Russell, 2005, 2006; Puleo, 2009; Puleo et al., 2014a].

Net sediment flux can be estimated through integration of sediment transport rate time series or from precision bed-level change measurements [Blenkinsopp et al., 2011; Houser and Barrett, 2009b; Masselink et al., 2009; Puleo et al., 2014b]. Ultrasonic distance meters (UDM) are often used to measure bed level elevation in the field [Blenkinsopp et al., 2011; Masselink et al., 2009]. Deployment of cross-shore arrays of these sensors enables the estimation of net cross-shore sediment flux over time scales ranging from individual swash events to tidal cycles using inversion of the sediment continuity equation [Blenkinsopp et al., 2011; Masselink et al., 2009]. However, these sensors quantify bed level elevation only when the bed is exposed.

The insights gained from field-based research have indicated that: (a) onshore-directed flows, compared to offshore-directed flows, tend to have larger velocities [e.g., Butt et al., 2009; Hughes et al., 1997; Masselink and Russell, 2006; Puleo et al., 2014a, 2012], larger bed shear stresses [e.g., Austin et al., 2011; Barnes et al., 2009; Miles et al., 2006; Puleo et al., 2014a], high levels of turbulence due to bore entrainment/collapse [e.g., Aagaard and Hughes, 2006; Butt et al., 2004] enhancing suspended sediment concentrations; (b) the difference between onshore- and offshore-directed sediment transport lead to net morphological change [e.g., Blenkinsopp et al., 2011; Masselink et al., 2009; Puleo et al., 2014b]. Previous efforts focused on small-scale processes provided new insights about inner-surf and swash-zone morphodynamics related to a specific cross-shore location. The cross-shore location where data were sampled plays a key role in overall bed level changes and how those changes are related to the underlying hydrodynamics [Aagaard and Hughes, 2006; Blenkinsopp et al., 2011; Houser and Barrett, 2010; Puleo et al., 2014b]. Foreshore elevations can fluctuate down (erosion) or up (accretion) by up to several centimeters for a particular swash event [e.g., Blenkinsopp et al., 2011; Houser and Barrett, 2010; Masselink et al., 2009; Puleo et al., 2014b]. The result is that only one or a few inner-surf/swash events may alter the final morphologic configuration of the foreshore over a tidal cycle [Blenkinsopp et al., 2011; Caceres and Alsina, 2012; Masselink et al., 2009; Puleo et al., 2014b]. Inner-surf and swash-zone events that exhibited negligible net elevation change had velocity time series that were symmetric with respect to onshore- and offshore-directed flows. Erosive events tend to have shorter (slower) onshore-directed duration (velocity) than the offshore-directed flow. In contrast, accretive events tend to have a longer (larger) onshore-directed duration (velocity) than the offshore-directed flow [e.g., Masselink et al., 2009; Puleo et al., 2014b]. Less attention has been paid to the contribution of alongshore flows. Austin et al. [2011] and Puleo et al. [2014a] showed that alongshore velocities could be of similar magnitude or exceed cross-shore velocities and emphasized that both flow motions can contribute to sediment transport.

Much prior research has focused on inner-surf and swash-zone processes under erosive conditions [e.g., Bonte and Levoy, 2015; Butt and Russell, 2005; Duncan Jr., 1964; Holland and Puleo, 2001; Vousdoukas et al., 2012; Vousdoukas, 2012]; partially because the signals are large and obvious. It is generally recognized that under highly energetic conditions the foreshore erodes as a result of surf zone processes [Aagaard and Greenwood, 1995]. Inner-surf and swash-zone processes are more likely to alter the backshore region of the beach (even the fore dunes), depending on the wave set-up. Less attention has been paid to post-storm recovery or accretive processes where the time scales are longer or the signals are not as large. Foreshores do have the capacity to repair themselves following erosive events. Under calm energy conditions (i.e., post-storm), surf-zone, inner-surf and swash-zone processes are important in controlling the foreshore morphodynamics [Baldock and Alsina, 2013].

Past field-based studies have reported that surf zone sandbars tend to migrate rapidly onshore consequently accreting the foreshore (steep slope) due to tidal variation, offshore wave energy level and direction, flow asymmetry, swash overtopping, among others [Greenwood et al., 2004; Houser and Greenwood, 2007; Russell et al., 2009; Vousdoukas et al., 2011; Weir et al., 2006]. However, these findings are often based on large-scale morphological change measurements (i.e., repeat elevation surveys) rather than determination of the magnitudes or direction from either local instantaneous sediment transport rates or net sediment transport rates. Small-scale processes should be related to larger spatial and temporal domains (e.g., entire foreshore) to understand the accretion process of foreshores as governed by inner-surf and swash-zone dynamics. A dense array of hydrodynamic and sediment concentration sensors deployed at multiple cross-shore locations across the foreshore are needed to relate the small-scale processes to larger temporal and spatial scale accretive patterns.

In this study concurrent near-bed hydrodynamic and sediment concentration measurements at 5 cross-shore locations across the foreshore were collected during post-storm recovery. The measurements provided an opportunity to illustrate a number of inner-surf and swash-zone phenomena on a steep foreshore under accretive conditions. The main objectives of the experiment were: (1) estimate cross-shore and alongshore hydrodynamic and sediment transport parameters in the inner surf and swash zones; (2) provide improved knowledge of the spatial and temporal variation of the inner-surf and swash-zone suspended sediment transport processes under accretive conditions; and (3) estimate and predict the net suspended sediment transport using *in situ* measurements and an energetics formulation.

3.2 Methodology

3.2.1 Field site and hydrodynamic conditions

Field data were collected at South Bethany Beach, Delaware, USA (N 38° 30.66’, W -75° 03.13’; UTM: 4262522 m N, 495453 m E) from February 12 to February 25, 2014 (Figure 3.1a). Measurements during the field study were referenced to a local coordinate system with the cross-shore distance, x, increasing onshore and alongshore distance, y, increasing to the south. South Bethany Beach is a steep, meso-tidal beach with a semi-diurnal tide and a mean oceanic tidal range of 1.5 m. Mean sea level near the study area is -0.11 m (North American Vertical Datum; NAVD88).

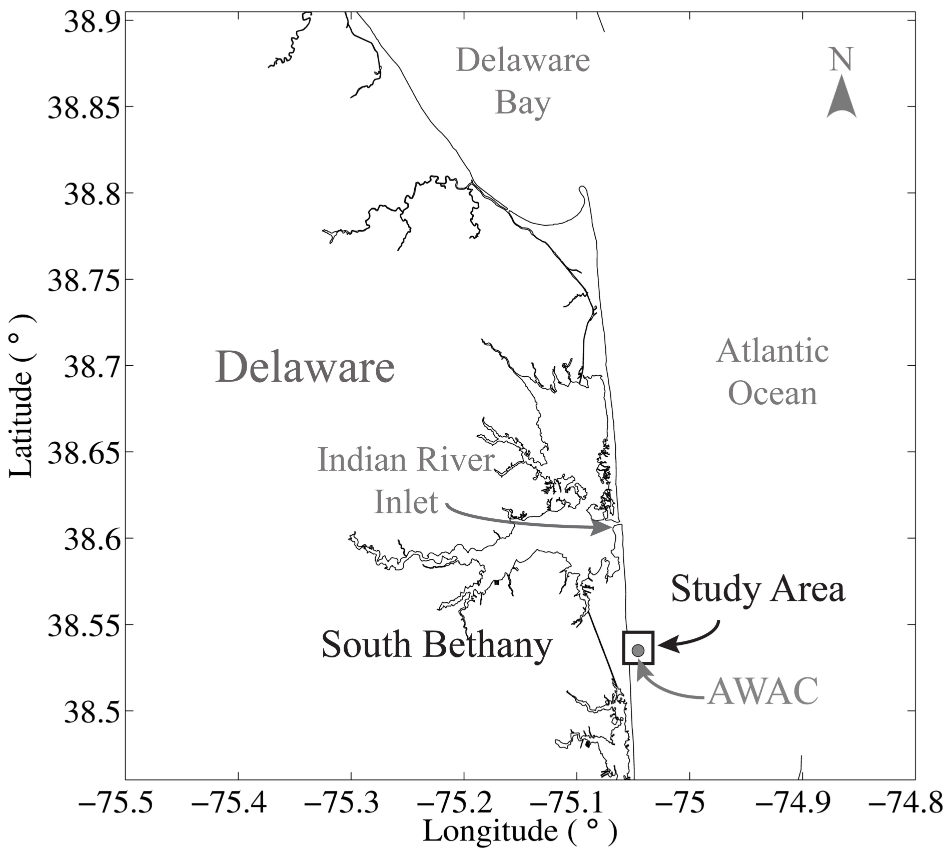

Figure 3.1. Digitized shoreline section of the Delaware coast showing the location of South Bethany Beach, Delaware, the study area (black square) and deployed wave sensor (AWAC).

Waves at the study site are short period (7 - 9 s) and small amplitude (0.5 - 1 m), with a dominant southeast direction (recorded by BTHD1 buoy roughly 0.65 km offshore; National Data Buoy Center-Station Bethany Beach, DE; www.ndbc.noaa.gov). Additional nearshore wave measurements (Figure 3.2) were collected during the study in approximately 6 m water depth using a bottom-mounted current profiler and wave directional system (Nortek 2MHz AWAC; Figure 3.1). Waves were measured in bursts of 1024 samples (at 2 Hz for 8.5 minutes) every 60 minutes. Time series of significant wave height (H_s), wave period (T_p), and wave direction (D_p) were obtained through data post-processing using a surface tracking and U & V velocity (SUV) method.

A Nor'easter storm struck the US East Coast from Feb. 12 - 14, 2014 and generated waves over 5 m (Figure 3.2i). The maximum significant wave height observed was 5.5 m with a peak period of 10 s. Northeast wind gusts reached 26 m s^{-1}. No inner surf/swash zones measurements were collected during this time due to the energetic/dangerous wave conditions and severe erosion. The waves subsided after Feb. 14 with conditions favorable for beach recovery. Hydrodynamic and suspended sediment concentration measurements were collected from Feb. 16 - 25, 2014 (Figure 3.12ii). Maximum wave heights were 1.5 m during this time period and were generally from the southeast (Figure 3.2i).

3.2.2 Sensor deployment

A 40 m long scaffold frame was installed ranging from seaward of the low tide line to landward of the berm. Five stations (Figure 3.3a) were established to measure concurrently, inner-surf and swash-zone velocity, water depth, and suspended sediment concentration. Highly resolved near-bed velocity profiles were recorded with five downward-looking Nortek Vectrino II Acoustic Doppler Profiling Velocimeters (ADPV). These sensors have the capability to profile the three velocity components (u, v, w corresponding to the cross-shore, x, alongshore, y, and vertical, z, directions,

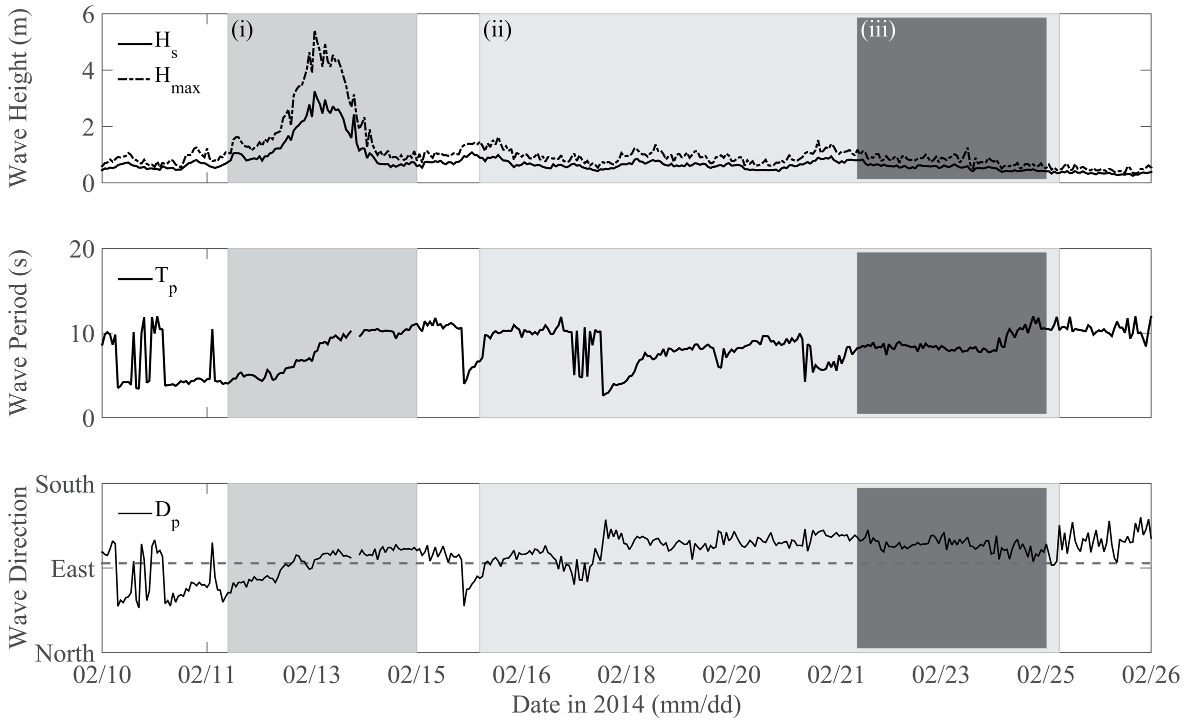

Figure 3.2. Wave conditions during the study period: (a) significant (H_s) and maximum wave height (H_{max}) estimated each hour; (b) wave period (T_p); (c) wave direction (D_p); horizontal dashed line is shore normal incidence. Gray shading in all panels indicates: (i) Noreaster event; (ii) data sampling period; (iii) period analyzed.

respectively) over a total vertical range of 0.03 m at 0.001 m spacing at 100 Hz. For consistency throughout the paper, cross-shore flow within the inner surf and swash zones are referred to as onshore-directed (also known as uprush) or offshore-directed (also known as backwash). For this study, the profiling range started 0.04 m below the transducer such that the initial velocity profile intersected the bed. Each station also included a Druck PTX1830 pressure transducer (PT), located in the direct vicinity of the bed, to determine the local water depth after accounting for the sensor elevation relative to local bed level changes. Suspended sediment concentration (SSC) was recorded using Campbell Scientific optical backscatter sensors (OBSs), collocated with an ADPV at each station. At three stations (1, 2, and 4), a pair of OBSs was deployed at 0.035 and 0.085 m above the initial bed level, whereas at the other two stations (3 and 5) only one OBS was deployed at 0.035 m above the initial bed level. The PTs and

OBSs were sampled at 16 Hz. All *in situ* sensors recorded data only when the water level reached or exceeded their elevation. Due to rapid morphological changes, the local elevation of each sensor above the bed was measured and adjusted vertically, as necessary and when possible during daylight hours. Severe cold weather, icy conditions (below -1° C) and snowfall during the field study increased the difficulty of measuring and adjusting the sensor elevations (Figure 3.3a).

A 5-m aluminum-imaging tower was located 62 m landward of station 1. A Sony DFW-X710 IEEE1394 protocol (rewire) visible-band, red-green-blue (RGB) camera with a 1024 x 768 pixel array was affixed to the tower. Images were sampled at 4 Hz during daylight hours and only under calm wind conditions. Camera pan and tilt was controlled remotely and live video feed and acquisition was through dedicated computers located inside a field trailer. Images were geo-referenced into the local coordinate system following the method of Holland et al. [1997]. A cross-shore pixel transect just North of the scaffold frame was identified to quantify the runup excursion [e.g., Aagaard and Holm, 1989; Holland et al., 1995; Holland and Holman, 1993; Holman and Stanley, 2007; Puleo, 2009]. All sensors on the scaffold frame were cabled into the field trailer for power, control and data acquisition. Sensor data were recorded on individual laptop computers. Time synchronization between laptops and sensors was achieved using a Trimble GPS antenna, and Dimension4 and Tac32 software.

3.2.3 Beach profile variability

Beach profile data were collected twice per day around low tide, using a real-time kinematic (RTK) Leica GPS system mounted on a rolling dolly. The field surveys consisted of cross-shore and alongshore transects at roughly 3 m horizontal spacing with areal coverage spanning 100 m on either side of the main measurement transect. Sampling extended into the water to an elevation of approximately 0.5 m below MSL when conditions permitted. Survey data were referenced to UTM zone 18 (NAVD88 for vertical and North American Datum, NAD83 for horizontal). Examples of daily

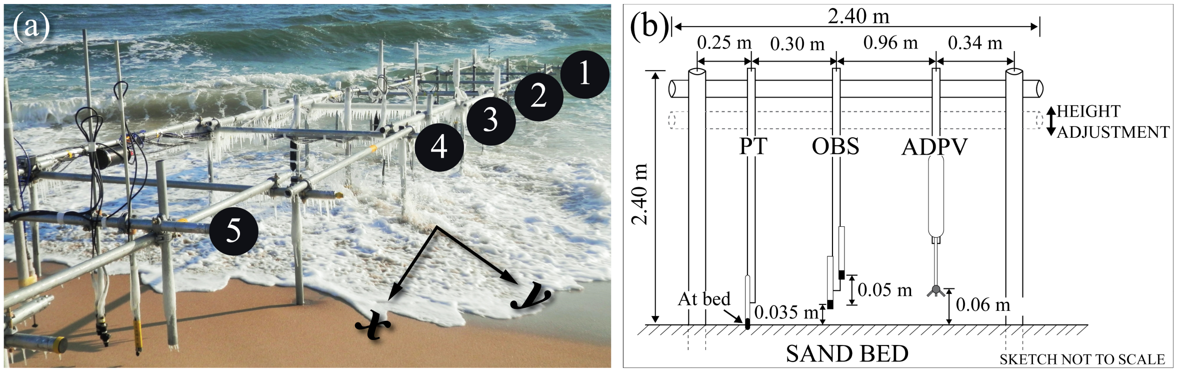

Figure 3.3. Sensor setup: (a) image showing the cross-shore extent of the scaffold frame covered with icicles in the swash zone at roughly mid tide and the location of the five sensor stations; and (b) a sketch showing an example of the sensor setup at each station.

morphological variability during the study period are shown in Figure 3.4. Data were cast into a local horizontal coordinate system to simplify comprehension of distances. The cross-shore coordinate (x) increases landward ($x = 0$ at the beginning of the scaffold frame) and the vertical coordinate (z) increases upward ($z = 0$ at mean sea level). Foreshore slope ($tan\beta$) was defined as the elevation gradient between the mean sea level ($z = 0$) and the maximum berm elevation. Energetic conditions ($H_s = 3$ m; $H_{max} = 5.5$ m; $T_p = 10$ s) during the Noreaster eroded the berm by 0.7 m and flattened the foreshore profile to approximately half its pre-storm slope ($tan\beta$ reduced from 0.13 to 0.05; Figure 3.4b). Beach recovery began even as the storm was subsiding with rapid accretion in contrast to general expectations for beach recovery during calm conditions (Figure 3.4c). Accretion of the foreshore continued over the duration of the field study, but only several waves overtopped the berm. Surface sediment samples were collected along the scaffold frame at 3 m intervals to determine the size distribution of sediment along the foreshore. The median grain size, d_{50}, was 0.4 - 1.0 mm. The coarsest sand was found at the seaward location of the scaffold frame and the grain size progressively decreased in the landward direction.

The primary objective of the field study was to measure ridge and runnel system evolution/migration through overwash after a storm event. However, few waves overtopped the ridge (Figure 3.2ii) and no landward migration was observed. Thus, sensors that were originally placed on the landward flank of the ridge to capture this potential migration were moved to the foreshore on the seaward ridge flank leading to the time period of interest for this study (Figure 3.4d; Figure 3.2iii). Data described hereafter were collected from Feb. 22 to 24, 2014 (Figure 3.2iii) and were examined to quantify cross-shore and alongshore dynamics within the inner surf/swash zones on a steep accreting beach.

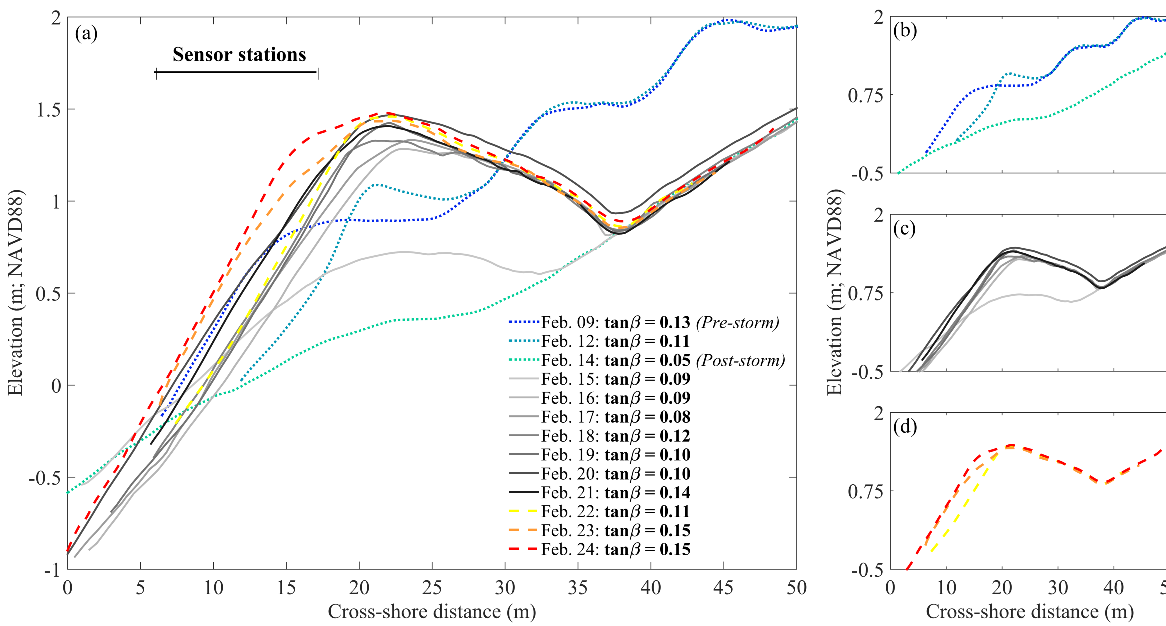

Figure 3.4. (a) Beach profiles collected during the second low tide of the day with mean sea level at $z = 0$ m: (b) green tone dotted lines depict the elevation from pre- to just post- storm, (c) gray tone lines depict the post- storm recovery period, (d) orange tone dashed lines depict subsequent recovery and identify the time period for data analyzed.

Foreshore profiles representing the daily changes of Feb. 22 - 24, 2014, are shown in Figure 3.5 to facilitate interpretation of Figure 3.4 during the time period analyzed. The accreting conditions during calm wave conditions (Figure 3.2iii) led to a steepening of the foreshore slope from $tan\beta = 0.11$ to $tan\beta = 0.15$. The elevation difference ($O(10^{-1}$ m)) between surveys reduced during the experiment with negligible changes at the landward portion of the foreshore (Figure 3.5b to 3.5d). The largest foreshore elevation difference ($dz = 0.23$ m) between successive surveys was observed on Feb. 22 (Figure 3.5b). The negligible changes at the landward portion ($x > 13$ m) were mostly due to the steepening of the foreshore, which affects the swash excursion distance.

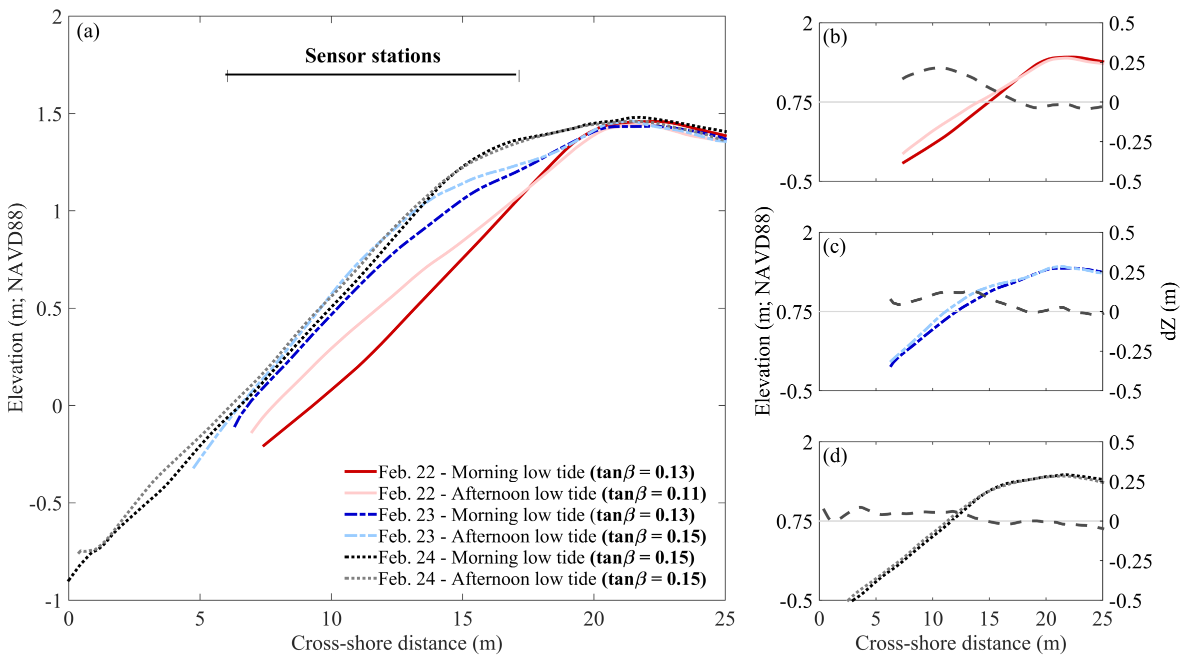

Figure 3.5. (a) Foreshore section of the beach profiles collected twice per day around low tide from Feb. 22 to Feb. 24: (b) red tone lines depict the foreshore elevation measured on Feb. 22, (c) blue tone dotted lines depict the foreshore elevation measured on Feb. 23, (d) gray tone dotted lines depict the foreshore elevation measured on Feb. 24. Dashed gray lines in panels (b) to (d) depict the elevation difference (y-axis on the right side) between the two foreshore profiles.

Alongshore variability was quantified from the surveyed bed elevation along 10 cross-shore profiles (Figure 3.6a white dashed lines). Foreshore profiles showed little alongshore variation with standard deviations of $O(10^{-2}$ m) (Figure 3.6b 3.6d). These estimates suggest that the morphological changes observed in Figure 3.5b to Figure 3.5d were mainly incited by cross-shore sediment transport gradients rather than alongshore sediment transport gradients. Therefore, the analysis of morphological changes focuses on cross-shore sediment transport gradients (Subsection 3.4). However, alongshore hydrodynamic and sediment transport parameters are presented as they are still important for suspended sediment transport processes on beaches.

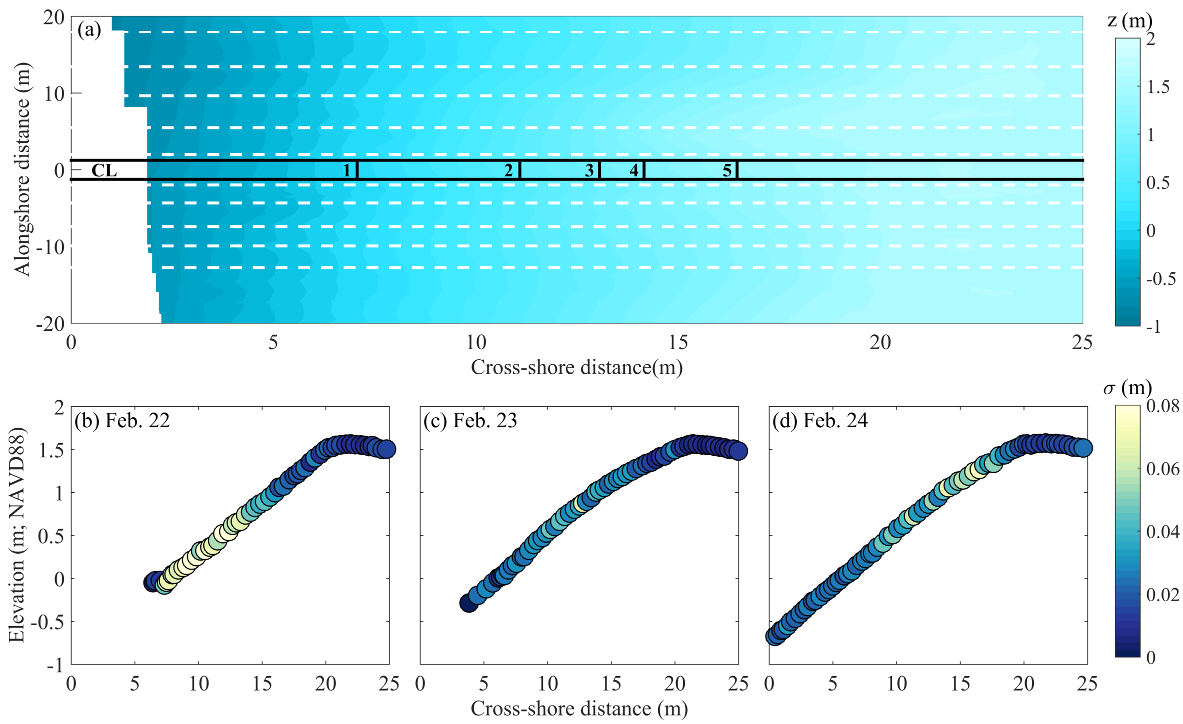

Figure 3.6. (a) Location of the cross-shore transects selected to quantify alongshore variation (white dashed lines). The solid black horizontal line indicates the cross-shore extent of the scaffold frame, the vertical black lines the location of the sensor stations, and color scheme depicts the foreshore elevation for Feb. 24 (as example); and (b-d) standard deviation, σ, of the alongshore variability along 10 cross-shore profiles for Feb. 22 to Feb. 24, respectively.

3.2.4 Data processing

PT data were corrected for atmospheric pressure and converted to water depth using gains and offsets determined by a laboratory pressure calibration test. The water depths were corrected to account for sensor vertical adjustment. The OBSs were calibrated in the laboratory with uniform suspensions produced using the surface sediment samples collected adjacent to their deployment position. OBS data were removed from the record when the water depth, measured by the PT, was less than the sensor elevation. Raw ADPV time-series records were quality controlled to remove unreliable data attributed to Doppler noise and signal discontinuity (intermittent submergence of instrumentation and/or flow laden with bubbles and sediment) [Aagaard and Hughes, 2006; Elgar et al., 2005; Lanckriet and Puleo, 2013; MacVicar et al., 2007; Puleo et al., 2012; Raubenheimer, 2002]. Previous research has suggested methods to quality-control acoustic Doppler data using phase-space despiking [Goring and Nikora, 2002; Mori et al., 2007], low-pass third-order Butterworth filter [Roy et al., 1997], or internal data quality parameters such as beam amplitude, signal to noise ratio, and correlation score [Alsina et al., 2012; Caceres and Alsina, 2012; Hughes and Baldock, 2004; Inch et al., 2015; Lanckriet and Puleo, 2013; Puleo et al., 2012; Raubenheimer, 2002]. Here, near-bed velocity measurements were rejected when beam amplitudes were below -20 dB and the correlation score was below 40 %. A velocity difference between two subsequent measurements of greater than 0.5 m s^1 was used as a threshold value to remove spikes and spurious data from ADPV signals [Inch et al., 2015; Puleo et al., 2014a]. Figure 3.7 shows an example of raw ADPV velocity measurement (Figure 3.7b) exhibiting signal noise and the quality-controlled velocity (Figure 3.7c) after removing the unreliable data. The gaps in the ADPV signal indicate that the free surface elevation was less than that of the sensor (Figure 3.7a), intermittency in the measurements, and the difficulty in capturing velocities in aerated and turbulent flows (i.e., initial stages of onshore-directed flow).

A percentage of velocity measurements were retained from each station following quality control procedures. Five-minute data segments of the percentage of data retained (signal discontinuity) are indicative of the highly dynamic and turbulent motions (Figure 3.8). At station 1, the majority of the velocity data was retained because the instrument station was located in the inner surf zone being submerged throughout most of the study period. Meanwhile, the percentage of data retained decreased at the other stations with generally less data retained with increasing onshore distance.

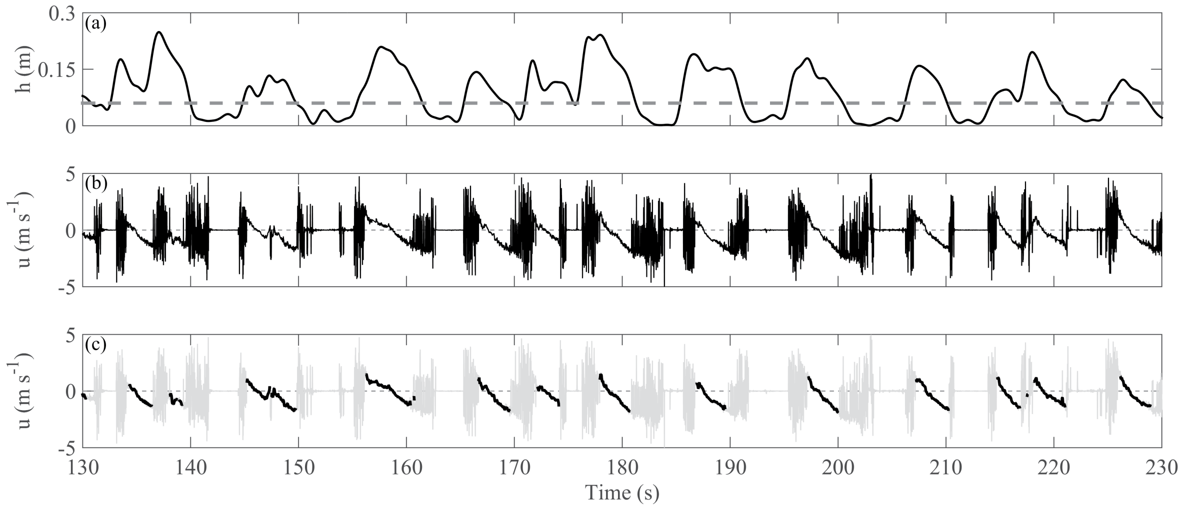

Figure 3.7. Time series excerpt of (a) PT water depth measurement; (b) ADPV raw velocity measurements; and (c) ADPV quality-controlled velocity measurements. The horizontal dashed line in top panel marks the local elevation of the ADPV sensor. The gaps in the bottom panel show the intermittent nature of swash motions.

Thus, the gaps in the velocity time series were a source of uncertainty in estimating suspended sediment transport rates and the associated morphological change. Reconstruction of velocity time series was necessary in an effort to replace removed data.

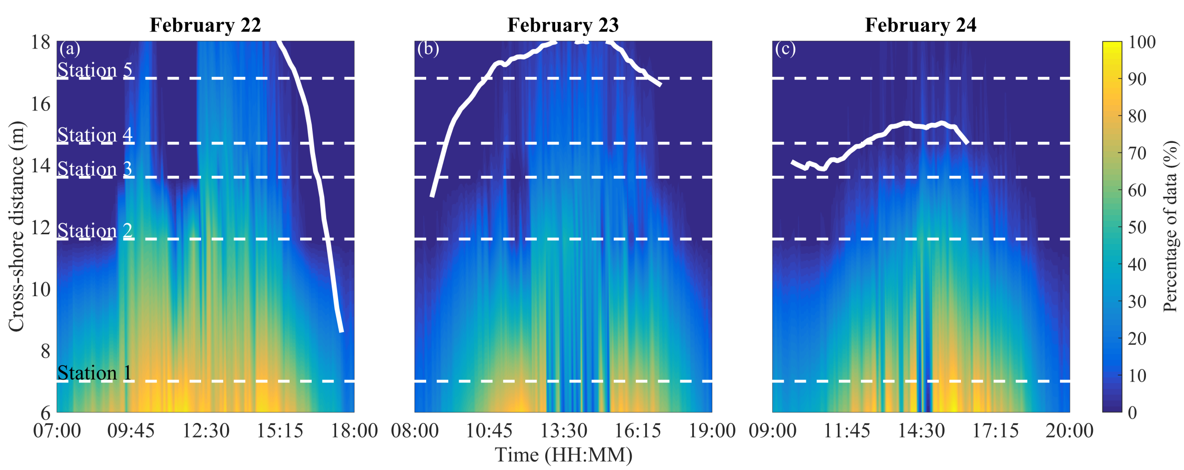

Figure 3.8. Five-minute time-average distribution of the percentage of velocity data retained after quality-controlled the ADPV velocity measurements. The white line denotes the runup (obtained by video imaging) and the horizontal dashed line the sensor station locations. Colors denote percentage of data retained for analysis.

3.2.5 Reconstruction of velocity time series

Two methods were used to reconstruct cross-shore velocity time series at each station: (1) the volume continuity method [referred to as VCME hereafter; Blenkinsopp et al., 2010b; Houser and Barrett, 2009b] and (2) a nonlinear shallow water equation solver [FUNWAVE; referred to as MVE (model velocity estimates) hereafter; Shi et al., 2012; Tehranirad et al., 2011]. The VCME was also needed to replace data removed from the ADPV at station 1 yielding a continuous inner surf zone forcing time series for the numerical model. The numerical model was then used to estimate cross-shore velocity time series for the other 4 stations.

ADPV measurements were transformed to depth-average velocities to allow combining VCME estimates with ADPV measurements, provide suitable boundary forcing to the numerical model, and allow direct comparison between measurements and estimates from both methods. *In situ* measurements were transformed assuming a logarithmic profile [Smith and Rogers, 2009; Wiberg and Smith, 1991] as

$$\bar{U} = u_n(z_s)\frac{ln(\frac{0.4h}{z_0})}{ln(\frac{z_s}{z_0})}, \tag{3.1}$$

where $\bar{U}$ is the depth-averaged velocity, u_n is the near-bed cross-shore velocity component (here the ADVP measurements), z_0 is the roughness height (= $1/30\ k_s$), k_s (=$2.5d_{50}$) is the apparent bed roughness, and z_s is the elevation above bed with $z_s = 0$ at the bed (based on nominal elevations). This approach yielded a ratio that varies in proportion to the logarithm of h over the bed roughness. The ratio of near-bed velocity to depth-averaged flow velocity was approximately 0.83 - 0.87, similar to the ratios reported by Raubenheimer et al. [2004]. The error in considering this assumption is often acceptably small if the sediment grain size is small with respect to the flow depth [Wiberg and Smith, 1991]. However, this has been confirmed for the offshore zone. There are still uncertainties in the inner surf and swash zones.

FUNWAVE, a Boussinesq wave model, was used as a shock-capturing nonlinear shallow water equation solver by deactivating the Boussinesq terms [Lanckriet and Puleo, 2015]. The MVE was run in one-dimensional mode over the foreshore profile with a cross-shore grid spacing of 0.025 m. The offshore boundary condition (BC) at station 1 (Figure 3.9) consisted of the depth-averaged velocity and local water depth (recorded by the PT). Friction coefficients (c_f) varied spatially throughout the model domain estimated as [Swart et al., 1974]

$$c_f = 0.0025exp\left(\left[5.213\left(\frac{a}{k_s}\right)^{-0.194}\right]\right), \tag{3.2}$$

where a ($= T_p u_{x_{max}}/2\pi$) is the swash excursion length. MVE simulations provided water depth and depth-averaged cross-shore velocity time series without data gaps for each station.

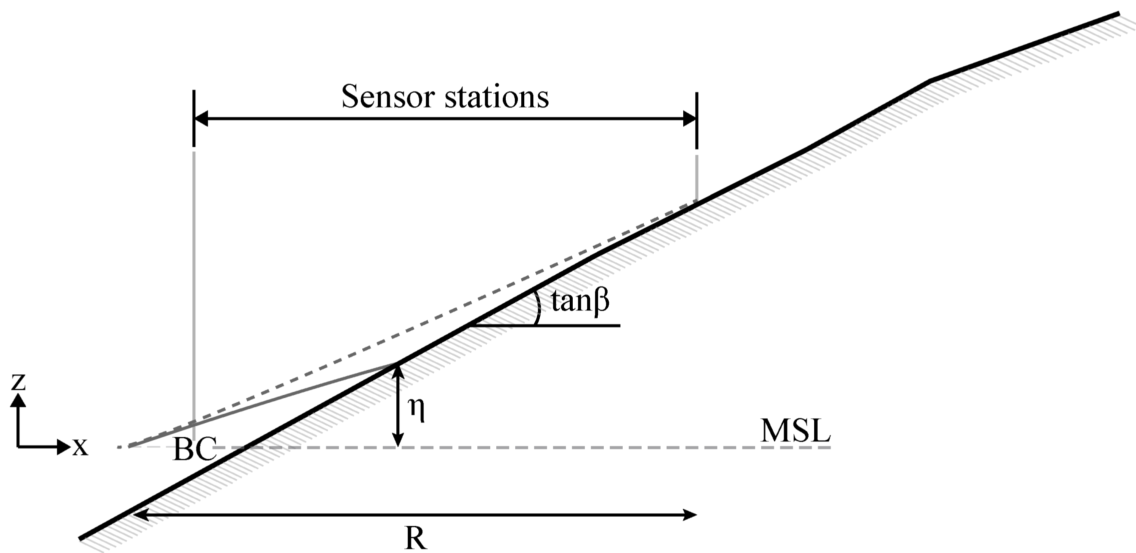

Figure 3.9. Definition sketch of numerical setup for the South Bethany Beach foreshore. BC is the location of the offshore boundary conditions, η is the free surface elevation, $tan\beta$ is the foreshore slope, and R is the runup excursion.

The depth-averaged velocity was estimated using the VCME technique by dividing cross-shore volume flux by local water depth. VCME depth-averaged velocity estimates were compared to ADPV measurements transformed to depth-averaged velocity using equation 3.1 for each station (Figure 3.10c). The average (standard deviation) of errors of 5-min root mean square cross-shore velocities between VCME estimates and ADPV measurements varied from 3% (19%) to 14% (38%) between stations with an overall root mean square error (RMSE) of 0.22 m s^{-1}. These errors are similar to those estimated using the same model but under different field conditions [Blenkinsopp et al., 2010b]. The VCME captures the variation of the water surface due to bore arrival and/or flow interactions, whereas the ADPV measurements only capture the near-bed flow (Figure 3.10c at station 5; t = 25 - 30 s). Additionally, differences were also apparent when the water depth at a certain location was such that the bed became rarely exposed (Figure 3.10c at station 5; t = 35 - 40 s), meaning that there is vertical shear that cannot be identified from the depth-average velocity estimates.

MVE estimates were compared against ADPV measurements (Figure 3.10b) to evaluate the numerical model performance. The mean (standard deviation) of errors of 5-min MVE water depth estimates relative to the observations varied from 2% (12%) to 8% (28%) between stations. Whereas, the mean (standard deviation) of 5-min root mean square cross-shore velocities between ADPV measurements and MVE estimates varied from 10% (31%) to 27% (52%) between stations with an overall RMSE of 0.44 m s^{-1}. These errors were similar to those obtained using a one-dimensional depth-averaged nonlinear shallow water equation model with quadratic friction [Raubenheimer, 2002]. As expected, MVE estimates for velocity were larger in magnitude than ADPV measurements due to quality-control procedures and data truncation at the early/final stages of swash events. The reconstructed cross-shore velocity time series, VCME and MVE, were used in the analysis of sediment transport and foreshore morphological change described in Subsection 3.4.4.

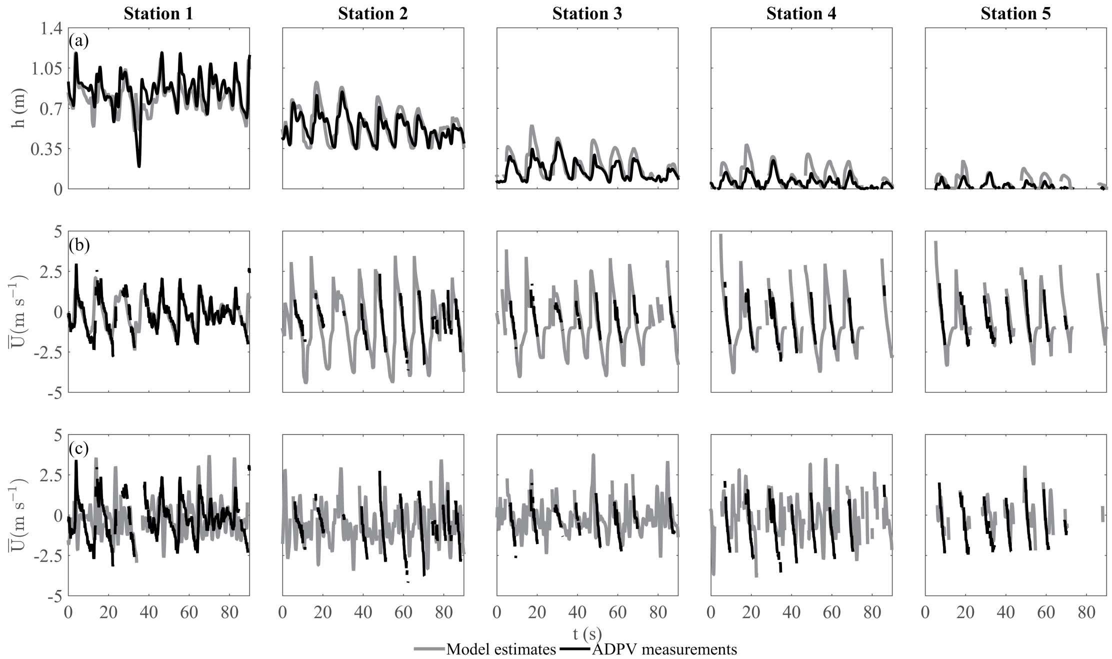

Figure 3.10. (a) Comparison of measurements of water depth (gray) and FUNWAVE (MVE) model result (black); (b) comparison of measurements of cross-shore velocity transformed from the ADPV (gray) and MVE model results (black); and (c) comparison of measurements of cross-shore velocity transformed from the ADPV (gray) and velocity estimate using volume continuity method (VCME) (black).

3.3 Hydrodynamic and Sediment Transport Parameters

The hydrodynamic and suspended sediment transport formulations used in this study are described in the following subsections. The parameters are used to quantify inner-surf and swash-zone processes in relation to observed foreshore elevation variability (Section 3.4).

Bed Shear Stress

The quadratic drag law was used to estimate the bed shear stress (equation 2.1).The quadratic drag law has been widely applied in inner-surf and swash-zone studies where velocities are collected at a single or multiple elevations above the bed [e.g., Puleo et al., 2012; Raubenheimer et al., 2004]. The embedded friction coefficient was estimated using the Swart et al. [1974] formula (equation 3.2). Friction coefficient estimates ranged from 0.01 to 0.02 and are commensurate with values from sandy beaches reported in many prior studies [e.g., Hughes et al., 1997; Inch et al., 2015; Puleo et al., 2012; Puleo and Holland, 2001; Raubenheimer et al., 2004] suggesting the use of Swart's formula is appropriate.

Alternatives for estimating bed shear stress rely on: 1) the von Karman-Prandtl relationship [e.g., Inch et al., 2015; Masselink and Russell, 2005; Puleo et al., 2014b, 2012; Raubenheimer et al., 2004] that requires a model skill cutoff to accept or reject such estimates; or 2) parameterizations relying on velocity fluctuations [e.g., Aagaard and Hughes, 2006; Nielsen, 2002] that carry estimation error through velocity decomposition in a non-stationary flow. These approaches have been applied in previous inner-surf and swash-zone studies. However, the energetic conditions encountered in the present study lead to difficulties in applying these methods. Thus, the quadratic drag law was used.

Suspended sediment transport rates

Suspended sediment concentration (SSC) measurements were used to estimate concentration profiles and suspended sediment transport rates. SSC from stations with a pair of OBS (stations 1, 2, 4) were extrapolated to sediment concentration profiles using a power-law approximation between sensors [Camenen and Larson, 2005] and a uniform profile below the lowest sensor with SSC equivalent to lowest OBS measurements [Puleo et al., 2014a]. Meanwhile, for stations with only one OBS or if only one OBS was submerged, the concentration was assumed constant from the OBS towards the bed. Neither near-bed velocity nor suspended sediment concentration profiles were extended to the free surface to avoid introducing additional unknown error into the estimates (see Discussion; Section 3.5.1).

Instantaneous depth-integrated suspended sediment transport rate (Q_i) was calculated as

$$Q_i = \int_{z_s=0}^{z_s=h_{OBS}} u_i(z_s) SSC(z_s) dz_s, \tag{3.3}$$

where h_{OBS} is the elevation of the highest submerged OBS, $SSC(z_s)$ is the sediment concentration profile, and dz_s is the difference in elevation.

3.4 Results

Raising and lowering of sensors relative to the bed occurred only during daylight due to the dangerous conditions and severe cold weather during the field study. Therefore, only data from daylight, comprised of one high tide per day were analyzed.

3.4.1 Spectral signature

A spectral analysis was performed with station 1 water depth measurements to calculate the relative energy levels over a tidal cycle. Data from the other stations were not used for spectral analysis due to data discontinuities. Spectra were computed using Welch's average periodiogram method, dividing the water depth measurements into 10-min segments with 50 % overlap, tapered using a Hamming window. The incident frequency peak in the inner surf zone is evident ($f > 0.05$ Hz; where f is frequency; Figure 3.11). The water depth spectrum for each day had dominant peaks at 10, 16, and 14 s, respectively. The reflective nature of the beach was confirmed by calculating the surf similarity parameter (ξ) [Guza and Inman, 1975]. Surf similarity parameters were less than 2.5 for each day, indicating that the inner-surf and swash-zone flows were dominated by incident-wave bores [Wright and Short, 1984]. Past field investigations have observed that reflective beaches are mostly swash-aligned (parallel to shore) and respond rapidly to changes in wave energy [e.g., Aagaard et al., 2012; Dail et al., 2000]. The high frequencies influence strongly the inner-surf and swash-zone dynamics and sediment suspension patterns. Interaction between collapsing bores and swash events tend to occur and increase as the incident-band frequency increases [Brocchini and Baldock, 2008; Hughes et al., 2014] thereby increasing the number of sediment suspension events.

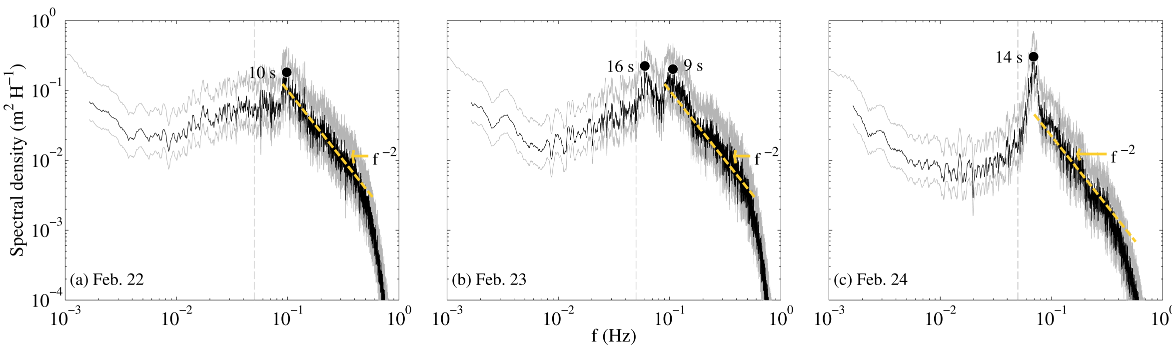

Figure 3.11. Water depth spectrum from PT data at station 1 for each day. Gray lines are the 95% - confidence bounds. Vertical dotted line identifies the division between the infragravity and incident frequencies (0.05 Hz; 20 s). Yellow dashed line shows an f^{-2} slope for reference.

3.4.2 Hydrodynamic parameters

Figure 3.12 shows a 65-s time-series excerpt of instantaneous measurements of hydrodynamic parameters at each station. Water depth measurements (Figure 3.12a) over time and space are often used to identify the initiation of flow cycles. In the inner surf zone these cycles begin with the bore arrival inducing a sudden onshore-directed flow. The bore arrival/collapse is identified by the occurrence of local maxima in the water depth (Figure 3.12a; t = 55 s). As the bore propagates into the swash zone it initiates a swash event that extends up the foreshore until the maximum uprush limit. Water depth decreases and swash flow thins as the flow propagates farther up the foreshore. Then, the flow reverses and offshore-directed flow initiates. The swash events are identified by consecutive occurrences of zero water depth and/or by a local minima in the water depth [i.e., Figure 3.12a.3 3.12a.5; t = 10 s; Blenkinsopp et al., 2011; Caceres and Alsina, 2012].

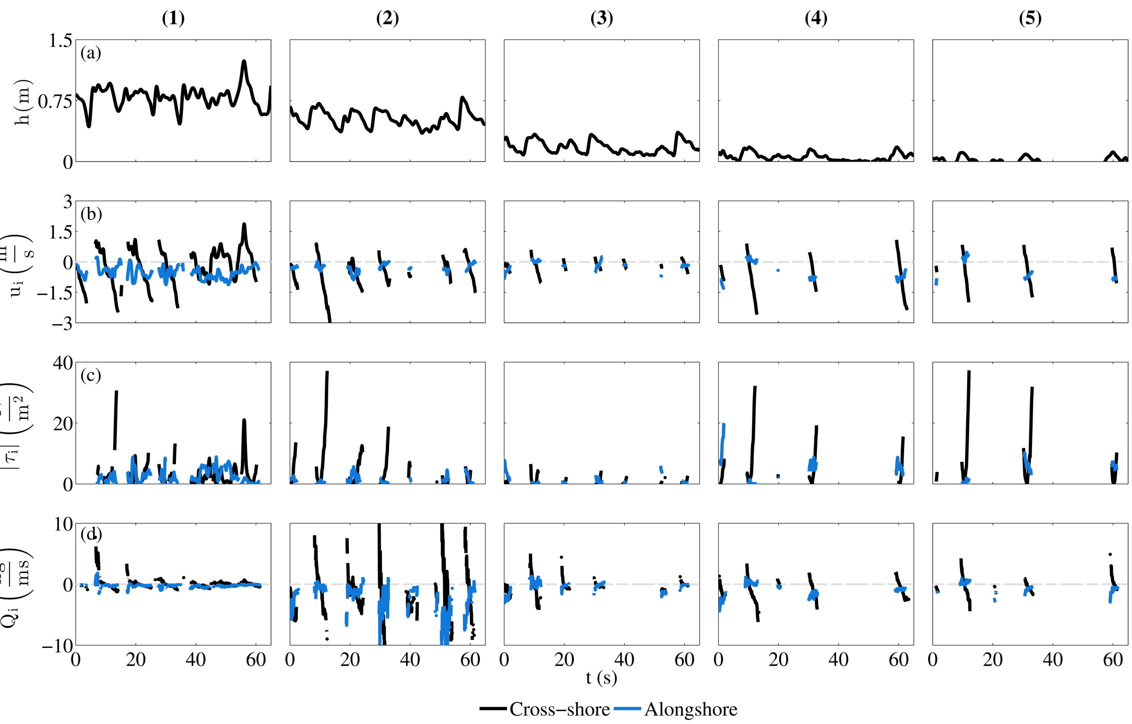

Figure 3.12. Time-series excerpt of inner-surf and swash-zone hydrodynamic and sediment transport for each station: (a) water depth; (b) cross-shore (black line; positive values indicate onshore-directed flow; negative values indicate offshore-directed flow) and alongshore (blue line) velocity; (c) cross-shore (black line) and alongshore (blue line) bed shear stress; and (d) cross-shore (black line) and alongshore (blue line) suspended sediment transport rate.

Cross-shore velocities were of longer duration during offshore-directed flows (Figure 3.12b negative values). Station 2 was mainly located in the transition between the inner surf and swash zone. However, velocities were intermittent due to the presence of bubbles (Figure 3.12b.2). Onshore-directed flow initiation was not measured due to this disturbance. The same problem occurred at the landward stations. Bores frequently collapsed at station 3 affecting the acoustic sensor measurements and reducing the duration of quality-controlled data. The swash-zone flows were strong, considering that the water depth was approximately an order of magnitude smaller compared to the stations in the inner surf zone.

Over the 3 days, the maximum onshore-directed (offshore-directed) velocity measured in the inner surf zone varied between 3.6 to 4.1 m s^{-1} (-3.5 to -4.3 m s^{-1}) and between 2.4 to 3.9 m s^{-1} (-3.15 to -3.6 m s^{-1}) in the swash zone. These velocity ranges were larger than maximum velocities measured previously on steep sandy foreshores [e.g., Conley and Griffin, 2004; Houser and Barrett, 2010; Puleo et al., 2000]. It was observed that maximum onshore-directed velocities were either similar or slightly larger than the maximum offshore-directed velocities as found previously [Conley and Griffin, 2004; Houser and Barrett, 2010; Shanehsazzadeh and Holmes, 2007]. Meanwhile, maximum alongshore velocity magnitudes reached similar values over the 3 days of 2.5 m s^{-1} to 4.2 m s^{-1} in the inner surf zone and 1.6 m s^{-1} to 2.7 m s^{-1} in the swash zone. These flows were mostly unidirectional (often northerly-directed) and occasionally exceeded cross-shore velocities [Austin et al., 2011; Puleo et al., 2014a]. Similarity between cross-shore and alongshore maximum velocity magnitudes, suggest that it is critical to incorporate alongshore velocities into the bed shear stress calculation even though there was negligible alongshore variability in morphology.

Maximum bed shear stresses were frequently observed at the end of the offshore-directed flow measured at all stations (Figure 3.12c). Except for station 3, bed shear stresses (i.e., Figure 3.12c) had a similar order of magnitude ($O(1)$-$O(10^1)$ N m^{-2}). The bed shear stresses increased between the inner surf zone just prior to bore collapse and the swash zone. The maximum cross-shore bed shear stress magnitude in the inner surf was 124 N m^{-2} and 130 N m^{-2} in the swash zone. Whereas, maximum alongshore bed shear stress magnitude in the inner surf zone was 103 N m^{-2} and 59 N m^{-2} in the swash zone. Cross-shore and alongshore bed shear stresses were similar. The mean of $|\tau_x|/|\tau_y|$ over the study period varied from station to station and over the experiment duration (Figure 3.13; mean $\pm$ standard deviation; $[\mu \pm \sigma]$). These ratios suggest that the cross-shore component was generally dominant. However, the large value of the standard deviation indicates that the alongshore component cannot be assumed negligible.

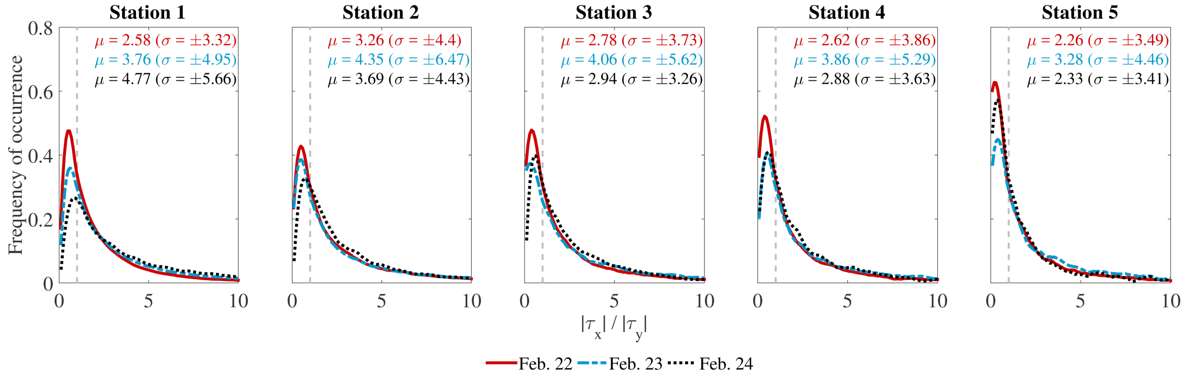

Figure 3.13. Ratios between the cross-shore and alongshore bed shear stress magnitudes at each station on Feb. 22 (red line), Feb. 23 (blue dashed line), and Feb. 24 (black dotted line). Vertical dashed line identifies the ratio equal to 1.

3.4.3 Suspended sediment transport parameters

Large quantities of suspended sediment were transported on the steep foreshore. Maximum suspended sediment concentrations (> 90 kg m^{-3}) occurred at the start of the flow cycle. Concentrations during offshore-directed flows did not exceed the concentration observed during the onshore-directed flows. However, the estimated cross-shore suspended sediment transport rates showed different behavior with offshore-directed rates occasionally larger and of longer duration than onshore-directed rates. This result is due partially to the intermittency of the velocity time series (Figure 3.12d). Alongshore suspended sediment transport rates were, for the most part, unidirectional and reached similar magnitudes as the cross-shore sediment transport rates. Larger alongshore sediment transport rates were observed at the seaward stations (Figure 3.12d.1 - 3.12d.3), where more turbulence was injected into the water column. For the landward stations, alongshore sediment transport rates were an order of magnitude smaller than the other stations (Figure 3.12d.4 - 3.12d.5).

Peak values of suspended sediment transport rates decreased during the course of the study. The temporal variation was mostly due to the decrease of the incident-band frequencies (Figure 3.12) and the steeping of the foreshore that reduced the occurrence of bore-swash and swash-swash interaction [Caceres and Alsina, 2012]. Maximum

Table 3.1. Maximum cross-shore sediment transport rates in the inner surf and swash zones.

	Maximum onshore-directed (offshore-directed) cross-shore sediment transport rate ($Q_x \equiv$ kg m^{-1} s^{-1})		
	Feb. 22	Feb. 23	Feb. 24
Inner surf	46 (-48)	96 (-58)	37 (-28)
Swash zone	33 (-44)	45 (-48)	44 (1-47)

cross-shore suspended sediment transport rates varied between onshore-directed and offshore-directed phases. The maximum onshore-directed and offshore-directed cross-shore sediment transport rates in the inner surf and swash zone are presented in Table 3.1. In the swash zone, the sediment transport rates were smaller; particularly, at station 5 where the rates were an order of magnitude smaller ($O(10^1$ m^{-1} s$^{-1}))$.

Inner-surf maximum alongshore suspended sediment transport rate magnitudes reached 39 kg m^{-1} s^{-1} on Feb. 22, 42 kg m^{-1} s^{-1} on Feb 23, and 20 kg m^{-1} s^{-1} on Feb. 24. Whereas, swash-zone maximum alongshore suspended sediment transport rate magnitudes were 34 kg m^{-1} s^{-1} on Feb. 22 and 33 kg m^{-1} s^{-1} for the last two days. The ratios of $|Q_x|/|Q_y|$ were influenced by larger cross-shore suspended sediment transport rates, suggesting that the cross-shore component was generally dominant (Figure 3.14; $\mu \pm \sigma$). The large standard deviation indicates that the alongshore component is not negligible even though the alongshore sediment transport gradients may be negligible relative to cross-shore suspended sediment transport gradients (Figure 3.6) and the associated morphological changes.

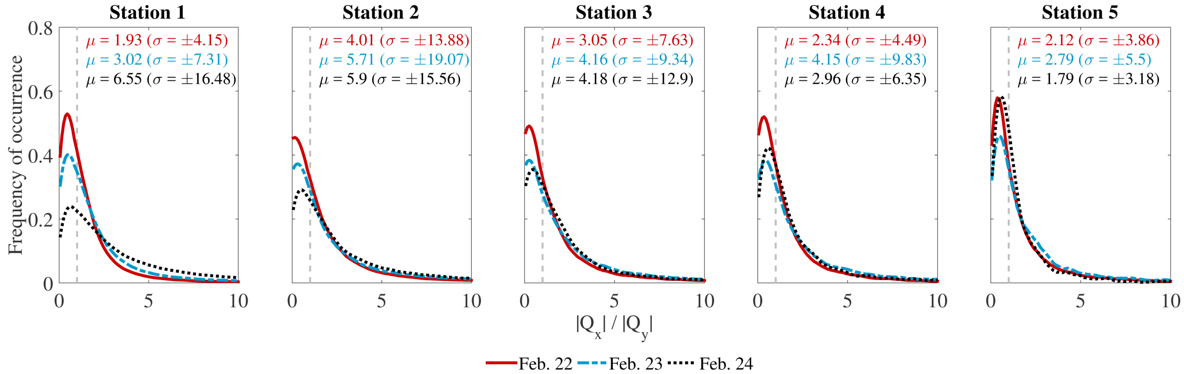

Figure 3.14. Ratios between the cross-shore and alongshore suspended sediment transport rate magnitudes at each station on Feb. 22 (red line), Feb. 23 (blue dashed line), and Feb. 24 (black dotted line). Vertical dashed line identifies the ratio equal to 1.

3.4.4 Spatial and temporal characteristics of instantaneous suspended sediment transport rates

Cross-shore and alongshore suspended sediment transport rates were binned to compare the distribution over each day and for each station (Figure 3.15). The majority of the cross-shore and alongshore sediment transport rate magnitudes were in the range of $Q_i < \pm\ 20$ kg m^{-1} s^{-1}. Larger rates were observed but not included in Figure 3.15 due to the low percentage of occurrence (< 2 %). An evident spatial and temporal variation is observed between the different stations. At all stations, small sediment transport rates had the larger maximum percentage of occurrence. The number of instantaneous rates (N-values) decreased with cross-shore distance and tide (day). This temporal variation was due to the percentage of time the measuring region of the sensor was inundated, the runup excursion length (water level), offshore wave conditions, and the steepening of the foreshore that affected the maximum excursion distance [Greenwood et al., 2004; Weir et al., 2006].

The distributions of the cross-shore sediment transport rates (Figure 3.15a) are negatively skewed (skewness < 0) and with heavy tails (kurtosis > 3) suggesting that offshore sediment transport dominated for the times the sensors collected reliable data. The alongshore sediment transport rate distributions were negatively skewed on Feb.

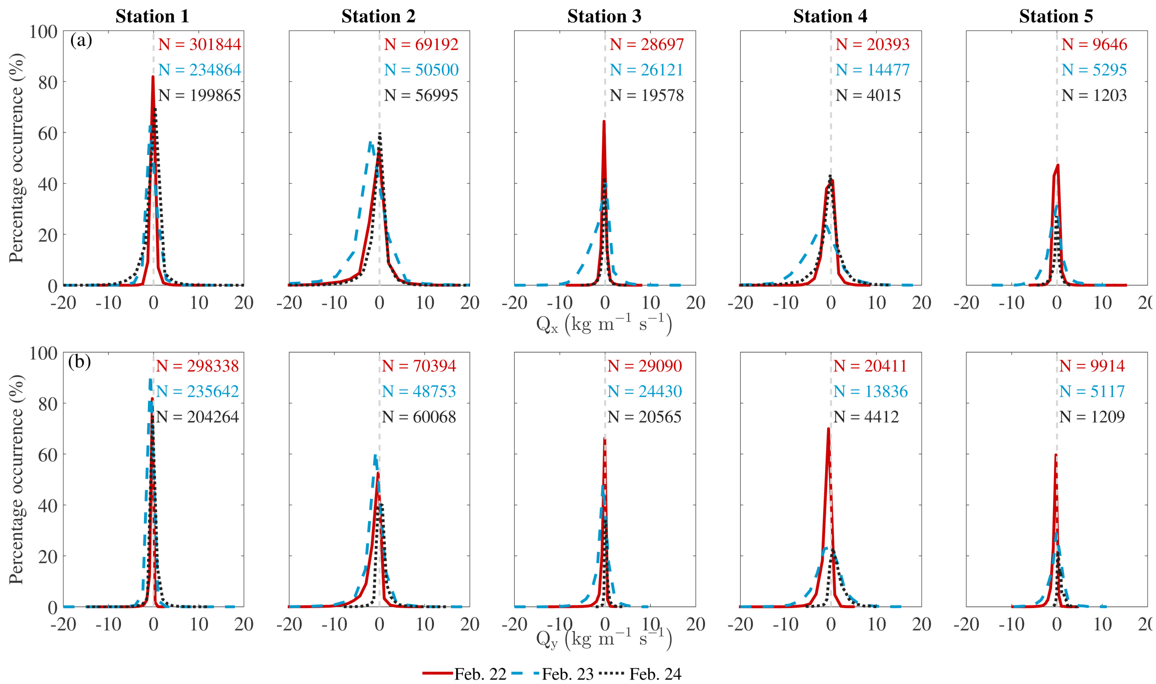

Figure 3.15. Distribution of the instantaneous (a) cross-shore and (b) alongshore suspended sediment transport rates at each station during Feb. 22 (red line), Feb. 23 (blue dashed line), and Feb. 24 (black dotted line).

22 and Feb. 23, and positively skewed on Feb. 24. However, the alongshore distributions skewness were minimum, close to zero.

All distributions followed a Student's t location-scale distribution (goodness of fit values significant at the 90 % on a *t-test* statistic) given by

$$P(Q_i) = \frac{\Gamma(\frac{\delta+1}{2})}{\varsigma\sqrt{\delta\pi}\Gamma(\frac{\delta+1}{2})}\left[\frac{\delta + (\frac{Q_i-\gamma}{\sigma})}{\delta}\right]^{-(\frac{\delta+1}{2})} \tag{3.4}$$

where γ is the location parameter (mean of the distribution), ς is the scale parameter (standard deviation of the distribution), δ is the shape parameter (degree of freedom) and Γ is the gamma function. The statistical parameters (γ, ς, and δ) were estimated using the maximum likelihood iterative method. The parametric probability distribution of the instantaneous cross-shore and alongshore suspended sediment transport rates matched the Student's t location scale distribution well (Figure 3.16; example for Feb. 22). The Student's t location-scale distribution is able to capture the tail of the distribution. However, the parametric distribution tends to underestimate the sediment transport rates ($Q_i < \pm$ 0.3 kg m^{-1} s^{-1}).

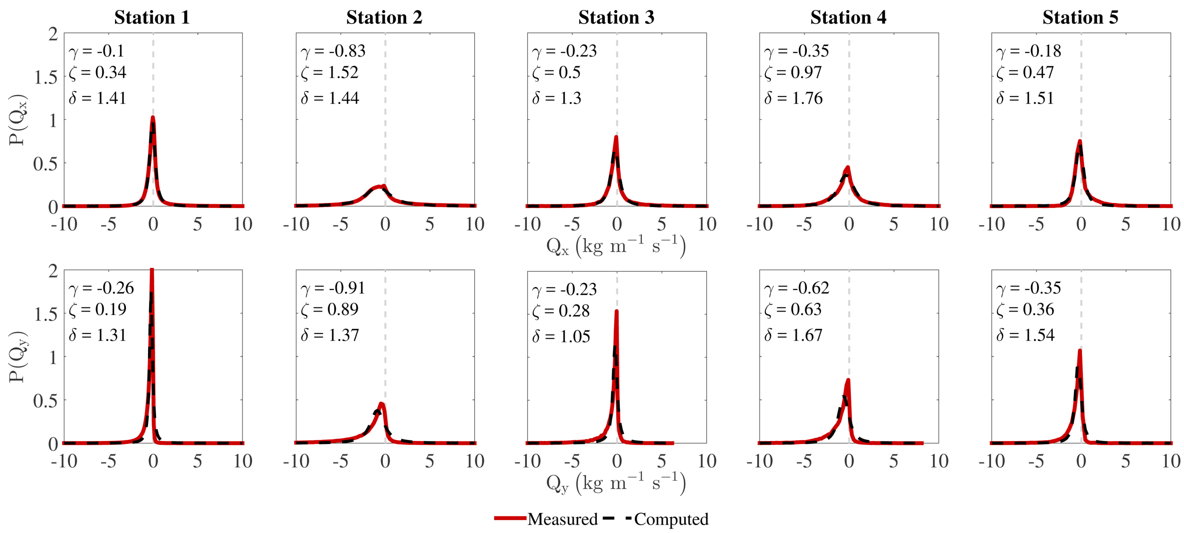

Figure 3.16. Probability distribution of the instantaneous (a) cross-shore and (b) alongshore suspended sediment transport rates at each station during Feb. 22 (red line) as well as the computed by the Student's t location-scale distribution (black line).

From the previous analysis, it is evident that there is a spatial and temporal variation in the measured instantaneous suspended sediment transport rates. However, the variation was based on measurements from sensors at fixed locations, whereas the inner surf and swash zone vary with tidal modulations. Therefore, the foreshore was divided into regions to define relative sensor location within the inner surf and swash zones as the tide level varies. The foreshore was parsed using the percentage of time the bed was inundated [Aagaard and Hughes, 2006; Blenkinsopp et al., 2011; Hughes and Moseley, 2007; Masselink et al., 2009; Masselink and Russell, 2005]. The percentage was calculated based on a 5-min average local mean water depth for each station (Figure 3.17). The maximum swash excursion (runup; Figure 3.17 thick white line) decreased over time with fewer swash events farther landward. By Feb. 24, stations 4 and 5 were inundated only 10 % of the time. The transition between inner surf zone and swash zone was determined on the basis that the inner surf zone is permanently submerged (95 - 100 %) and the swash zone is inundated intermittently (< 95 %). However, during the present study, the energetic conditions hindered the identification of the transition boundary. Therefore, the percentages selected varied by 5 to 10 % to those previously reported for inner surf (90 - 100 %), seaward swash zone (also known as lower and mid swash, 30 - 89 %), and landward swash (also known as upper swash; 1 - 29 %).

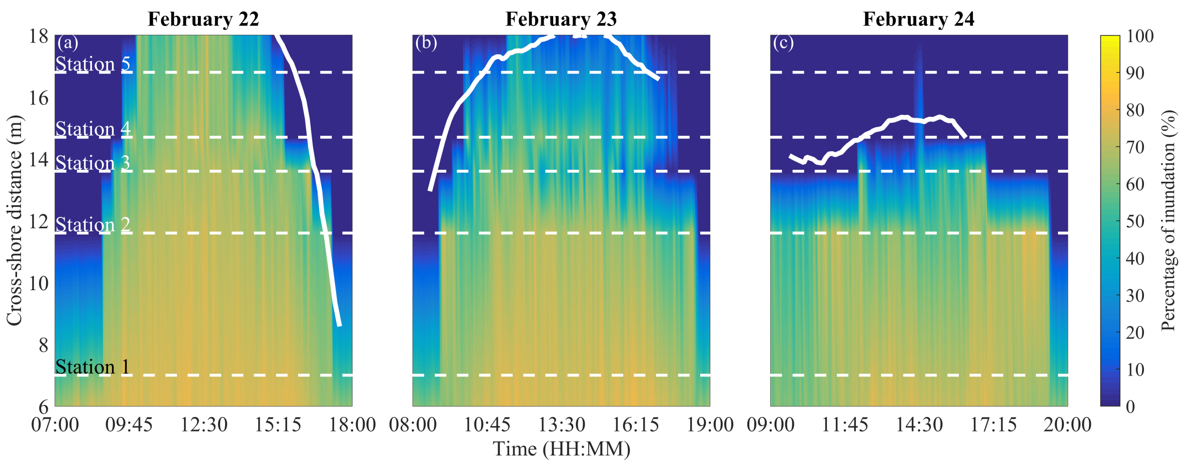

Figure 3.17. Five-minute time-average distribution of the percentage of time the bed was inundated throughout the stations as function of time (denoted by color scheme). The thick white line represents the runup limit.

The spatial variation of cross-shore and alongshore 5-min time-averaged instantaneous suspended sediment transport rates based on the percentage of inundation during each day is presented in Figure 3.18 as the mean and standard deviation suspended sediment transport rate (a-b) and skewness of the estimated mean sediment transport rates (c-d). The mean cross-shore suspended sediment transport rates (Figure 3.18a) varied between $\pm$ 0.5 kg m^{-1} s^{-1}. A noticeable spatial and temporal variation was observed in the standard deviation for the cross-shore component, particularly on Feb. 22, where there was a decrease between the landward swash zone to seaward swash zone and from seaward swash zone to the inner surf zone (Figure 3.18a). The standard deviation of the alongshore suspended sediment transport rates had a small spread

(Figure 3.18b). The mean alongshore suspended sediment transport rates (Figure 3.18b) ranged between 0 to -0.5 kg m^{-1} s^{-1}, except for the mean alongshore suspended sediment transport rates in the inner surf zone on Feb. 24 (0.1 kg m^{-1} s^{-1}). The largest mean and standard deviation cross-shore suspended sediment transport rates were estimated in the inner surf zone and seaward swash zone (Figure 18a). The mean cross-shore sediment transport rates ranged between -0.53 and 0.26 kg m^{-1} s^{-1} and were predominantly offshore. Meanwhile, the mean alongshore suspended sediment transport rates were relatively small (-0.03 to 0.12 kg m^{-1} s^{-1}) and predominantly northerly-directed (Figure 3.18b). The spatial and temporal variation of the cross-shore suspended sediment transport rate standard deviation was larger in the inner surf and seaward swash zone attributed to flow interactions ($\pm$ 0.7 kg m^{-1} s^{-1}). The spatial and temporal variation of the alongshore transport rate standard deviation was small and almost constant ($\pm$ 0.1 kg m^{-1} s^{-1}).

The skewness was quantified to assess the probability that an event was onshore-/offshore-directed (Figure 3.18c) or northerly-/southerly-directed (Figure 3.18d). Skewness was defined as

$$Skewness = \frac{\frac{1}{n}\sum_{j=1}^{n}(Q_{ij} - \bar{Q_i})^3}{\left(\sqrt{\frac{1}{n}\sum_{j=1}^{n}(Q_{ij} - \bar{Q_i})^2}\right)^3}, \tag{3.5}$$

where n is the number of data points and $(\bar{Q_i})$ is the suspended sediment transport rate mean. Positive skewness suggests that onshore-directed rates are more likely to occur for the cross-shore component and southerly-directed rates for the alongshore component, whereas negative skewness suggests offshore-directed rates for the cross-shore component and northerly-directed rates for the alongshore component.

The skewness for cross-shore suspended sediment transport rates varied spatially and temporally. On Feb. 22, all regions were positive (Figure 3.18c red circles), whereas on Feb. 23 and Feb. 24 only the seaward swash zone and inner surf were positive (Figure 3.18c blue squares and black crosses). Positive skewness suggests that the dimensionless cross-shore regions accreted [Houser and Barrett, 2009b]. This trend correlates well with the foreshore morphological change (dz) shown in Figure 3.5b - 3.5d (gray dashed lines). The larger accretion was observed at the seaward swash zone and inner surf zone regions ($0 < x < 14$ m) with minimum erosion at the landward swash zone ($14 < x < 20$ m). The alongshore suspended sediment transport rates were generally negatively skewed (northerly-directed; Figure 3.18d). The skewness was positive (southerly-directed; Figure 3.18d black crosses) only in the inner surf zone on Feb. 24.

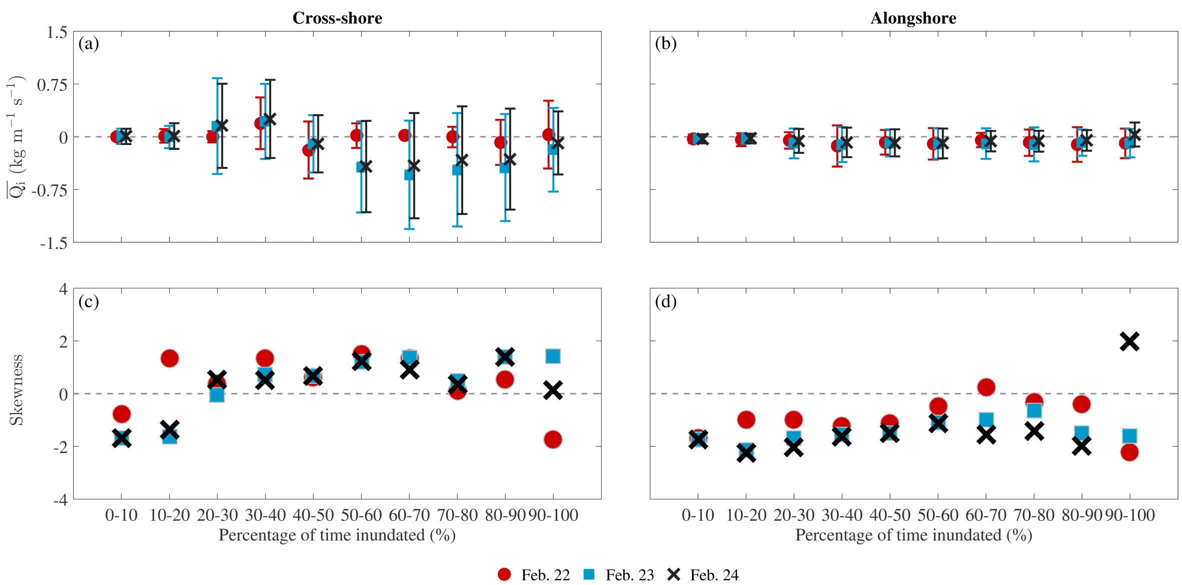

Figure 3.18. (a-b) Mean and standard deviation (error bar) of suspended sediment transport rates; and (c-d) skewness of mean suspended sediment transport rates as a function of percentage of time inundated for Feb. 22 (red circles), Feb. 23 (blue squares), and Feb. 24 (black crosses). Symbols are offset in panels (a-b) for visual clarity.

3.4.5 Suspended sediment transport gradients and associated morphological changes

Cross-shore suspended sediment transport rate gradients between each cross-shore station were estimated to quantify net sediment transport and the associated foreshore morphological change. No alongshore sediment transport gradients were considered because minimal alongshore foreshore morphological variability was measured (Figure 3.6). Cross-shore suspended sediment transport rate gradients (Figure 3.18c) were estimated using the following three methods: (1) ADPV velocity and OBS concentration measurements, (2) VCME velocity estimates and OBS measurements, and (3) MVE model results and OBS measurements. Net sediment transport was quantified from cross-shore suspended sediment transport rate gradients summed over 5-minute intervals. Figure 3.19b shows, that for Feb. 22 the direction and magnitude of the suspended sediment transport rate gradients varied between stations/regions. Predicted deposition occurred in the regions where dQ_x/dx was less than zero and erosion was predicted when dQ_x/dx was greater than zero. The estimated gradients from method (1) in the region $7 \leq x \leq 11$ m (Figure 3.19b□), show the corresponding pattern of the cross-shore sediment transport responsible for the foreshore profile change measured from morning to afternoon low tide (Figure 3.19a). The good agreement with the foreshore profile change is partially attributed to less velocity time-series intermittency for stations 1 and 2, as discussed earlier. Meanwhile, the estimated gradients in the other regions indicate erosion, being opposite to the foreshore profile difference measured. This discrepancy with measured profile change was likely due to a larger percentage of data removal from quality control during onshore-directed flows. Therefore, the averages were weighted more by offshore-directed flows. Methods (2) and (3) show a qualitative agreement with method (1) in the regions $7 \leq x \leq 11.5$ m, and $15 \leq x \leq 17$ m but with small magnitudes (Figure 3.19● and Figure 3.19⧫). Methods (2) and (3) have a qualitative agreement in terms of sediment transport direction with the foreshore profile change in the regions $7 \leq x \leq 11.5$ m and $13.5 \leq x \leq 15$ m. Differences in magnitudes and in some cases signs were observed between the 3 methods in the regions $11.5 \leq x \leq 13.5$ m and $13.5 \leq x \leq 15$ m. However, the magnitudes in all 3 methods were overestimated. Similar results were observed during Feb. 23 and Feb. 24 (not shown).

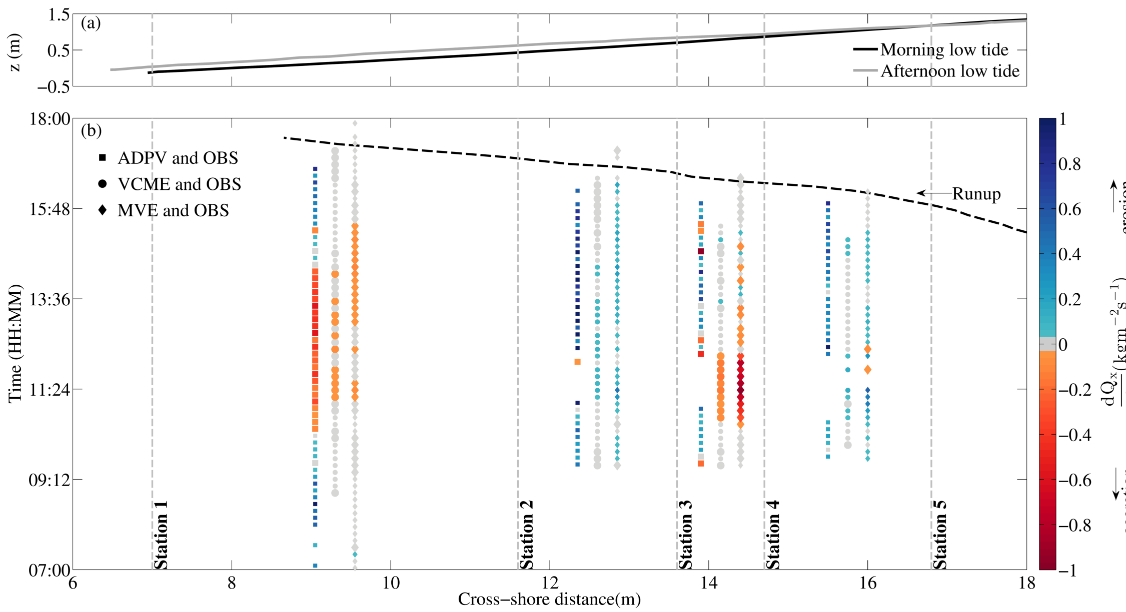

Figure 3.19. (a) Cross-shore foreshore profiles before and after high tide on Feb. 22, 2014; and (b) 5-minutes time-averaged sediment transport flux gradients estimated with: (■)ADPV and OBS measurements, (●) volume continuity method velocity estimates (VCME) and OBS measurements, and (♦) numerical model velocity estimate (MVE) and OBS measurements. In the bottom panel, the red color (negative values; large markers) indicates accretion, blue (positive values; small markers) indicates erosion, and gray indicates minimal to no change. Vertical dashed gray lines mark the cross-shore location of the stations and the black dashed curve denotes the runup (obtained by video imaging).

Most sediment transport models for the inner surf/swash zone are guided by the use of a Bagnold-type energetics model [Bagnold, 1966a]. The generic model assumes two transport modes: bed load and suspended load. But, because only suspended sediment transport was measured, a suspended sediment formulation was adopted to compare the cross-shore suspended sediment transport rates estimates with the model predictions. The immersed weight suspended sediment transport rate (I_s) is given by

$$I_s = \frac{0.5\epsilon_s(1-\epsilon_b)\tau_x|u_x|}{\left(\frac{w}{U_s}\right) - \left(\frac{|u_x|}{u_x}\right) tan\beta} \tag{3.6}$$

where w is the sediment fall velocity, U_s is the suspended sediment transport velocity, and ϵ is an efficiency factor (where the subscripts b and s indicate bed load and suspended load, respectively). U_s was assumed to be equal to u_x, therefore I_S is related to the velocity to the fourth power. The volumetric suspended sediment transport rate is related to the immersed weight transport rate as

$$q_x = \frac{I_s}{g(\rho_s - \rho)}\rho_s, \tag{3.7}$$

where g is the gravitational acceleration and ρ_s is the sediment density. The following three methods were used to predict sediment transport rates from the Bagnold approach: (4) ADPV velocity and Bagnold's formula, (5) VCME velocity estimates and Bagnold's formula, and (6) MVE model results and Bagnold's formula. Figure 3.20c shows, for Feb. 22, the suspended sediment transport rate gradients estimated with Bagnold's formula. The results from method (4) and (5) show slightly better agreement in terms of sediment transport direction (Figure 3.20b□ and 3.20b○) with the foreshore profile change (Figure 3.20a) in all regions. Method (6) predicts the wrong direction in all cross-shore regions (Figure 3.20b◇). The energetic-based suspended transport model predicted better the onshore-directed sediment transport in the first 3 regions than the methods based on OBS measurements, correlating qualitatively well with foreshore profile change. Moreover, both methods using VCME velocity estimates show the best qualitative agreement with the foreshore profile change, suggesting that VCME was able to estimate the onshore-directed flows. However, the magnitudes for all methods were overestimated. A similar pattern was observed for the other 2 days (not shown).

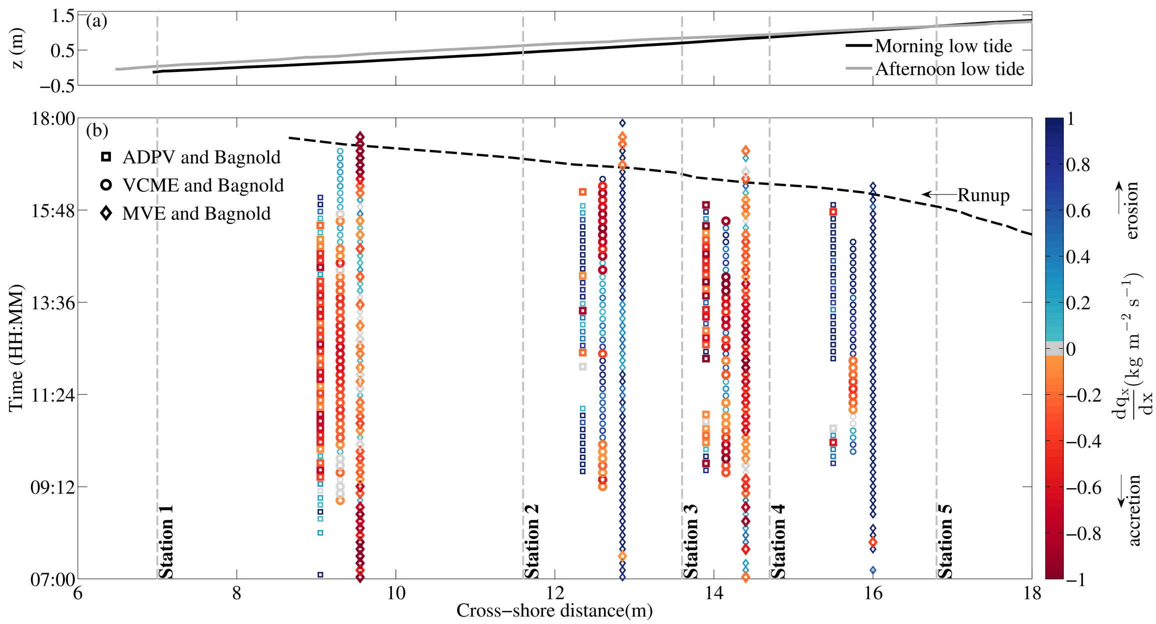

Figure 3.20. (a) Cross-shore foreshore profiles before and after high tide on Feb. 22, 2014; and (b) 5-minutes time-averaged sediment transport flux gradients estimated with: (□) ADPV measurements and Bagnold's formula, (○) volume continuity method velocity estimates (VCME) and Bagnold's formula, and (◇) numerical model velocity estimate (MVE) and Bagnold's formula. In the bottom panel, the red color (negative values; large markers) indicates accretion, blue (positive values; small markers) indicates erosion, and gray indicates minimal to no change. Vertical dashed gray lines mark the cross-shore location of the stations and the black dashed curve denotes the runup (obtained by video imaging).

The sum of the estimated and predicted cross-shore suspended sediment transport rate gradients (Figure 3.21c) were compared to the net cross-shore suspended sediment transport rate gradients (Figure 3.21b) to quantify the net change over a tidal cycle. The net sediment transport rate gradients were calculated through the sediment continuity equation as

$$\frac{dz}{dt} = -\frac{1}{\rho_s \alpha}\frac{dQ_x}{dx} \tag{3.8}$$

where dt is the difference in time between the profile measured before and after high tide ($\approx$ 12 hrs), α is the solidity (= 0.65), and dx is the cross-shore distance between stations. Equation 3.8 assumes no alongshore gradient contribution (discussed earlier).

The total net change between regions, using the sediment continuity equation (Figure 3.21b), indicates accretion across the foreshore with a net sediment transport rate between -0.2 to -0.01 kg m^{-2} s^{-1} on Feb. 22, between -0.075 to -0.01 kg m^{-2} s^{-1} on Feb. 22, and between -0.02 to 0.01 kg m^{-2} s^{-1} on Feb. 24.

The net suspended sediment transport rate gradients considering OBS measurements and Bagnold's formula (Figure 3.21c) were more than one order of magnitude larger than the total net change from the sediment continuity equation over the 3 days. The closest agreement with the sediment continuity equation for each region and over each day was from the suspended sediment transport rate gradients using VCME estimates and OBS measurements (Figure 3.21c●). The values ranged between -13 to 23 kg m^{-2} s^{-1}. Whereas, the worst agreement with the sediment continuity equation results was observed on Feb. 22 and Feb. 23 from suspended sediment transport rate gradients using Bagnold's formula and the ADVP (Figure 3.21c□) measurements and MVE estimates (Figure 3.21c◊). The values ranged between -170 to 188 kg m^{-2} s^{-1} for suspended sediment transport gradients estimated. But, overall, the six methods used to estimate and predict cross-shore suspended sediment transport rate gradients (Figure 3.21c) overestimate severely the total net change from the sediment continuity method (Figure 3.21b) by often two orders of magnitude.

3.5 Discussion

3.5.1 Inner-surf and swash-zone dynamics on a steep foreshore

The offshore wave conditions and steep foreshore in this study increased the effect of flow interactions, causing rapid changes in flow velocity, entraining a high concentration of air bubbles, and generating turbulence which lead to localized suspension and advection of sediment, consistent with previous findings [Blenkinsopp et al., 2011; Masselink et al., 2009]. Sediment transport rate estimates suggest sediment advected

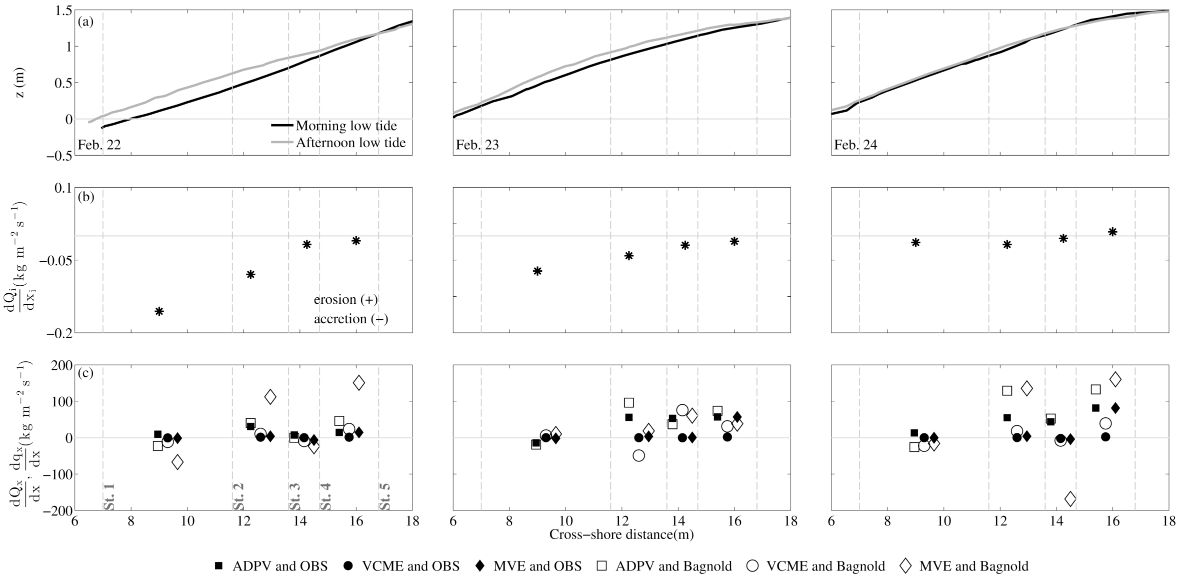

Figure 3.21. (a) Cross-shore foreshore profiles before and after high tide; (b) spatial gradient ($dQ_i dx$) estimated from dz/dt of the sediment continuity equation (equation 3.8); and (c) net cross-shore sediment transport rate gradients between stations estimated with: (■)ADPV and OBS measurements, (•) volume continuity method velocity estimates (VCME) and OBS measurements, (♦) numerical model velocity estimate (MVE) and OBS measurements, (□) ADPV measurements and Bagnold's formula, (○) volume continuity method velocity estimates (VCME) and Bagnold's formula, and (◊)numerical model velocity estimate (MVE) and Bagnold's formula. Vertical dashed gray lines mark the cross-shore location of the stations and the horizontal gray line identifies the value equal to zero.

from the point of bore collapse was deposited landward and dominated by the cross-shore component. Maximum cross-shore velocity magnitudes in the inner surf and swash zones exceeded 3.5 m s^{-1} and were commensurate with those reported previously for steep/reflective foreshores [Conley and Griffin, 2004; Houser and Barrett, 2010; Shanehsazzadeh and Holmes, 2007]. Maximum bed shear stress (exceeding 100 N m^{-1}) and suspended sediment concentrations (exceeding 200 kg m^{-3}) were found during the largest cross-shore velocities. Maximum cross-shore bed shear stress magnitudes were similar to previous estimates on a moderately sloped foreshore [Miles et al., 2006] under more energetic conditions and larger grain size. Cross-shore bed shear stress estimates exceeded, by approximately twice, those reported previously for sandy beaches under different foreshore slopes (mostly low gradient slopes) and hydrodynamic forcing conditions [e.g., Austin et al., 2011; Inch et al., 2015; Masselink and Russell, 2005; Puleo et al., 2014a, 2012]. Meanwhile, suspended sediment concentrations were consistent with those from other steep beaches [e.g., Masselink and Russell, 2006; Miles et al., 2006; Puleo, 2009; Puleo et al., 2003a, 2000]. Offshore-directed flows tended to have longer duration than onshore-directed flows, but this observation is sometimes biased owing to ADPV quality control. From the "viable" velocity measurements absolute differences between maximum onshore- and offshore-directed velocities were often < 0.1 m s^{-1}, indicating that the accretion may largely depend on sediment advection.

Alongshore components of velocity and hence sediment transport within the inner surf and swash zones were not negligible even with minimal alongshore gradients in morphology (Figure 3.6). Alongshore-directed hydrodynamic and sediment transport parameters were of similar magnitude to their cross-shore-directed counterparts in the inner surf zone, but smaller in the swash zone. Thus, the exclusion of alongshore-directed bed shear stress in cross-shore sediment transport formulations will underpredict the sediment transport rate and may lead to poor model skill. *In situ* measurements showed that when cross-shore flows decelerate, alongshore flows accelerate suggesting that sediment is maintained in suspension for a longer duration than a cross-shore only model would predict.

The majority (98 %) of the estimated cross-shore and alongshore suspended sediment transport rates in the inner surf and swash zone were in the range $\pm$ 20 kg m^{-1} s^{-1}, comparable to those reported previously. [e.g., Caceres and Alsina, 2012; Masselink and Russell, 2005; Puleo, 2009; Puleo et al., 2015, 2014a]. The negatively skewed distributions of the instantaneous cross-shore and alongshore suspended sediment transport rates (Figure 3.15) suggest that erosion was dominant. However, 0.23 m to 0.10 m of accretion was actually observed from Feb. 22 to Feb. 24, respectively.

The rapid vertical growth of the foreshore occurred during high tide and mostly due to the runup excursion length (water level) that overtopped the berm, transporting suspended sediment farther up the foreshore. However, the sediment transport rate estimates are contrary to the observed foreshore morphological change alluding to the difficulty of quantifying sediment transport rates even from *in situ* sensors. Issues with ADPVs and OBSs, being incapable of measuring the total flow duration of inner-surf and swash-zone dynamics can lead to compounding errors in the sediment transport estimates (Table 3.2). The combination of existing methodologies, such as remote sensing techniques (LIDAR or video imaging), non-intrusive sensors (ultrasonic distance meters), or larger arrays of collocated sensors may help reduce these errors in future datasets.

The OBS deployed were unable to resolve the vertical profile. It has been reported that extending suspended sediment transport rates to the free surface can enhance the suspended sediment transport rates, particularly during the initial onshore-directed flow phase due to increased water depths [Puleo et al., 2015]. There are a variety of options to extend the velocity and/or suspended sediment concentration profile to the free surface: (a) assume vertical uniformity of velocity and concentration above the highest submerged OBS, (b) assume a constant suspended concentration from the highest submerged OBS to the free surface, (c) linearly extrapolate the suspended concentration from the highest submerged OBS to zero at the free surface, (d) fit a concentration profile to some theoretical formulation and extend it to the free surface elevation, among others. As an example, suspended sediment transport rates were estimated again assuming a constant suspended sediment concentration from the highest submerged OBS to the free surface elevation. The suspended sediment transport rates increased by 160 to 200 % and surely overestimate the true sediment transport rate based on comparisons to bathymetric change. Extrapolating the concentration profiles introduced additional unknown error to the estimates and enhanced the importance of offshore-directed suspended sediment transport (erosive dominance). The

Table 3.2. Maximum cross-shore sediment transport rates in the inner surf and swash zones.

Field measurement instrumentation	Issue	Potential percent of data error (%)	Improved methodologies/ approaches
ADPV *flow velocity*	• Noisy signal due to aerated flows	• 7 - 9 % *	• Remote sensing (e.g., LIDAR)
	• Artificial truncation due to intermittent submersion or elevated sensors	• 9 - 11 % *	• Non-intrusive instrumentation (e.g., ultrasonic distance meters)
	• Limited vertical resolution (measured 30 mm of water column)	• 13 % *	• Collocated/stacked instrumentations
OBS *(suspended sediment concentration)*	• Calibration sensitivity due to air bubbles	• Data loss unknown but assumed small; error in response ∼ 25 % [Puleo et al., 2015]	• Collocated instrumentation
	• Calibration using sediment from the bed and assumend to be the material in suspension	• Unknown	•Sediment traps [Horn and Mason, 1994; Masselink et al., 2009], pump-bottle sampler [van Rijn, 2007], or multi-frequency acoustic concentration and velocity profiler (tested only in laboratory setup; [Chassagneux and Hurther, 2014]
	• Limited vertical resolution (single point measurement)	• ∼30%*	•Collocated/stacked instrumentation or use of fiber optical backscatter sensors (FOBS)
	• One sediment transport mode	• Up to a factor of 10 [Puleo et al., 2014b]	•Measure bed load [Aagaard and Hughes, 2006; Horn and Mason, 1994; Hughes et al., 2007; Masselink et al., 2005; Masselink and Russell, 2006; Puleo, 2009; Puleo et al., 2014a] and sheet flow [Lanckriet et al., 2014; Puleo et al., 2014b] using conductivity concentration profiler [CCP; Lanckriet and Puleo, 2013]

* Estimated from field study dataset

overall erosive tendency did not change, but larger discrepancies (nearly twice the vertical change) with equation 3.8 estimates were obtained. Puleo et al. [2015] used a vertical array of collocated measurements of flow velocity and suspended sediment concentration across a larger portion of the water column, compared to the present study, but were still unable to overcome the same data gap issues found here.

A spatial variation of the mean sediment transport rates was identified over the course of the study, where cross-shore distance was expressed as relative position based on the percentage of time the bed was inundated [Hughes and Moseley, 2007; Masselink and Russell, 2006].The largest mean cross-shore suspended sediment transport rates were estimated in the inner surf zone and seaward swash zone (Figure 3.18a). The mean cross-shore sediment transport rates ranged between -0.53 and 0.26 kg m^{-1} s^{-1} and were predominantly offshore. Meanwhile, the mean alongshore suspended sediment transport rates were relative small (-0.03 to -0.12 kg m^{-1} s^{-1}) and predominantly northerly-directed (Figure 3.18b). The spatial and temporal variation of the cross-shore suspended sediment transport rate standard deviation was larger in the inner surf and seaward swash zone attributed to flow interactions ($\pm$ 0.7 kg m^{-1} s^{-1}). Whereas, the spatial and temporal variation of the alongshore sediment transport rate standard deviation was small and almost constant ($\pm$ 0.1 kg m^{-1} s^{-1}). Blenkinsopp et al. [2011] observed a similar trend of increasing suspended sediment transport rate standard deviation with percentage of inundation during accretive conditions. The results indicate that a greater number of larger suspended sediment transport rates occur in the inner surf and seaward swash zone where the bed is inundated for longer periods of time. The skewness of the cross-shore suspended sediment transport rates is commensurate with foreshore accretion in the inner surf and seaward swash zone as measured. The instantaneous suspended sediment transport rates indicated that individual events can transport large quantities of sediment relative to the total change over a tidal cycle, whereas the mean of the suspended sediment transport rates suggested that the foreshore change might be caused by numerous small instantaneous sediment rates, noted in several recent studies [Austin and Masselink, 2006; Blenkinsopp et al., 2011; Masselink et al., 2009; Puleo et al., 2014b].

3.5.2 Morphological response

The analysis of morphological change focused only on cross-shore sediment transport rate gradients since the alongshore bathymetric variability quantified was small (Figure 3.6). Cross-shore suspended sediment transport rate gradients between each station were quantified using 6 different methods in an effort to account for possible inconsistencies with *in situ* measurements (Table 3.2). Cross-shore suspended sediment transport rate gradients estimated using Bagnolds formula (equation 3.6) confirmed that this model is not reliable on steep reflective beaches and may not be reliable in other scenarios [e.g., Butt et al., 2005; Hughes et al., 1997; Masselink and Hughes, 1998; Puleo et al., 2000]. The Bagnold-type model is based only on bed shear stress, flow velocity, and an auto suspension term, where each term has inherent assumptions. The flow velocity used to estimate bed shear stress is based on a quadratic drag law and the sediment transport prediction was obtained from varying acoustic Doppler sensor elevation relative to the bed. The auto suspension term is based on sediment from the bed and assumed to be the same material in suspension and efficiency factors are estimated using intermittent data. Previous studies have emphasized that the efficiency factors are not constant and may vary depending on location. A least square regression between *in situ* suspended sediment transport rate estimates and predictions from Bagnold's model was performed to estimate the values of k (=0.5ρ c_f ϵ_s (1-ϵ_b)), that incorporates the efficiency factors ϵ_b and ϵ_s. The values of k ranged between 0.55 to 10.5 (0.4 to 6.3) for onshore-directed (offshore-directed) flows and in similar magnitude to those reported previously [Hughes et al., 1997; Puleo et al., 2000]. Masselink and Hughes [1998] estimated values of k larger than 10.5 for onshore-directed flows and larger than 6.3 for offshore-directed flows. The large range of k values between stations shows the dependency of k on grain size, friction coefficient and field conditions [Hardisty, 1983; Hughes et al., 1997]. Hence, cross-shore suspended sediment transport rate gradients estimated using Bagnold's formula should consider spatially variable efficiency factors for onshore-directed and offshore-directed flows.

Five-minute time-averaged sediment transport rate gradients based on OBS measurements (Figure 3.19b) show qualitative agreement between the three different methods and with the foreshore profile change in the regions $7 \leq x \leq 11$ m (inner surf zone) and $13.5 \leq x \leq 15$ m (transition between seaward and landward swash zone). Meanwhile, the suspended sediment transport rate gradients using equation 3.7 and the VCME (Figure 3.20$circ$b) velocity time series show qualitative agreement with the foreshore profile change in the regions $7 \leq x \leq 11$ m, $11 \leq x \leq 13.5$ m (seaward swash zone), and $13.5 \leq x \leq 15$ m. Quantitative comparisons for all 6 methods were poor, overestimating severely the total net change from the sediment continuity method (Figure 3.21b) by often two orders of magnitude, indicating the difficulty in estimating or predicting sediment transport in the inner surf and swash zones. The poor agreement between the different methods may be ascribed to the potential error sources mentioned in table 3.2 and to:

1. no sediment advection was estimated as the energetics formulation assumes local suspension only. Onshore sediment transport may be affected by advection of entrained sediment, particularly on steep beaches where bores tend to collapse directly on the foreshore [Jackson et al., 2004; Masselink et al., 2010].

2. the nonlinear shallow water equation solver did not account for fluid infiltration/exfiltration and used a temporally constant and spatially varying friction coefficient (c_f).

3. Bagnolds energetics-based suspended sediment transport model assumes bed shear stress driven by a quadratic drag law in unidirectional flow and does not

consider turbulence generated by swash bores [Butt et al., 2005; Puleo et al., 2000], sediment advection [Alsina et al., 2009], flow acceleration or pressure gradient effects [Drake and Calantoni, 2001], and in/exfiltration effects [Turner and Masselink, 1998] that play an important role in sediment transport processes under reflective conditions on steep foreshores.

3.6 Conclusions

Concurrent measurements of flow dynamics and the sediment transport at 5 cross-shore locations were collected from the inner surf and swash zones of a steep-sloping sandy beach. Three high tides were monitored in an attempt to quantify the foreshore morphological change during accretive conditions. The results indicated that:

1. On steeper reflective beaches the effect of flow interactions increased the localized suspension and advection of sediment from the point of bore collapse at the inner surf zone or seaward swash zone and deposited landward, mostly by the cross-shore component.

2. Alongshore-directed hydrodynamic and sediment transport parameters can be of similar magnitude, compared to cross-shore components, in the inner surf and swash zones. Therefore, the alongshore component is a potential mechanism to enhance sediment transport and its exclusion from sediment transport predictions can lead to increased error.

3. A spatial and temporal variation of suspended sediment transport rates across the foreshore was identified and differences are attributed to the steepening of the foreshore, low energy wave climate, and the decrease of the incident frequency that affected the maximum excursion distance.

4. The cross-shore variation in the skewness of the suspended sediment transport rates was consistent with the instantaneous observations and foreshore morphological change measurements. A greater number of larger suspended sediment

transport rates occurred in the inner surf and seaward swash zones where most of the accretion occurred.

5. Cross-shore suspended sediment transport rate gradients estimated using Bagnolds formula confirmed that this approach is not reliable on steep reflective beaches. Sediment transport processes, under these conditions, are known to be driven by turbulence generated by swash bores, in/exfiltration effects, sediment advection, and flow acceleration or pressure gradient effects. Future experiments must consider all potential mechanisms that enhance sediment transport.

6. Temporal data gaps were a major limitation in quantifying sediment transport, particularly onshore-directed transport, due to issues with *in situ* instrumentation not being capable of measuring the total spatial and temporal variability of inner-surf and swash-zone dynamics. These gaps must be circumvented using remote sensing techniques, non-intrusive sensors, or larger arrays of collocated sensors.

Chapter 4

INNER-SURF AND SWASH-ZONE DYNAMICS ON A SEA-BREEZE DOMINATED BEACH

4.1 Introduction

The atmospheric circulation structure, at all scales, is directly related to convective processes that displace the air from high pressure zones to low pressure zones, and to advection that distributes the heat and moisture across the surface of the Earth [Abbs and Physick, 1992]. These processes generate wind and air circulation that transport the heat from the tropic to the high latitudes. Similar processes are observed in coastal regions, known as sea- and land-breeze systems. These systems are categorized as mesoscale meteorological phenomena and occur within kilometers and a time scale of seconds to hours [Sonu et al., 1973]. The intensity of these air flows varies depending on the temperature difference between the land and sea; larger temperature gradients induce more intense wind velocity [Federico et al., 2010]. Tropical and subtropical areas experience the strongest sea-breeze events due to the large temperature difference between land and sea (Figure 4.1).

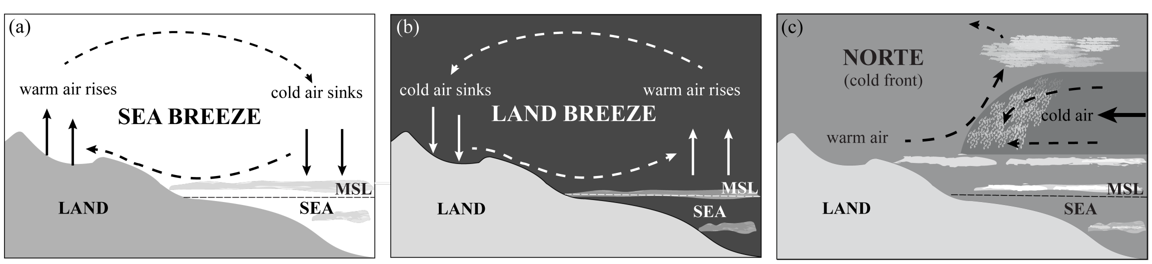

Figure 4.1. Schematic of (a) sea-breeze and (b) land-breeze circulation patterns in coastal zones and (c) El Norte.

Nearshore wave fields are strongly influenced by land- and sea-breeze conditions causing local wind waves to undergo changes in height, period and direction. Typically, sea breezes increase water levels and incident wave height and decrease the wave period. If sea-breeze conditions dominate the wave field, it may also affect the wave angle [Masselink and Pattiaratchi, 2001; Pattiaratchi et al., 1997; Sonu et al., 1973]. As temperatures cool, the sea breeze generated wave conditions subside with the opposition of land breezes [Masselink, 1998]. Intense wind events associated with synoptic scale events (referred to as small storm or high pressure systems) are also common in these areas. These events are characterized by a cold front passage and sustained intense winds. Cold fronts are noted by cold air advancing and displacing warmer air and generally move from west to east. Their duration can vary from one to a few days.

Prior studies have demonstrated that wave energy, wave-induced currents, and suspended sediment transport rate in the surf zone increase following the onset of the sea breezes [Masselink and Pattiaratchi, 2001; Sonu et al., 1973] inducing morphological change. Masselink [1998] showed that the sea-breeze-generated waves and currents induced continuous sediment resuspension, increasing the sediment transport rate by a factor of 100. This finding is similar to Kana and Ward [1980] who measured sediment transport rates during a storm. Thus, the impact on the coast during sea breeze conditions can be similar to a small storm [Masselink, 1998; Pattiaratchi et al., 1997]. The main difference is that sea breeze conditions occurred over a daily diurnal cycle, whereas storms occurred intermittently. During land-breeze, onshore sediment transport prevailed, inducing accretion whereas sea breeze conditions caused beach erosion [Masselink and Pattiaratchi, 2001] Their finding suggests that the sediment transport processes may have some balance on a daily basis, being analogous to the storm or seasonal cycle of beach morphological changes [Dean and Dalrymple, 2001; Komar, 1976]. Therefore, sea-breeze dominated beaches are continually adjusting morphologically due to changing hydrodynamic conditions. However, these local wind-forcing conditions are more important in microtidal environments with lower overall wave energy.

The aforementioned research efforts on the coastal dynamics on sea breeze dominated beaches focused on surf-zone-generated waves and current. However, to the author's knowledge, only one study has focused on swash-zone processes [Sonu et al., 1973]. Swash oscillations during the experiment, showed high-frequency attenuation controlled by tides, wave conditions and/or foreshore slope. However, there is a lack of data relating the small-scale inner-surf and swash-zone processes to different wind forcing conditions. To address this, a field study was conducted on a microtidal, low wave energy, sea-breeze dominated sandy beach to investigate the effects of local (land/sea breeze) and synoptic (storm) scale meteorological events on inner-surf and swash-zone dynamics. This paper presents near-bed hydrodynamic and sediment transport observations during different wind forcing conditions. Section 4.2 describes the field study that was conducted in Sisal, Yucatán, Mexico and the quality control procedures used on the data set. Section 4.3 describes the formulations used to quantify bed shear stress, turbulence dissipation rate and suspended sediment transport rate. Section 4.4 provides the results related to the temporal and spatial variability in the inner-surf and swash-zone hydrodynamic and sediment transport processes during different wind forcing conditions. Discussion and conclusions are given in Section 4.5 and Section 4.6, respectively.

4.2 Field Experiment

4.2.1 Study site and local climate

A field experiment (NCSAL; Nearshore Coastal Dynamics on a Sea-Breeze dominated micro-tidal beach) to study coastal hydrodynamic and sediment transport processes during different forcing conditions was conducted from April 1^{st} to April 11^{th}, 2014 at Sisal Beach, Sisal Yucatán, Mexico (Figure 4.2; 21° 09′ 56.20″ N, 90° 02′ 26.44″ W; 807320 m E, 2343344 m N). The northern Yucatn Peninsula (Figure 2), located between the Caribbean Sean and the Gulf of Mexico, has a 245 km wide and shallow continental shelf with a 1:1000 slope [Enriquez et al., 2010]. The peninsula has input to the coastal ocean from groundwater seeps and springs [Capurro and Reid, 1972]. The area has no river input to the coastal ocean.

Sisal Beach is a microtidal, low wave energy, sea-breeze dominated sandy beach with a semi-diurnal tide and a mean oceanic tidal range of 0.80 m. The beach is approximately 3.1 km long, faces northwest, and is exposed to both Gulf of Mexico swell and locally generated wind waves. The field site was located near the midpoint between Sisal Pier and the east jetty at Sisal port (Figure 4.2) and is characterized by a high-gradient profile mainly composed of medium sand with a median grain size (d_{50}) of 0.37 mm.

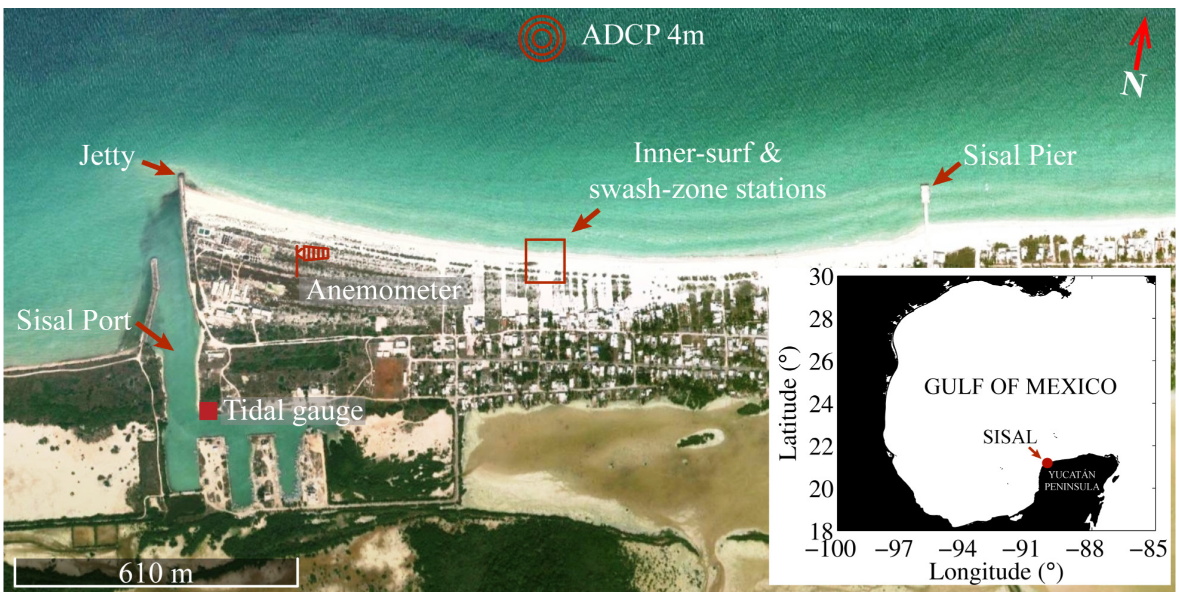

Figure 4.2. Location of Sisal, Yucatán, Mexico, showing the (●) study area, (□) field site, (◯) wave sensors deployed offshore (acoustic Doppler current profilers), (▲) tide gauge, and (+) anemometer.

The nearshore wave climate in Sisal depends primarily on the winds associated with local sea/land breezes induced by land-ocean temperature gradients and cold front passages (Nortes). Norte events are synoptic scale meteorological events with a short-duration that originate in the Southern United States and propagate across the Gulf of Mexico. The nearshore zone is typically subjected to daily land and sea breezes which generate small waves (< 0.5 m) with short wave periods (< 5.5 s) unless highly-energetic events occur. The intense winds induced by Nortes can generate large waves exceeding 1 m and peak periods are directly proportional to the wave energy.

Wind speed and direction (U_θ) were measured using a local weather station located 600 m west of the field site. The station consists of a 51 m tall mast outfitted with 3 ultrasonic anemometers. The anemometers were positioned at 3, 6, and 24 m above the ground level. Wind data from the highest anemometer were adjusted to the standard reference height of 10 m through the logarithmic law (Figure 4.3a) and are reported as U_{10}. Land-breeze events (Figure 4.3a) are related to winds blowing from a southeasterly/southerly direction and with wind speeds less than 10 m s^1. Sea breezes are characterized by winds blowing from an easterly/northeasterly direction with wind speeds between 3 m s^1 to 13.9 m s^1. A diurnal cycle was observed where the land breezes occurred from night to early morning and sea breezes between morning to late afternoon. Meanwhile, the Norte event (April 8 to April 9, 2014) was characterized by northerly/northwesterly winds with wind speeds exceeding 14 m s^1.

The changes in the wind climate were reflected in the wave climate (Figure 4.3b - d). Offshore wave measurements (Figure 4.3b-c) were collected during the study in approximately 4 m water depth using a bottom-mounted acoustic Doppler current profiler [Figure 4.2 Torres-Freyermuth et al., 2016]. A time series of significant wave height (H_s), wave period (T_p), wave direction (D_p), and mean sea level (MSL) was obtained through data post-processing using a surface tracking and U & V velocity (SUV) method. Water surface elevation was measured using an ultrasonic tidal gauge installed in the Sisal Port with elevations referenced to the mean sea level at the tidal gauge (Figure 4.2■).

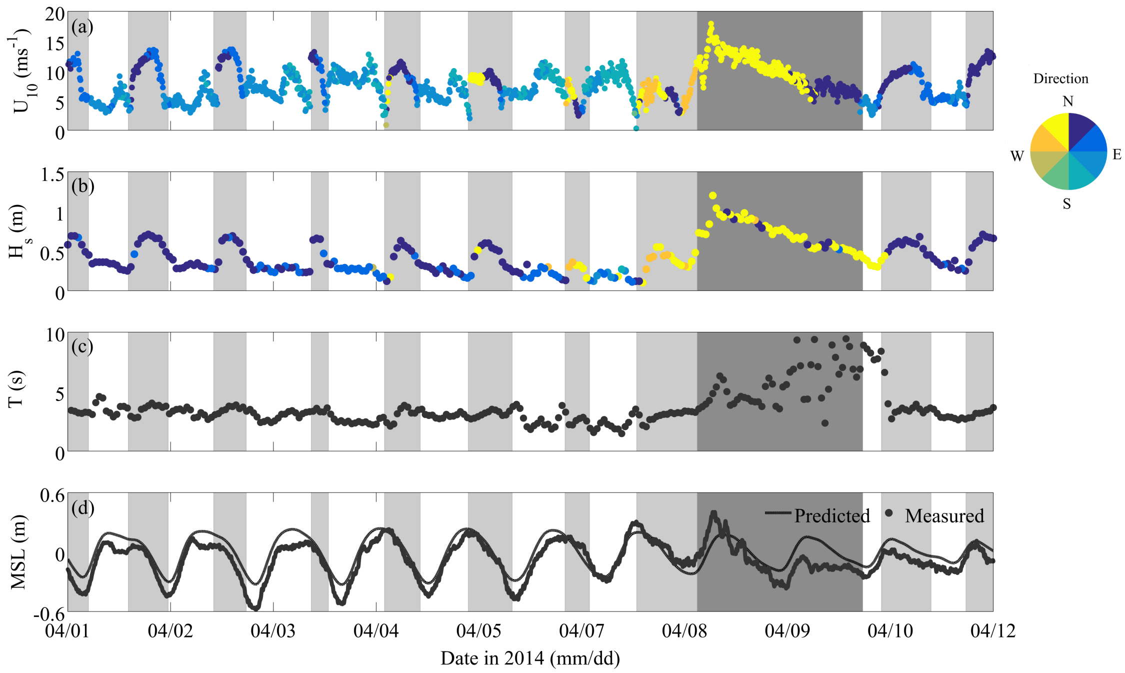

Figure 4.3. Time series of: (a) wind speed (U_{10}) and wind direction (U_θ) denoted by color scheme; (b) significant wave height (H_s) and wave direction (D) denoted by color scheme; (c) wave period (T); and (d) predicted (line) and measured (gray circles) mean sea level (MSL) during land breezes (white panels), sea breezes (light gray panels) and El Norte (dark gray panel).

During land breezes, small-amplitude waves of 0.1 - 0.3 m and 2.5 - 3.0 s prevailed (Figure 4.3b-c; white panels). The onset of the sea breezes induced an almost immediate change, increasing progressively the wave height to a maximum of 0.6 m and wave period of 4.0 s (Figure 4.3b-c; light gray panels). Waves during these forcing conditions were northeasterly/easterly directed. Meanwhile, during the onset of the Norte event, waves increased rapidly reaching a maximum significant wave height of 1.2 m and 6.2 s wave period (Figure 4.3b-c; dark gray panel). The measured mean sea level (Figure 4.3d) was in phase with the predicted tidal data ranging from -0.6 to 0.2 m, however the measurements deviated from the predictions by up to 0.15 m during land- and sea-breeze events. The measured mean sea level was 0.3 m higher than the predicted values during the beginning of the Norte and 0.2 m lower as the storm waves subsided (Figure 4.3d; dark gray panel).

4.2.2 Instrumentation setup

Numerous instruments were deployed during the field campaign to measure offshore, surf zone, inner-surf and swash-zone dynamics along three different transects (Figure 4.4a). However, this paper focuses on inner-surf and swash-zone measurements from the middle transect only (Figure 4.4b). For an overview of the instrumentation used in each zone refer to Torres-Freyermuth et al. [2016]. Three 12.5 m scaffold frame were erected within the inner surf and swash zones. Three instrument stations were established at different cross-shore locations with a cross-shore spacing of 4.9 m and 2.6 m between stations 1-2 and 2-3, respectively, (Figure 4.4b) to measure concurrently, fluid velocity, suspended sediment concentration and local water depth. Measurements during the field study were referenced to the local coordinate system established.

Each station contained a downward-looking Nortek Vectrino II acoustic Doppler profiling velocimeters (ADPV), a pair of Campbell Scientific optical backscatter sensor (OBS), and a pressure transducer (PT). In addition, the two landward stations (2 and 3) contained a Valeport electromagnetic current meter (EMCM). Each ADPV measured near-bed velocity profiles at 100 Hz over a total vertical range of 0.03 m at 0.001 m spacing . The ADPVs were initially positioned (deployed nominally at 0.03 m) such that the vertical profile intersected the bed. Sensors were adjusted occasionally in an effort to maintain a velocity profile that intersected the bed. The EMCMs measured cross-shore and alongshore velocities at 16 Hz at a single elevation above the bed (deployed nominally at 0.04 m). The PTs, located in the direct vicinity of the bed, were used to identify the local water depth accounting for sensor elevation relative to local bed level changes. PTs were sampled at 16 Hz. Suspended sediment concentrations were recorded at each station by two OBSs deployed at 0.035 and 0.085 m above the initial bed level. The OBSs were sampled at 16 Hz. *In situ* sensor data were recorded only when water level reached or exceeded their elevation. All sensors were surveys into the local coordinate system using a differential GPS system. The local elevation of each sensor above the bed was measured and adjusted vertically roughly every 1 and 2 hours but an exact schedule was not maintained.

A 3-m tower was erected landward of the scaffold frame. An Allied Vision Technologies (AVT) Stingray F125CP video camera with a 1290 x 960 pixel array was affixed to the top of the tower. Images were sampled at 7.5 Hz during daylight hours. Images were geo-referenced into the local coordinate system following the method of Holland and Holman [1997]. A cross-shore pixel transect just East of the scaffold frame was identified to quantify the runup excursion [Aagaard and Holm, 1989; Holland et al., 1995; Holland and Holman, 1993].A total of 50 timestack images were generated after sampling pixel intensities along a cross-shore transect 5 m east of the middle sensor frame. All sensors on the scaffold frames, the video camera, and weather station were cabled into the field trailer for power, control and data acquisition. Sensor data were recorded on individual laptop computers and were time synchronized to a common datum (Coordinated Universal Time; UTC) using a Garmin GPS antenna and Dimension4 and Tac32 software.

4.2.3 Cross-shore beach profiles

Cross-shore beach profiles were collected using a differential GPS system (Figure 4.5a). Profile elevations were obtained using a handheld antenna with the surveyor walking offshore, limiting the distance that could be surveyed. Offshore data points (from 80 to 170 m) were collected with a prism affixed to a 3 m tall pole and surveyed using a total station. Profile elevations were measured almost daily. Data were cast into a local coordinate system to simplify comprehension of distances. The cross-shore coordinate (x) increases landward and the vertical coordinate (z) increases upward. The beach is characterized by a steep foreshore ($tan\beta$ = 0.04 - 0.08) and two sand bars

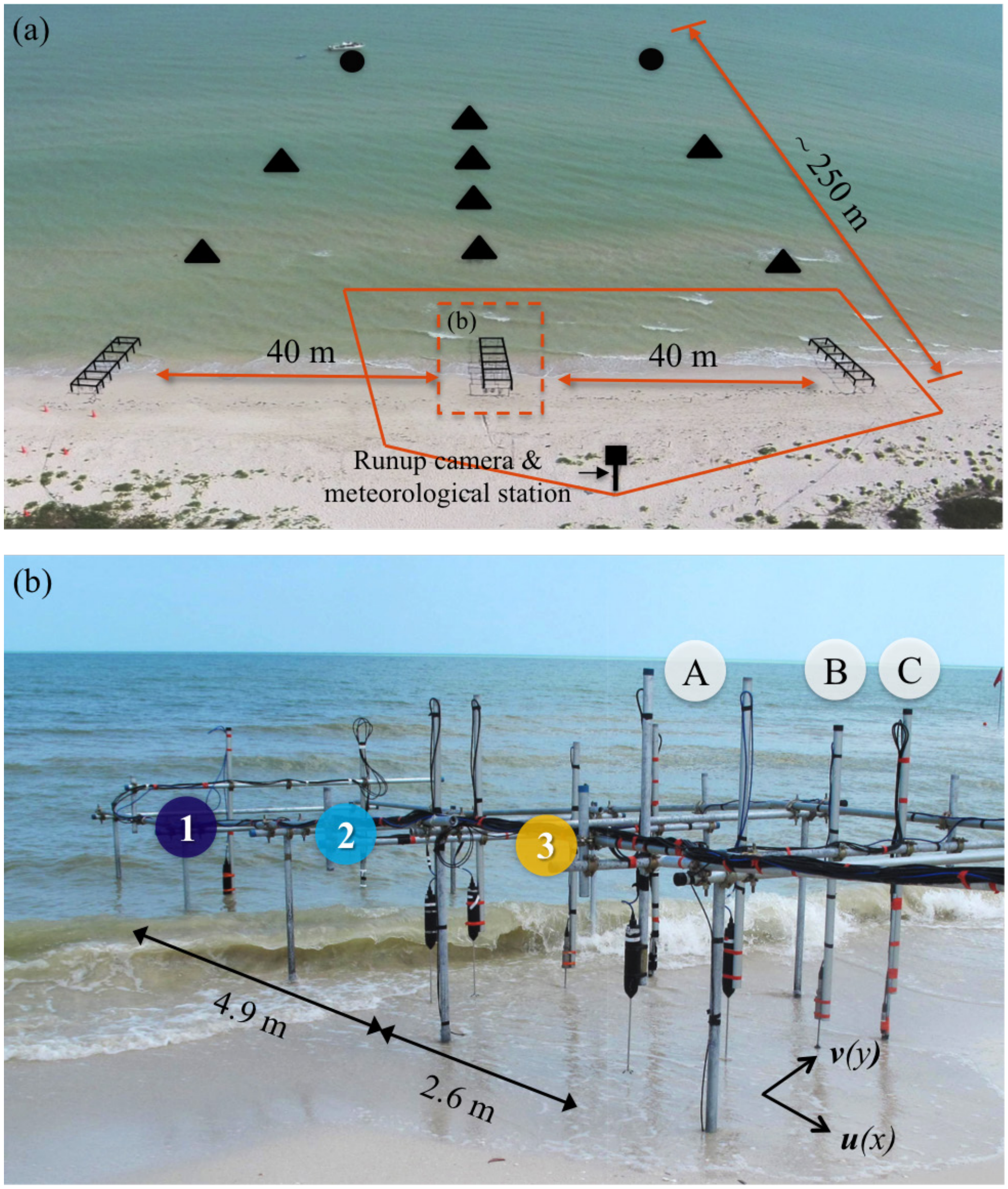

Figure 4.4. Images showing the: (a) location of the instruments used during the field experiment and (b) inner-surf swash-zone setup and stations. Sensors on the nearshore zone are (●) acoustic Doppler Aquadopp profiler; (▲) Vector three-dimensional current meter. On each inner-surf and swash-zone station: (A) acoustic Doppler profiler velocimeter (ADPV); (B) electromagnetic current meter (EMCM); (C) a pair of optical backscatter sensors (OBS) and a pressure transducer (PT). The enclosed area shows the field of view of the runup camera and the dashed square indicates the location relevant to this particular investigation.

located in 1.0 and 1.5 m water depth. Most of the pre- and post-storm morphological change was observed in the nearshore subaqueous regions and in the vicinity of the sand bars (x = -10 to -140 m). Energetic conditions during the Norte (H_s=1.2 m; T_p = 6.2 s) eroded the nearshore by 0.5 m (-80 to -100 m). The overall foreshore profile remained changed little in the vicinity of the sensors, within the inner surf and swash zones, with maximum elevation difference of dz =± 0.15 m (Figure 4.5b). The beach (x = -10 to -100 m) recovered slowly following storm wave subsidence

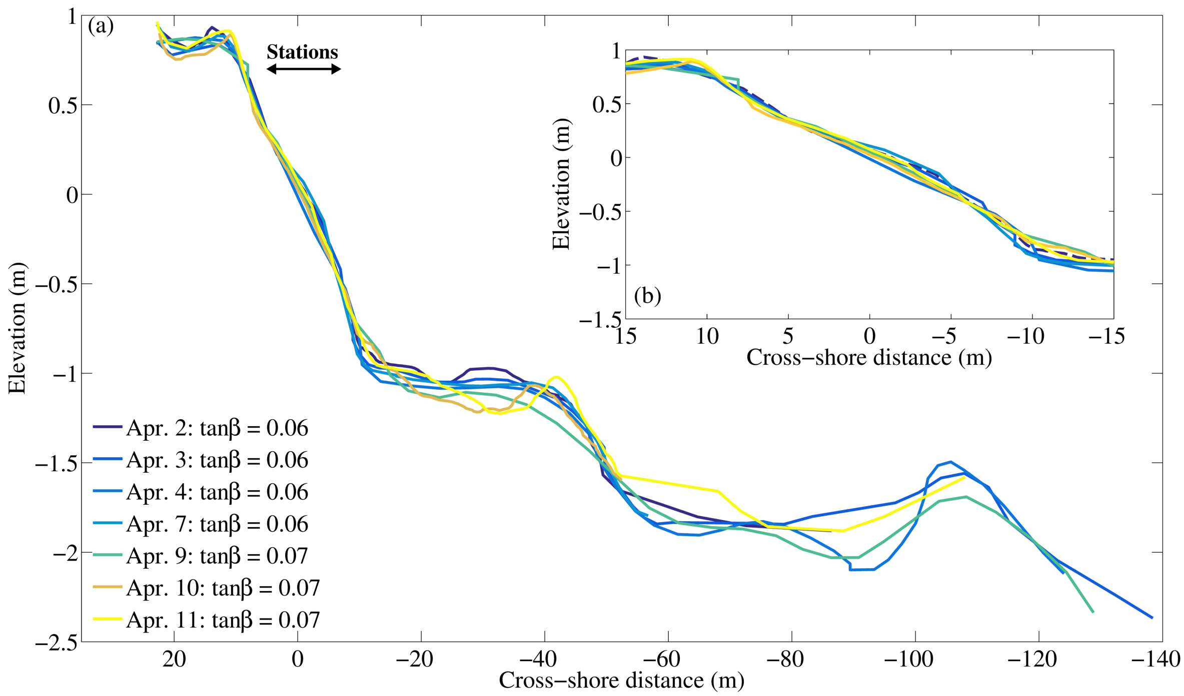

Figure 4.5. Cross-shore beach profiles measured during low tide along the the central transect with mean sea level at $z = 0$.

4.2.4 Data processing

Pressure transducer data were corrected for atmospheric pressure and converted to water depth using gains and offsets determined by a laboratory pressure calibration test. The water depths were corrected to account for sensor vertical adjustment. The OBSs were calibrated in a circulation chamber using the surface sediment samples collected adjacent to their deployment position. OBS data were removed from the record when the water depth, measured by the PT, was less than the sensor elevation. The EMCMs and ADPVs used in this study were calibrated by their manufacturers and are highly stable. Cross-shore and alongshore velocity time series collected with EMCM and ADPVs were combined to extend the velocity profiles from the bed to approximately 0.04 m above the bed. The extended velocity profiles allowed a better estimation of the flow dynamics and sediment transport processes. Raw ADPV time series records were quality controlled to remove unreliable data attributed to Doppler noise and signal discontinuity [intermittent submergence of instrumentation and/or ow laden with bubbles and sediment; Aagaard et al., 2006; Elgar et al., 2005; Lanckriet and Puleo, 2013; MacVicar et al., 2007; Puleo et al., 2012; Raubenheimer et al., 2004; Puleo et al., 2014a]. Internal data quality parameters such as beam amplitude, signal to noise ratio, and correlation score have been used to quality control acoustic Doppler data [Alsina et al., 2012; Caceres and Alsina, 2012; Hughes and Baldock, 2004; Inch et al., 2015; Lanckriet and Puleo, 2013; Puleo et al., 2012; Raubenheimer, 2002]. Here, near-bed velocity measurements were rejected when beam amplitudes were below -15 dB and the correlation score was below 80 %. A velocity difference between two subsequent measurements of greater than 0.5 m s^{-1} was used as a threshold value to remove spikes and spurious data from ADPV signals [Inch et al., 2015; Puleo et al., 2014a]. The greatest quantity of removed data occurred during uprush due to the high turbulence levels.

4.3 Hydrodynamic and Sediment Transport Formulations

The hydrodynamic and suspended sediment transport formulations used in this study are described in the following subsections. The parameters were used to quantify inner-surf and swash-zone processes in relation to forcing conditions (Section 4.4).

4.3.1 Turbulence

Different methods exist to calculate turbulence dissipation using field measurements, most of them performed in the surf zone, such as Kolmogorov hypothesis using frequency spectrum [Veron and Melville, 1999], wavenumber spectrum [e.g., Feddersen et al., 2007; Trowbridge and Elgar, 2001] or the structure function [e.g., Mohrholz et al., 2008; Whipple and Luettich Jr, 2009; Wiles et al., 2006]. From these three methods, the structure function is the most feasible to investigate the spatial and temporal evolution of the dissipation rate.

Near-bed turbulence dissipation rates were quantied using the structure function method described by Wiles et al. [2006] (equation 2.7). The vertical velocity component (w) was used because it has a lower noise floor compared to the cross-shore and alongshore velocity components [Lanckriet and Puleo, 2013]. The structure function was then fitted to

$$D(z_s, r, t) = N + Ar^{\frac{2}{3}}, \tag{4.1}$$

where N and A are fitting parameters. N is indicative of measurement (Doppler) noise and A is a measure of the decorrelation of the velocity field with increasing separation distance due to turbulence [Brinkkemper et al., 2015; Lanckriet and Puleo, 2013; Wiles et al., 2006]. Subsequently, ε is calculated as

$$\varepsilon = \left(\frac{A}{C}\right)^{\frac{3}{2}}, \tag{4.2}$$

A time averaging window of 1.25 s with 50 % overlap was chosen for dissipation estimates. This value was selected based on the sensitivity analysis of the time averaging window length performed by Lanckriet and Puleo [2013]. Their analysis showed that dissipation rates were highly similar for window ranging from 1.25 to 3.5 s. Estimated values were rejected when the fit of equation 4.1 characterized by square of the correlation coefficient (R^2) was less than 0.70.

4.3.2 Bed Shear Stress

The bed shear stress, τ_i, can be determined using several methods applied to shallow water and near-bed velocity profiles. In the present study, two methods were used to estimate τ_i. The first method used was the von Karman-Prandtl relationship for fully developed hydraulic rough flow [Inch et al., 2015; Masselink and Russell, 2005; Puleo et al., 2014b, 2012; Raubenheimer et al., 2004] described as

$$u_i(z_s) = \frac{u_*}{\kappa} ln \frac{z_s}{z_0}, \tag{4.3}$$

where u_i ($= u, v$) velocity component (at 0.03 m below the ADPV transducer), $i = x, y$ component, u_* is the friction velocity, κ is the von Karman constant ($= 0.4$), and z_0 is the bed roughness. The velocity profile measurements permit calculate calculation of the u_* by performing a least squares regression between $u(z_s)$ and $ln(z_s)$. The slope (m) of the least squares fit when multiplied by κ yields u_*. The fundamental definition of u_* yields the bed shear stress (equation 2.1). The von Karman-Prandtl relationship [e.g., Inch et al., 2015; Masselink and Russell, 2005; Puleo et al., 2014a, 2012; Raubenheimer et al., 2004] requires a model skill cutoff to accept or reject such estimates. An R^2 cutoff of 0.7 was used as an indicator of poor model fit. During these instances, a second method, more often used, was implemented to reduce introduction of additional gaps in the bed shear stress time series.

The quadratic drag law was used to estimate the bed shear stress when the von Karman-Prandtl relationship model skill was poor (equation 4.3). The quadratic drag law has been widely applied in inner-surf and swash-zone studies where velocities are collected at a single or multiple elevations above the bed [e.g., Puleo et al., 2012; Raubenheimer et al., 2004]. The embedded friction coefficient was estimated using the Swart et al. [1974] formula (equation 3.2). Friction coefficient (c_f) estimates ranged from 0.01 to 0.2 (discussed in subsection 4.2) and are commensurate with values from sandy beaches reported in many prior studies [e.g., Hughes et al., 1997; Inch et al., 2015; Puleo et al., 2012, 2000; Raubenheimer, 2002] suggesting the use of Swart's formula is appropriate.

4.3.3 Suspended sediment transport rates

Suspended sediment concentration (SSC) measurements were used to estimate suspended sediment transport rates. SSC were extrapolated to sediment concentration profiles using a power-law approximation between sensors [Camenen and Larson, 2005] and a uniform profile below the lowest sensor with SSC equivalent to lowest OBS measurements [Puleo et al., 2014a]. The suspended sediment concentration profiles were used to obtain a gross first-order estimate of the suspended sediment transport rate using equation 3.3.

4.4 Results

4.4.1 Spectral signature

A spectral analysis was performed on water depth measurements from station 1 to calculate the relative energy levels during different wind conditions. Spectra were computed using Welchs average periodiogram method, dividing the water depth measurements into 30-min segments with 50 % overlap, tapered using a Hamming window. The incident frequency peak in the inner surf zone is evident from April 1^{th} to April 7^{th} ($f > 0.05$ Hz; Figure 4.6). The water depth spectra for the first days during land- and sea-breeze conditions had dominant peaks between 6 to 8 s. These periods are associated with low amplitude swell, generated by remnants of a high-pressure system that impacted the field site days before the field experiment started. The generated waves arrived to the inner surf/swash zones with minimum energy loss from the surf zone [Sonu et al., 1973]. As the swell energy decreased, high-frequency peaks (3 to 4 s), associated with local wind waves, prevailed during land- and sea-breeze conditions.

The land and sea breezes from April 5 to 7 reached similar wind speeds (10 m s^{-1}), and generate disturbances from the interaction between onshore- and offshore-directed flows. These interactions induced energetic inner-surf and swash-zone hydrodynamics and considerable sediment resuspension events (discussed in subsections 4.4 and 4.5).

During the onset of the Norte event (April 8^{th} to April 9^{th}), infragravity ($f <$ 0.05 Hz) and incident frequency ($f >$ 0.05 Hz) peaks were evident. No presence of land breeze events were observed during the onset of the Norte. Swell peaks (8 to 9 s) and infragravity periods (23 - 45 s) were observed during the peak conditions generated by the Norte. After the Norte (April 10^{th} to April 11^{th}), incident frequencies dominated while infragravity frequencies decrease progressively and land- and sea-breeze events resumed.

4.4.2 Swash oscillations

The instantaneous shoreline was monitored from runup timestacks data for 3 days (April 4, 5, and 8) during daylight hours (Figure 4.6 red lines). For the first two days, land-breeze events were dominated by incident frequencies, related to wind waves. Infragravity motions were measured during sea-breeze events. Meanwhile, during the Norte, the swash oscillation spectrum indicates several peaks (at 5,11, and 19 s) within the infragravity and incident frequencies. A noticeable feature was that the incident frequency peaks were quite similar between both spectral analyses. This similarity is attributed to the flow interaction processes in the inner surf zone. Figure 4.6(blue lines) is based on vertical variation at a fixed location in the inner surf zone measuring mostly the flow interactions, while this analysis considered the swash oscillation across the foreshore. Because the foreshore acts as a low-pass filter, only the longer periods were observed in the runup timestacks.

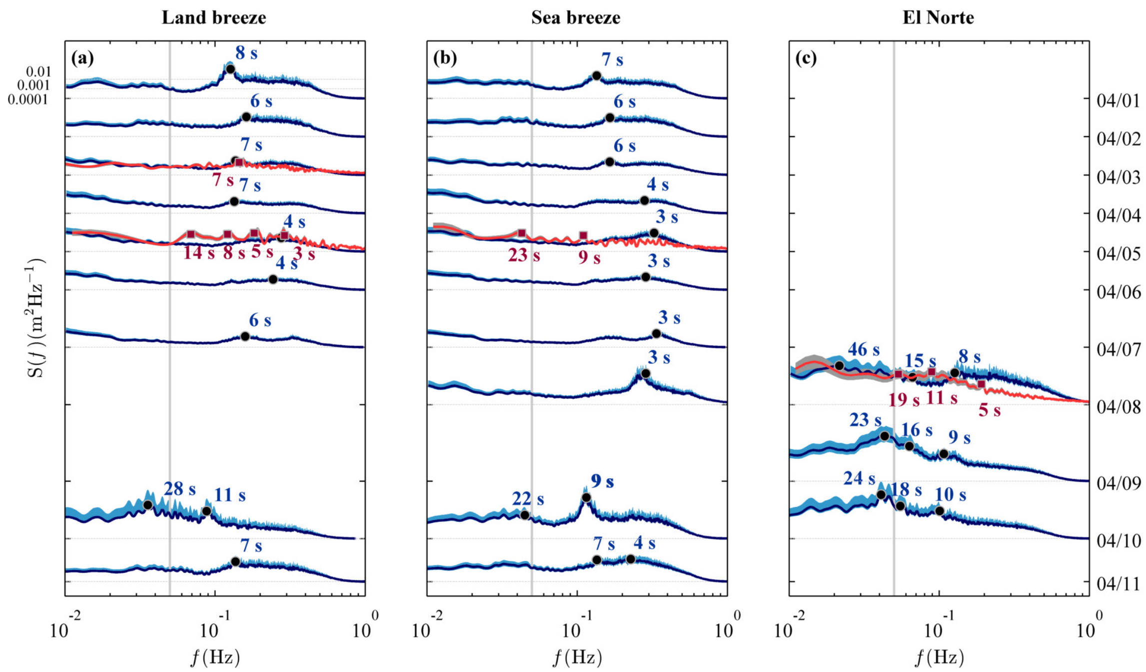

Figure 4.6. Water depth spectrum from PT data from station 1 (blue lines) and swash oscillation spectrum from runup timestacks data (red lines) for: (a) land breeze; (b) moderate sea breeze; (c) strong sea breeze; (d) the Norte wind events. Shaded bars are the 95 %-confidence bounds. Vertical gray line identifies the division between the infragravity and incident frequencies (0.05 Hz; 20 s). Horizontal dashed line denotes the datum for the spectral energy.

Maximum runup is defined as the elevation of individual water-level maxima above the still-water level, considering setup and swash [Stockdon et al., 2006; Holman, 1986; Holland and Holman, 1993]. A noticeable difference was observed between land breeze and the other two conditions. From this analysis, it is evident that as the wind field intensifies, the swash excursion extends farther landward. However, it would have been expected that sea breezes had a larger landward extent than land breezes. However, this did not occur because sea-breeze events occurred during ebb (Figure 4.3). The 2% exceedance value for runup, $R_{2\%}$, was calculated from the cumulative probability density function of runup elevations (Figure 4.7). During land breeze, the maximum runup was 0.30 m. Meanwhile, during sea-breeze and the Norte conditions, the maximum runup was 0.21 m and 0.65 m, respectively.

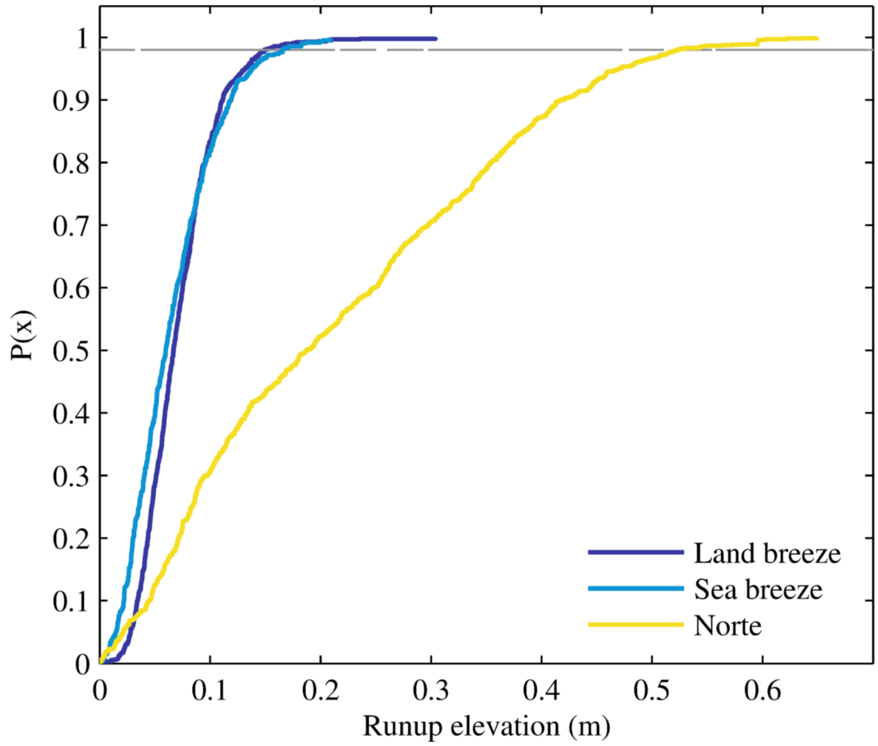

Figure 4.7. The 2% exceedance value of runup, $R_{2\%}$ (horizontal gray line),as calculated from the cumulative probability density function of runup elevations.

4.4.3 Hydrodynamics parameters

A 60-s time-series excerpt of instantaneous measurement of hydrodynamics parameters at each station for each wind condition is shown in Figure 4.9. The change in wind speed and direction induced pronounced changes to the inner-surf and swash-zone hydrodynamics.

Water depth measurements were used to identify the zones inundated by the runup. Depth measurements are also often used to identify the initiation of flow cycles (onshore-directed and offshore-directed flows). These cycles initiate with the bore arrival, commonly identified by the occurrence of local maxima in the water depth (Figure 4.9a; t = 15 s). As the collapsing bore propagates into the swash zone (farther up the foreshore; from stations 1 to 3) and reverses, the water depth decreases. During land- and sea-breeze conditions, the water level covered station 1. Meanwhile, stations 2 and 3 were occasionally reached when the water level increased and longer period waves were present. Hence, the seaward instrument station 1 was submerged throughout the study period while stations 2 and 3 were inundated occasionally by swash events. During the Norte all stations were submerged.

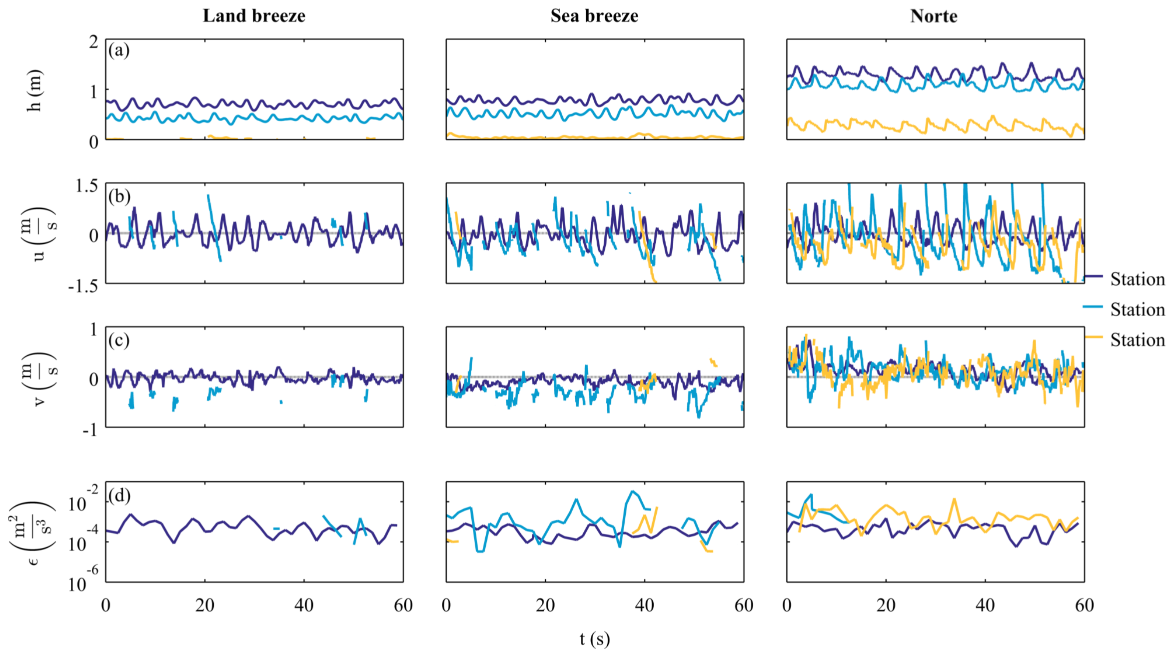

Figure 4.8. Time series excerpt of inner surf and swash-zone dynamics for each station during land-breeze, sea-breeze, and El Norte event: (a) water depth; (b) cross-shore velocity (positive values indicate onshore-directed flow; negative values indicate offshore-directed flow); (c) alongshore velocity; (d) turbulence dissipation rate.

Figures 4.8b and 4.8c show the corresponding cross-shore and alongshore velocity time series from roughly 0.015 m above the bed. Onshore-directed (offshore-directed) flow velocity, during land-breeze conditions, varied between 0.98 to 1.42 m s^{-1} (-0.67 to -1.86 m s^{1}) in the inner surf and between 1.00 to 1.87 m s^{-1} (-0.63 to -1.98 m s^{-1}) in the swash zone. Meanwhile, during sea-breeze conditions, onshore-directed (offshore-directed) flow velocity of 1.11 to 2.20 m s^{-1} (-0.82 to -2.50 m s^{-1}) and 0.85 to 2.26 m s^{-1} (-0.67 to -2.40 m s^{-1}) in the inner surf and swash zone, respectively, was observed. Onshore-(offshore-) directed flow velocities at station 3 were 0.80 (-0.90) m s^{-1} different than the flow velocities measured at the other stations. Onshore-directed (offshore-directed) flow velocity during the Norte varied between 1.76 to 1.96 m s^{-1} (-1.50 to -2.13 m s^{-1}) in the inner surf and 1.68 to 2.47 m s^{-1}(-1.64 to -2.40 m s^{-1}) in the swash zone. Flow velocities during sea breeze and the Norte reached similar maximum velocities, while during land breeze the maximum flow velocities were slower.

Alongshore flows were mostly unidirectional (Figure 4.8c) and aligned with the direction of the winds and waves (Figure 4.3). Maximum cross-shore and alongshore flow velocities were measured at station 2 during each forcing condition, where bore arrival/collapse frequently occurred. Alongshore flow velocity magnitudes, during land breeze conditions, often exceeded 0.4 m s^{-1} and 0.8 m s^{-1} in the inner surf and swash zone, respectively. Meanwhile, during sea breeze, flow velocity magnitudes of 0.7 to 2.3 m s^{-1} and 0.7 to 1.5 m s^{-1} during the Norte conditions were observed. During the Norte, alongshore velocities were less than during sea breeze, evidence that the stronger flows were mostly cross-shore directed.

The structure function method relies on vertical profile of w' and did not consider the velocity profile within 0.005 m of the bed and the top of the measured profile due to required separation distance for the calculation (equation 2.9; Figure 4.8). Turbulence dissipation rates estimated ranged between $O(10^5$ m^2 s$^3)$ to $O(10^2$ m^2 s$^3)$ during land breeze and between $O(10^3$ m^2 s$^3)$ to $O(10$ m^2 s$^3)$ during sea-breeze and the Norte conditions. Gaps in the turbulence dissipation rate time series are due to poor agreement between the measured structure function (equation 2.9) and the $D(z_s) \sim r^{(2/3)}$ scaling. It is evident that the turbulence dissipation rates tend to increase with decreasing water, as observed in previous studies [e.g., Lanckriet and Puleo, 2013; Brinkkemper et al., 2015; Raubenheimer et al., 2004].

4.4.4 Sediment transport parameters

A 60-s time-series excerpt of instantaneous measurement of sediment transport parameters at each station for each wind condition is shown in Figure 4.9. Both cross-shore and alongshore velocity time series (Figures 4.9a - 4.9d) are presented.

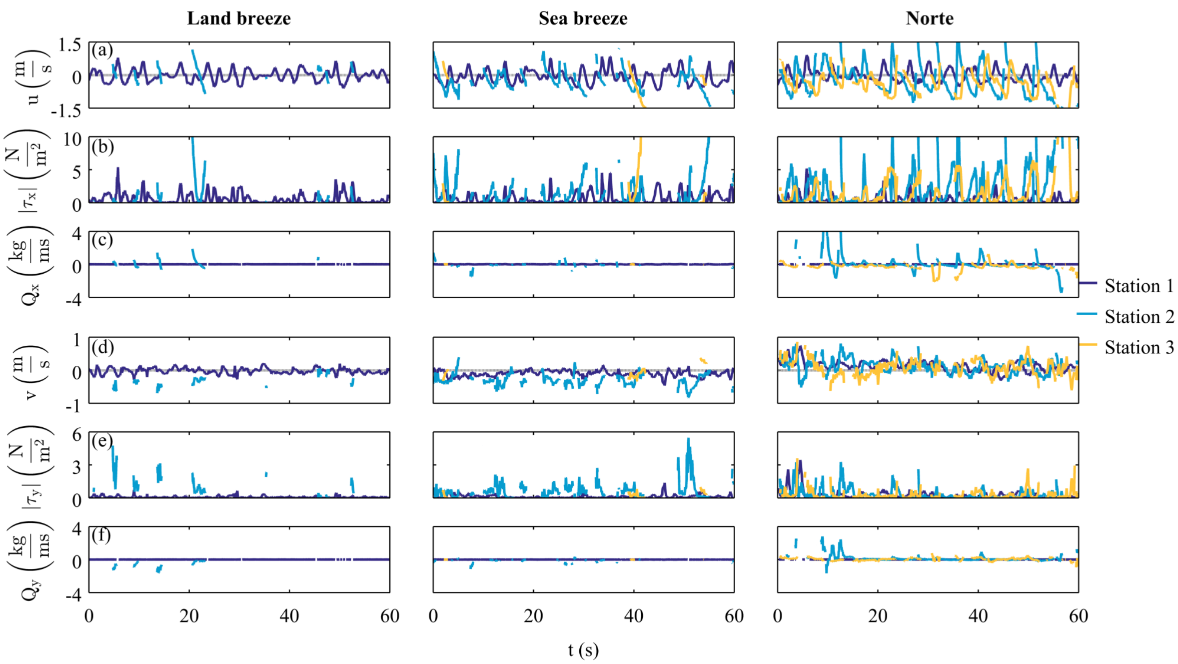

Figure 4.9. Time series excerpt of inner-surf and swash-zone dynamics for each station during land-breeze, sea-breeze, and El Norte event: (a) cross-shore velocity (positive values indicate onshore-directed flow; negative values indicate offshore-directed flow); (b) cross-shore shear stress magnitude; (c) cross-shore suspended sediment transport rate; (d) alongshore velocity; (e) alongshore shear stress magnitude; (f) alongshore suspended sediment transport rate.

There is considerable variability in the bed shear stress magnitudes between stations (Figures 4.9b - 4.9e). The bed shear stresses were weaker in the inner surf zone (station 1), when the bed was consistently submerged. Maximum bed shear stresses were frequently observed at the end of the offshore-directed flows measured at all stations (Figures 4.9a - 4.9d). The cross-shore (alongshore) bed shear stress magnitudes, during land-breeze conditions, reached a maximum of 20 N m^{-2} (15 N m^{-2}) in the inner surf and 28 N m^{-2} (17 N m^{-2}) in the swash zone. Bed shear stresses were of similar magnitude during the sea-breeze/ Norte conditions, where swash events were more frequent and swash-swash interactions more prevalent. Cross-shore bed shear stress reached a maximum of 19 N m^{-2} in the inner surf zone and 36 N m^{-2} in the swash zone. Whereas, maximum alongshore bed shear stress magnitude in the inner surf zone was 6 N m^{-2} and 28 N m^{-2} in the swash zone. Cross-shore bed shear stress generally dominated, as observed from the mean $|\tau_x|/|\tau_y|$ (Figure 4.10). However, the large value of frequency of occurrence and standard deviation indicated that the along-shore component is important and cannot be assumed negligible.

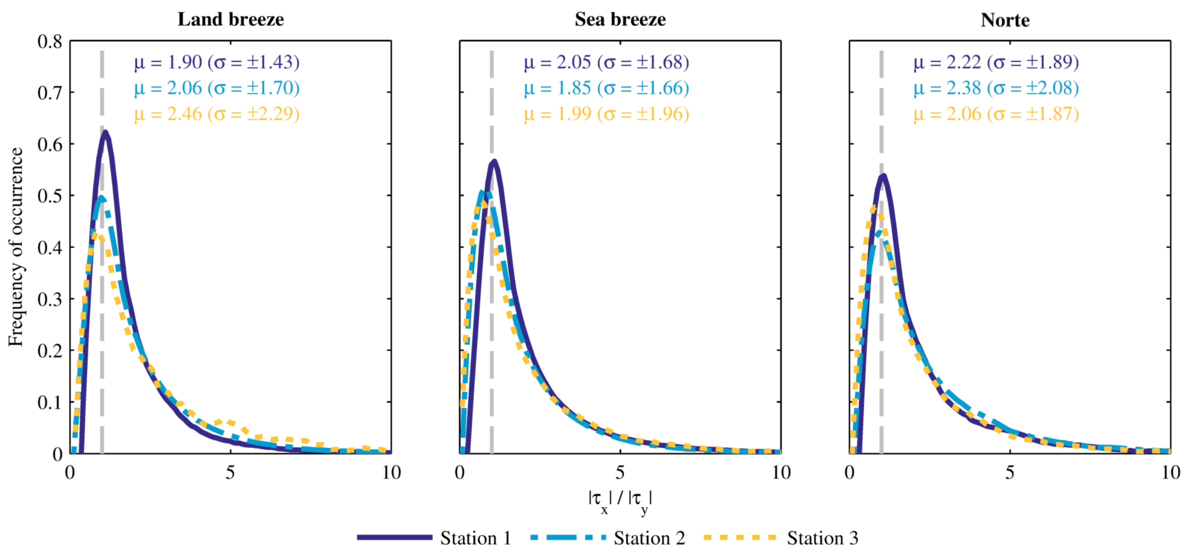

Figure 4.10. Ratios between the cross-shore and alognshore bed shear stress magnitudes at eact station during each forcing condition. Vertical dashed line identifies the ratio equal to 1.

The friction coefficients used to estimate bed shear stresses varied considerably between stations and forcing conditions (Figure 4.11). Larger friction coefficients were estimated at station 1 during all forcing conditions. However, the major difference was mostly due to the forcing conditions. During land and sea breezes, the friction coefficients range from 0.003 to 0.2. Meanwhile, friction coefficients were one order of magnitude smaller during the Norte (c_f = 0.01- 0.04). These values were similar to those reported previously for sandy beaches [e.g., Hughes et al., 1997; Inch et al., 2015; Puleo et al., 2012, 2000; Raubenheimer et al., 2004]. The difference between the forcing conditions, were mostly due to the flow velocities being larger during the Norte.

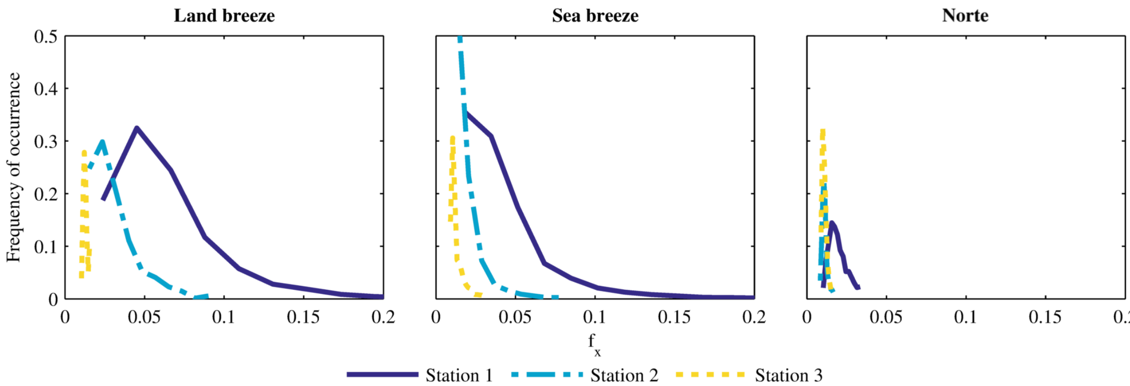

Figure 4.11. Histogram of friction coefficient for cross-shore flows for each station and forcing condition.

Suspended sediment concentrations occurred at the start of the flow cycle (onshore-directed flows) and maximum values were estimated at station 2. Large sediment suspension events were observed more frequently during the Norte. Suspended sediment transport rates decrease between stations and increase as forcing conditions intensified. Cross-shore and alongshore suspended sediment transport rates between station 1 ($O(0.1$ kg m^{-1} s$^{-1}))$ and the others ($O(1$ kg m^{-1} s$^{-1}))$ varied by an order of magnitude. Alongshore suspended sediment transport rates were, for the most part, unidirectional and reached similar magnitudes as the cross-shore component. Maximum cross-shore suspended sediment transport rates did not vary significantly between onshore-directed and offshore-directed phases ($\pm = 0.01$ kg m^{-1} s^{-1}; Table 4.1). During land- and sea-breeze conditions, the net sediment transport tended to be easterly-directed, while westerly-directed during the Norte. Similarity between cross-shore and alongshore swash-zone flow estimated parameters during land-/sea-breeze and the Norte conditions indicate that the cumulative effect of daily land/sea breezes can be similar or greater than the effects generated by a short duration Norte.

Table 4.1. Maximum cross-shore and alongshore suspended sediment transport rates in the inner surf and swash zones during different forcing conditions.

	Maximum cross-shore (alongshore) suspended sediment transport rate ($Q_x \equiv$ kg m^{-1} s^{-1})		
	Land breeze	Sea breeze	El Norte
Inner surf	0.35 (0.34)	1.70 (0.84)	2.55 (1.17)
Swash zone	12.0 (5.30)	12.72 (8.14)	17.80 (10.81)

The ratio of $|Q_x|/|Q_y|$ indicates that the cross-shore suspended sediment transport rates were generally dominant (Figure 4.12), similar to the bed shear stress ratios. However, the large standard deviation suggests that the alongshore component is not negligible and the exclusion the of the alongshore component in sediment transport calculations could lead to large errors. Differences between wind forcing conditions were observed at stations 2 and 3. As expected, fewer events occurred during land breezes compared to the transport rates during sea breezes. During land- and sea-breeze events, stations 2 and 3 were mostly located in the swash zone. During the Norte, fewer events were observed at station 2 compared to the other two wind forcing conditions. This difference is attributed to the changes in water levels during the Norte, locating station 2 between the inner surf and swash zone.

4.5 Discussion

The change in wind speed and direction induced pronounced changes to the inner-surf and swash-zone dynamics. Field observations showed that larger inner-surf and swash-zone flows, bed shear stresses, turbulence intensity and sediment suspension occur during sea breezes and the Norte. Maximum values occurred at station 2, where bores frequently collapsed generating flow interactions and localized suspension.

Measured maximum onshore-directed velocities of 0.80 to 2.5 m s^{-1} and -0.67 to -2.50 m s^{-1} for offshore-directed velocities were similar to previous estimates on steep sandy foreshores [Conley and Griffin, 2004; Houser and Barrett, 2010; Shanehsazzadeh and Holmes, 2007]. Cross-shore velocity magnitudes between sea-breeze and the Norte

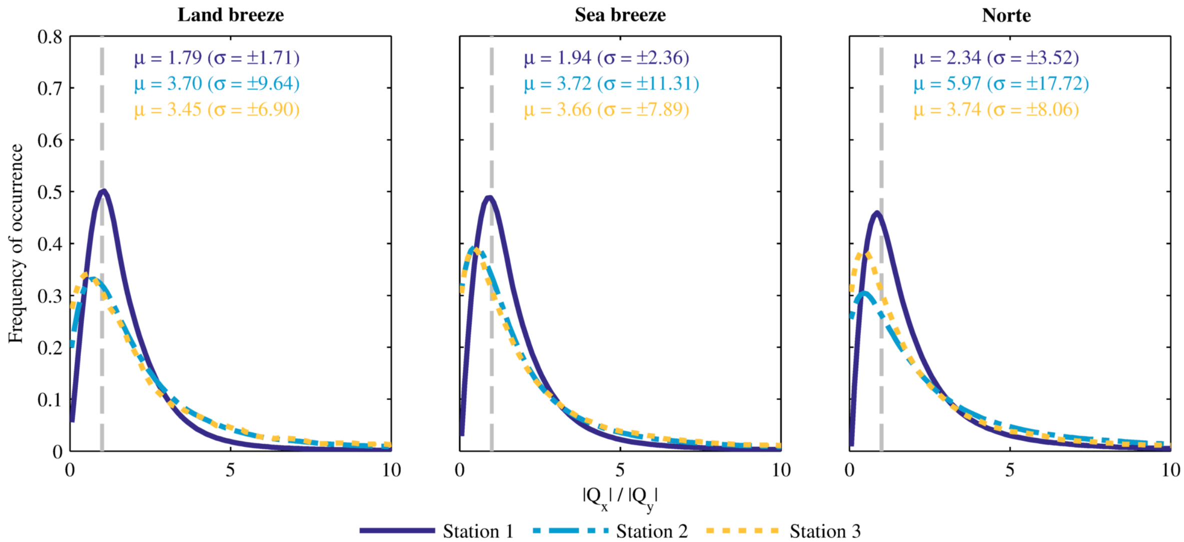

Figure 4.12. Ratios between the cross-shore and alognshore suspended sediment transport rate magnitudes at eact station during each forcing condition. Vertical dashed line identifies the ratio equal to 1.

conditions reached similar values, whereas land breeze velocity magnitudes were often smaller by more than 0.6 m s^{-1}. Cross-shore bed shear stress magnitudes were smaller, by one order of magnitude, to those reported previously for sandy beached on moderately sloped foreshore [Miles et al., 2006]. However, the Miles et al. [2006] study was performed on a macrotidal beach with stronger flows and hydrodynamic forcing conditions. Bed shear stresses were consistent with those from sandy beaches on low gradient slopes [Austin et al., 2011; Inch et al., 2015; Masselink and Russell, 2005; Puleo et al., 2014a, 2012]. Maximum cross-shore bed shear stress magnitudes ranged between $O(10^1$ N m$^{-2})$ to $O(10$ N m$^{-2})$. Differences in flow velocities suggest that larger bed shear stress should occur during sea breezes and the Norte. However, friction coefficients were one order of magnitude smaller during strong wind conditions, reducing the bed shear stress values during sea breeze and the Norte. Suspended sediment concentration (exceeding 50 kg m^{-3}) was measured during the largest cross-shore and alongshore velocities. Alongshore flow velocity magnitudes were similar to their cross-shore-directed counterparts during sea breezes, but smaller during land breezes and the Norte. This difference was mostly due to the wind and dominant wave direction. Alongshore bed shear stress reached similar values as the cross-shore directed values. Turbulence dissipation rates, during land-breeze events, ranged from $O(10^{-5}$ m^2 s$^{-3})$ to $O(10^{-2}$ m^2 s$^{-3})$. However, during sea-breeze and the Norte conditions, dissipation rates were similar ranging between $O(10^{-3}$ m^2 s$^{-3})$ to $O(10$ m^2 s$^{-3})$. A higher range of dissipation rates ($O(10^{-3}$ m^2 s$^{-3})$ to $O(10$ m^2 s$^{-3})$) was estimated at station 2 due to intermittent wave breaking at the site generating high levels of turbulence. These estimates exceeded values reported in previous studies ($O(10^{-5}$ m^2 s$^{-3})$ to $O(10^{-3}$ m^2 s$^{-3})$) [Brinkkemper et al., 2015; Lanckriet and Puleo, 2013; Raubenheimer et al., 2004; Sou et al., 2010]. The differences between the estimated and previously reported rates can be related to differences in the method selected to estimate ε, field site morphology, offshore wave forcing, and vertical sensor position. The turbulence intensity increased with decreasing water depth [Brinkkemper et al., 2015; Lanckriet and Puleo, 2013; Raubenheimer et al., 2004; Sou et al., 2010].

The growth of energy levels in the wave climate resulted in almost a continuous suspension of sediment at station 1 and occasionally at station 2 and 3 [Inman and Filloux, 1960; Masselink, 1998; Pattiaratchi et al., 1997]. During the Norte, large suspended sediment transport rates were more frequently observed, as expected. However, considerable sediment suspension was measured during land and sea breezes. Most of the land-breeze events occurred during high tide. During these instances, land breeze transport rates reached similar values to those estimated during sea breezes. Therefore, when wave climate intensifies and coincides with high water levels, most of the foreshore is inundated and the sediment transport is more significant [Inman and Filloux, 1960].

Thirty-minute time-averaged mean cross-shore and alongshore sediment transport rates were computed at each station during land/sea breezes (Figure 4.13 light and gray panels) and Norte (Figure 4.13 dark gray panel). The mean inner-surf suspended sediment transport rates were similar during all wind forcing conditions ranging between $\pm$ 0.1 kg m^{-1} s^{-1} (station 1;Figure 4.13 dark blue). Whereas, the mean suspended sediment transport rates at other stations were small, ranging between $\pm$ 0.4 kg m^{-1} s^{-1}. Similarities between cross-shore and alongshore mean suspended sediment transport rates magnitudes during sea breezes and the Norte (Figures 4.13b and 4.13c) suggest that sea-breeze effects may be compared to those generated by a short duration small storm. However, despite the milder energy conditions during land breezes, when these coincide with high tides, the estimated mean suspended sediment transport rates were commensurate to those estimated during sea-breeze events. The similarities are partially attributed to the fact that land breezes occurred mostly during high water, mobilizing considerable amount of sediment across the foreshore. These observations suggest under ideal conditions (strong wind, large waves, and high water levels), any wind forcing condition can mobilize a considerable amount of sediment across the foreshore, even if the dominant wind direction is from the land. These mean of the suspended sediment transport rates suggests that the foreshore change might be caused by numerous small instantaneous sediment rates, noted in several recent studies [Austin and Masselink, 2006; Blenkinsopp et al., 2011; Masselink et al., 2009; Puleo et al., 2014b].

A dominant pattern between forcing conditions and suspended sediment transport rates was observed. During sea breezes and Norte, cross-shore suspended sediment transport rates were mostly negative, suggesting that erosive conditions dominated. However, after the Norte, the suspended sediment transport rates during sea breezes were positive. This difference can be ascribed to the low mean water levels which generated wave conditions similar as post-storm wave conditions, thereby moving sediment onshore. Meanwhile, during land breeze, cross-shore suspended sediment transport rate were mostly positive, suggesting that the foreshore accreted. Previous studies suggest that the land/sea breeze cycles erodes and accretes the foreshore and such daily cycle is analogous to the storm cycle or the seasonal morphological cycle [Inman and Filloux, 1960; Komar, 1976; Masselink, 1998; Pattiaratchi et al., 1997]. However, this analysis does not quantified the associated foreshore morphological changes during the different forcing conditions, but confirms how sediment transport processes varied depending on wind conditions. Meanwhile, alongshore suspended sediment transport rates were unidirectional and aligned with the direction of the wind. The alongshore suspended sediment transport rates were easterly-directed ($\bar{Q}_y < 0$) and westerly-directed ($\bar{Q}_y > 0$) when winds were blowing from a easterly/northeasterly and north/northwesterly direction, respectively.

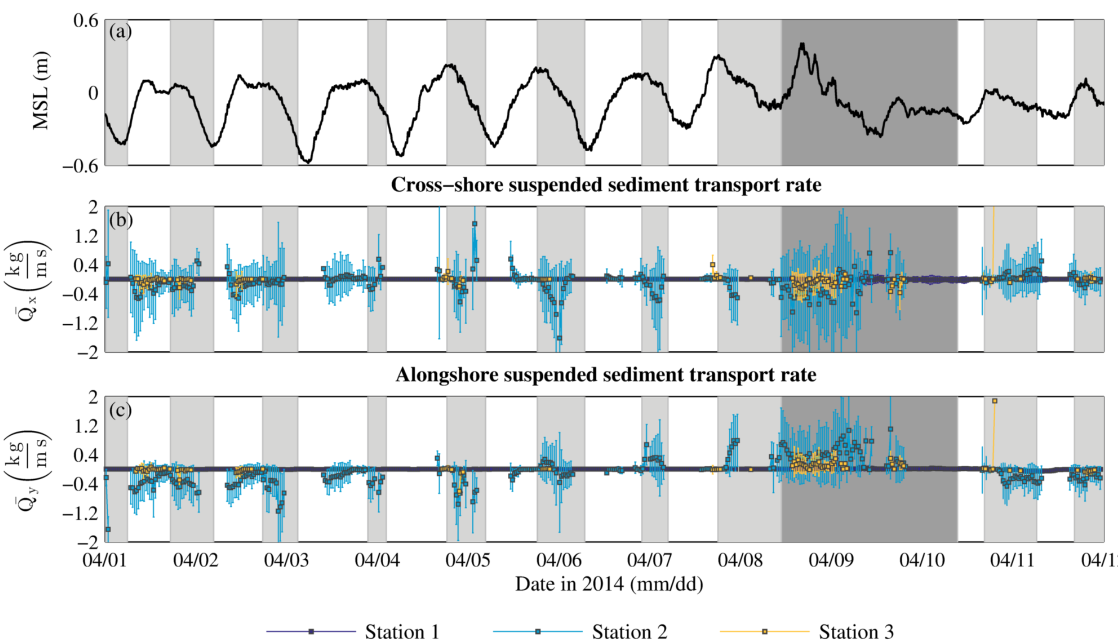

Figure 4.13. Time series of: (a) mean sea level (MSL); (b) 30-minute time-averaged mean and standard deviation (error bar) of cross-shore suspended sediment transport rate ($\bar{Q}_x$); and (c) 30-minute time-averaged mean and standard deviation (error bar) of alongshore suspended sediment transport rate ($\bar{Q}_y$) during land breezes (white panels), sea breezes (light gray panels) and Norte (dark gray panel).

The temporal and spatial variation of net and absolute values of cross-shore and alongshore sediment transport rates (Figure 4.14) support the notion that during strong sea breezes a significant amount of sediment can be mobilized similar or greater than the effects generated by a small storm. The net cross-shore and alongshore suspended sediment transport rates (Figures 4.14a and 4.14b) at stations 1 and 3 were small, suggesting that minimal morphological change occurred at those locations. Net cross-shore suspended sediment transport rates between sea-breeze and the Norte events reached similar values, however alongshore net suspended sediment transport rates were in the opposite direction mostly due to the wind and wave direction during each forcing conditions. At station 2, a net offshore suspended sediment transport rate and a unidirectional alongshore suspended sediment transport rate was measured. However, temporal gaps due to intermittency in the measurement of aerated and turbulent flows generated by collapsing bores, were a major limitation in quantifying sediment transport, particularly onshore-directed transport. Hence, if temporal gaps during onshore-directed transport are circumvented using other measuring approaches (e.g., remote sensing, non-intrusive sensors), the net sediment transport rate at station 2 might be similar to the other stations. The sum of the absolute of all cross-shore and alongshore suspended sediment transport rates (Figures 4.14c and 4.14d) confirmed that all conditions could mobilize a large quantity ($Q_{i_{abs}} > 5000$ kg m^{-1} s^{-1}) of sediment across the foreshore. However, due to the intensity and frequency of sea breezes, these wind-forcing conditions mobilized a greater quantity of sediment. Thereby, sea-breeze events play a major role in controlling the foreshore morphological processes on this low energy microtidal beach.

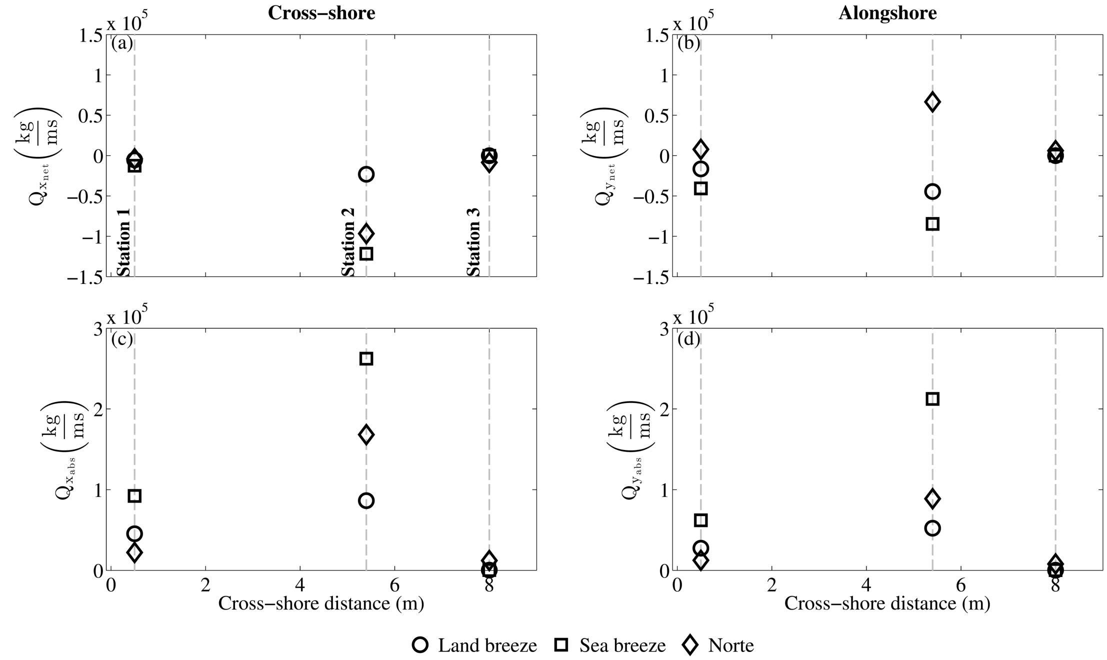

Figure 4.14. (a) Net cross-shore sediment transport rate; (b) net alongshore sediment transport rate; (c) sum of the absolute of all cross-shore sediment transport rates; and (d) sum of the absolute of all alongshore sediment transport rates at each station during (○) land breeze, (□) sea breeze and (◊) Norte. Vertical dashed gray lines mark the cross-shore location of the stations.

4.6 Conclusions

The effects of sea breeze on swash-zone dynamics, during local (land/sea breeze) and synoptic (Norte) scale meteorological events were investigated on a microtidal, low energy, sandy beach. The data presented provide the first estimates of small-scale inner-surf and swash-zone hydrodynamics and sediment transport processes during these different wind forcing conditions. The results indicated that:

1. Despite the milder energy conditions during land breezes, when these coincide with high tides, the estimated instantaneous hydrodynamic and sediment transport parameters often had similar orders of magnitude to sea breezes.

2. Flows forced by daily sea breeze can mobilize a large quantity of sediment on the same order of magnitude as sediment mobilized by the hydrodynamics associated with a short duration small storm (Norte).

3. The sum of the absolute of all cross-shore and alongshore suspended sediment transport rates at each station during each wind forcing condition, confirmed that all conditions could mobilize large quantities of sediment across the foreshore. However, sea breezes induced more suspension events due to their frequent occurrence. Thus, sea-breeze events play a major role in controlling the foreshore morphological processes on this low energy, microtidal beach.

Chapter 5

CONCLUSIONS

This work described field measurements and measurement techniques to understand the relation of small-scale inner-surf and swash-zone processes to post-storm beach recovery (accretive conditions) and mesoscale meteorological phenomena (wind forcing mechanism). Arrays of sensors were used to simultaneously measure fluid velocities, sediment concentrations, water depth, and bed level change at multiple cross-shore locations across the foreshore and estimate hydrodynamics and sediment transport parameters. The acquired near-bed measurements provided valuable information. In terms of understanding accretive conditions, it was found that on steeper reflective beaches the effect of flow interactions increased the localized suspension and advection of sediment from the point of bore collapse at the inner surf zone or seaward swash zone and deposited landward, mostly by the cross-shore component. However, the alongshore hydrodynamic and sediment transport parameters can reach similar magnitude, compared to cross-shore component, being a potential mechanism to enhance sediment transport. *In situ* measurements showed that when cross-shore flows decelerate, alongshore flows accelerate suggesting that sediment is maintained in suspension for a longer duration than a cross-shore only model would predict. Thus, the exclusion of alongshore-directed bed shear stress in cross-shore sediment transport formulations will underpredict the sediment transport rate and may lead to poor model skill. The rapid vertical growth of the foreshore occurred during high tide and mostly due to the runup excursion length (water level) that overtopped the berm, transporting suspended sediment farther up the foreshore. However, the sediment transport rate estimates are contrary to the observed foreshore morphological change. Net sediment transport and the associated foreshore morphological change were quantified via cross-shore suspended sediment transport rate gradients and an energetics-based suspended sediment transport model in an effort to account for possible inconsistencies with *in situ* measurements. The analysis of morphological change focused only on cross-shore sediment transport rate gradients since the alongshore bathymetric variability quantified during the first field experiment was small. Net suspended sediment transport rate gradient estimates exceeded by two orders of magnitude the net transport quantified via bathymetric difference over each tidal cycle, highlighting the difficulty of predicting transport processes even under weak accretion conditions. Temporal data gaps were a major limitation in quantifying sediment transport, particularly onshore-directed transport, due to issues with instrumentation not being capable of measuring the total spatial and temporal variability of the inner-surf and swash-zone dynamics. Cross-shore suspended sediment transport rate gradients estimated using Bagnold's formula confirmed that this model is not reliable on steep reflective beaches. These discrepancies imply that all potential mechanisms that enhance sediment transport (e.g. turbulence generated by swash bores, sediment advection) and complete measurements for the full flow duration and throughout the water column are needed to improve sediment transport rate estimates in the inner-surf and swash zone. Data gaps can be circumvented using remote sensing techniques, non-intrusive sensors, or larger arrays of collocated sensors. Despite the poor agreement, the estimated parameters served to relate the small-scale processes to large temporal and spatial scale accretive patterns.

The effects sea breeze on swash-zone dynamics, during local (land/sea breeze) and synoptic (Norte) scale meteorological events were investigated on a microtidal, low energy, sandy beach. Flow velocities and suspended sediment concentrations were measured concurrently at three cross-shore locations to quantify bed shear stress, turbulent dissipation rate and sediment transport rates. Field observations showed that strong inner-surf and swash-zone bed shear stresses, turbulence intensity and sediment suspension occur during sea breezes and Norte. However, despite the milder energy conditions during land breezes, when these coincide with high tides, the estimated instantaneous hydrodynamic and sediment transport parameters often had similar orders of magnitude to sea breezes. The temporal and spatial variation of net and absolute values of cross-shore and alongshore sediment transport rates support the notion that during strong sea breezes a significant amount of sediment can be mobilized similar or greater than the effects generated by a small storm (Norte). The net cross-shore and alongshore suspended sediment transport rates at stations 1 and 3 were small, suggesting that minimal morphological change occurred at those locations. At station 2, a net offshore suspended sediment transport rate and a unidirectional alongshore suspended sediment transport rate was measured. Previous studies suggest that the land/sea breeze daily cycle is analogous to the storm cycle or the seasonal morphological cycle. Hence, if temporal gaps, due to intermittency in the measurements, during onshore-directed transport are circumvented using other measuring approaches (e.g., remote sensing, non-intrusive sensors), the net sediment transport rate at station 2 might be small; therefore supporting the finding of previous studies. The absolute sum of all cross-shore and alongshore suspended sediment transport rates at each station during each wind forcing condition, confirmed that all conditions could mobilize large quantities of suspended sediment across the foreshore. However, sea breezes induced more suspension events due to their frequent occurrence. Hence, sea-breeze events are an important forcing mechanism controlling foreshore morphological processes.

References

Aagaard, T. and Greenwood, B. (1995). Suspended sediment transport and morphological response on a dissipative beach. *Continental Shelf Research*, 15(9):1061–1086.

Aagaard, T. and Holm, J. (1989). Digitization of Wave Run-up Using Video Records. *Journal of Coastal Research*, 5(3):547–551.

Aagaard, T., Hughes, M., Baldock, T., Greenwood, B., Kroon, A., and Power, H. (2012). Sediment transport processes and morphodynamics on a reflective beach under storm and non-storm conditions. *Marine Geology*, 326328:154–165.

Aagaard, T., Hughes, M., Mller-Srensen, R., and Andersen, S. (2006). Hydrodynamics and Sediment Fluxes across an Onshore Migrating Intertidal Bar. *Journal of Coastal Research*, 22(2):247–259.

Aagaard, T. and Hughes, M. G. (2006). Sediment suspension and turbulence in the swash zone of dissipative beaches. *Marine Geology*, 228(14):117–135.

Abbs, D. J. and Physick, W. L. (1992). Sea-breeze observartions and modelling: a review. *Aust. Meteorol. Mag.*, (41):9–19.

Adrian, R. J. (1991). Particle-Imaging Techniques for Experimental Fluid Mechanics. *Annual Review of Fluid Mechanics*, 23(1):261–304.

Alsina, J. M. and Caceres, I. (2011). Sediment suspension events in the inner surf and swash zone. Measurements in large-scale and high-energy wave conditions. *Coastal Engineering*, 58(8):657–670.

Alsina, J. M., Caceres, I., Brocchini, M., and Baldock, T. E. (2012). An experimental study on sediment transport and bed evolution under different swash zone morphological conditions. *Coastal Engineering*, 68:31–43.

Alsina, J. M., Falchetti, S., and Baldock, T. E. (2009). Measurements and modelling of the advection of suspended sediment in the swash zone by solitary waves. *Coastal Engineering*, 56(56):621–631.

Amoudry, L., Hsu, T.-J., and Liu, P. L.-F. (2008). Two-phase model for sand transport in sheet flow regime. *J. Geophys. Res.*, 113(C3):C03011.

Astier, J., Astruc, D., Lacaze, L., and Eiff, O. (2012). Investigation of the swash zone evolution at wave time scale. Santander, Spain.

Astruc, D., Cazin, S., Cid, E., Eiff, O., Lacaze, L., Robin, P., Toublanc, F., and Caceres, I. (2012). A stereoscopic method for rapid monitoring of the spatio-temporal evolution of the sand-bed elevation in the swash zone. *Coastal Engineering*, 60:11–20.

Austin, M. J. and Buscombe, D. (2008). Morphological change and sediment dynamics of the beach step on a macrotidal gravel beach. *Marine Geology*, 249(34):167–183.

Austin, M. J. and Masselink, G. (2006). Observations of morphological change and sediment transport on a steep gravel beach. *Marine Geology*, 229(12):59–77.

Austin, M. J., Masselink, G., Russell, P. E., Turner, I. L., and Blenkinsopp, C. E. (2011). Alongshore fluid motions in the swash zone of a sandy and gravel beach. *Coastal Engineering*, 58(8):690–705.

Bagnold, R. A. (1966a). An approach to the sediment transport problem from general physics. USGS Numbered Series 422-I, U. S. Govt. Print. Off.

Bagnold, R. A. (1966b). The Shearing and Dilatation of Dry Sand and the 'Singing' Mechanism. *Proc. R. Soc. A*, 295(1442):219–232.

Bakhtyar, R., Barry, D. A., Li, L., Jeng, D. S., and Yeganeh-Bakhtiary, A. (2009). Modeling sediment transport in the swash zone: A review. *Ocean Engineering*, 36(910):767–783.

Baldock, T. E. and Alsina, J. (2013). Impact of beach scraping on near shore sediment transport and bar migration. pages 1–6. Engineers Australia.

Baldock, T. E., Grayson, R., Torr, B., and Power, H. E. (2014). Flow convergence at the tip and edges of a viscous swash front Experimental and analytical modeling. *Coastal Engineering*, 88:123–130.

Baldock, T. E. and Holmes, P. (1997). Swash Hydrodynamics on a Steep Beach. pages 784–793. ASCE.

Baldock, T. E. and Hughes, M. G. (2006). Field observations of instantaneous water slopes and horizontal pressure gradients in the swash-zone. *Continental Shelf Research*, 26(5):574–588.

Baldock, T. E., Hughes, M. G., Day, K., and Louys, J. (2005). Swash overtopping and sediment overwash on a truncated beach. *Coastal Engineering*, 52(7):633–645.

Baldock, T. E., Kudo, A., Guard, P. A., Alsina, J. M., and Barnes, M. P. (2008). Lagrangian measurements and modelling of fluid advection in the inner surf and swash zones. *Coastal Engineering*, 55(10):791–799.

Baldock, T. E., Tomkins, M. R., Nielsen, P., and Hughes, M. G. (2004). Settling velocity of sediments at high concentrations. *Coastal Engineering*, 51(1):91–100.

Barnes, M. P. and Baldock, T. (2007). Direct Bed Shear Stress Measurements in Bore-Driven Swash and Swash Interactions. In *Coastal Sediments '07*, pages 1947–1960.

Barnes, M. P. and Baldock, T. E. (2010). A Lagrangian model for boundary layer growth and bed shear stress in the swash zone. *Coastal Engineering*, 57(4):385–396.

Barnes, M. P., O'Donoghue, T., Alsina, J. M., and Baldock, T. E. (2009). Direct bed shear stress measurements in bore-driven swash. *Coastal Engineering*, 56(8):853–867.

Blenkinsopp, C. E., Mole, M. A., Turner, I. L., and Peirson, W. L. (2010a). Measurements of the time-varying free-surface profile across the swash zone obtained using an industrial LIDAR. *Coastal Engineering*, 57(1112):1059–1065.

Blenkinsopp, C. E., Turner, I. L., Masselink, G., and Russell, P. E. (2010b). Validation of volume continuity method for estimation of cross-shore swash flow velocity. *Coastal Engineering*, 57(10):953–958.

Blenkinsopp, C. E., Turner, I. L., Masselink, G., and Russell, P. E. (2011). Swash zone sediment fluxes: Field observations. *Coastal Engineering*, 58(1):28–44.

Bonte, Y. and Levoy, F. (2015). Field experiments of beach scarp erosion during oblique wave, stormy conditions (Normandy, France). *Geomorphology*, 236:132–147.

Briganti, R., Dodd, N., Pokrajac, D., and O'Donoghue, T. (2011). Non linear shallow water modelling of bore-driven swash: Description of the bottom boundary layer. *Coastal Engineering*, 58(6):463–477.

Briganti, R., Torres-Freyermuth, A., Baldock, T. E., Brocchini, M., Dodd, N., Hsu, T.-J., Jiang, Z., Kim, Y., Pintado-Patiño, J. C., and Postacchini, M. (2016). Advances in numerical modelling of swash zone dynamics. *Coastal Engineering*, 115:26–41.

Brinkkemper, J. A., Lanckriet, T., Grasso, F., Puleo, J. A., and Ruessink, B. G. (2015). Observations of turbulence within the surf and swash zone of a field-scale sandy laboratory beach. *Coastal Engineering*.

Brocchini, M. and Baldock, T. E. (2008). Recent advances in modeling swash zone dynamics: Influence of surf-swash interaction on nearshore hydrodynamics and morphodynamics. *Rev. Geophys.*, 46(3):RG3003.

Butt, T., Miles, J., Ganderton, P., and Russell, P. (2002). A simple method for calibrating optical backscatter sensors in high concentrations of non-cohesive sediments. *Marine Geology*, 192(4):419–424.

Butt, T. and Russell, P. (1999). Suspended sediment transport mechanisms in high-energy swash. *Marine Geology*, 161(24):361–375.

Butt, T. and Russell, P. (2000). Hydrodynamics and Cross-Shore Sediment Transport in the Swash-Zone of Natural Beaches: A Review. *Journal of Coastal Research*, 16(2):255–268.

Butt, T. and Russell, P. (2005). Observations of Hydraulic Jumps in High-Energy Swash. *Journal of Coastal Research*, 21(6):1219–1227.

Butt, T., Russell, P., Puleo, J., Miles, J., and Masselink, G. (2004). The influence of bore turbulence on sediment transport in the swash and inner surf zones. *Continental Shelf Research*, 24(78):757–771.

Butt, T., Russell, P., Puleo, J. A., and Masselink, G. (2005). The Application of Bagnold-Type Sediment Transport Models in the Swash Zone. *Journal of Coastal Research*, 21(5):887–895.

Butt, T., Tinker, J., Masselink, G., O'Hare, T., and Russell, P. (2009). Field Observations of Sediment Fluxes in the Inner-Surf and Swash Zones. *Journal of Coastal Research*, pages 991–1001.

Caceres, I. and Alsina, J. M. (2012). A detailed, event-by-event analysis of suspended sediment concentration in the swash zone. *Continental Shelf Research*, 41:61–76.

Camenen, B. and Larson, M. (2005). A general formula for non-cohesive bed load sediment transport. *Estuarine, Coastal and Shelf Science*, 63(12):249–260.

Capurro, L. R. A. and Reid, J. L. (1972). *Contributions on the physical oceanography of the Gulf of Mexico.* Gulf Pub. Co., Houston, Tex. OCLC: 513280.

Chardón-Maldonado, P., Pintado-Patiño, J. C., and Puleo, J. A. (2016). Advances in swash-zone research: Small-scale hydrodynamic and sediment transport processes. *Coastal Engineering*, 115:8–25.

Chassagneux, F. X. and Hurther, D. (2014). Wave bottom boundary layer processes below irregular surfzone breaking waves with light-weight sheet flow particle transport. *J. Geophys. Res. Oceans*, 119(3):1668–1690.

Conley, D. C. and Griffin, J. G. (2004). Direct measurements of bed stress under swash in the field. *J. Geophys. Res.*, 109(C3):C03050.

Cowen, E., Mei Sou, I., Liu, P., and Raubenheimer, B. (2003). Particle Image Velocimetry Measurements within a Laboratory-Generated Swash Zone. *Journal of Engineering Mechanics*, 129(10):1119–1129.

Craig, R., Loadman, C., Clement, B., Rusello, P., and Siegel, E. (2011). Characterization and testing of a new bistatic profiling acoustic Doppler velocimeter: The Vectrino-II. In *Current, Waves and Turbulence Measurements (CWTM), 2011 IEEE/OES 10th*, pages 246–252.

Dail, H. J., Merrifield, M. A., and Bevis, M. (2000). Steep beach morphology changes due to energetic wave forcing. *Marine Geology*, 162(24):443–458.

Dean, R. G. and Dalrymple, R. A. (2001). *Coastal Processes with Engineering Applications*. Cambridge University Press, Cambridge.

Desombre, J., Morichon, D., and Mory, M. (2013). RANS v2f simulation of a swash event: Detailed flow structure. *Coastal Engineering*, 71:1–12.

Dodd, N., Stoker, A. M., Calvete, D., and Sriariyawat, A. (2008). On beach cusp formation. *Journal of Fluid Mechanics*, 597:145–169.

Dong, L. P., Sato, S., and Liu, H. (2013). A sheetflow sediment transport model for skewed-asymmetric waves combined with strong opposite currents. *Coastal Engineering*, 71:87–101.

Downing, J. (2006). Twenty-five years with OBS sensors: The good, the bad, and the ugly. *Continental Shelf Research*, 26(1718):2299–2318.

Drake, T. G. and Calantoni, J. (2001). Discrete particle model for sheet flow sediment transport in the nearshore. *J. Geophys. Res.*, 106(C9):19859–19868.

Duncan Jr., J. R. (1964). The effects of water table and tide cycle on swash-backwash sediment distribution and beach profile development. *Marine Geology*, 2(3):186–197.

Elfrink, B. and Baldock, T. (2002). Hydrodynamics and sediment transport in the swash zone: a review and perspectives. *Coastal Engineering*, 45(34):149–167.

Elgar, S., Raubenheimer, B., and Guza, R. T. (2005). Quality control of acoustic Doppler velocimeter data in the surfzone. *Meas. Sci. Technol.*, 16(10):1889.

Enriquez, C., Mario-Tapia, I. J., and Herrera-Silveira, J. A. (2010). Dispersion in the Yucatan coastal zone: Implications for red tide events. *Continental Shelf Research*, 30(2):127–137.

Erikson, L., Larson, M., and Hanson, H. (2005). Prediction of swash motion and run-up including the effects of swash interaction. *Coastal Engineering*, 52(3):285–302.

Feddersen, F., Trowbridge, J. H., and Williams III, A. J. (2007). Vertical structure of dissipation in the nearshore. *Journal of Physical Oceanography*, 37(7):1764–1777.

Federico, S., Pasqualoni, L., Sempreviva, A. M., De Leo, L., Avolio, E., Calidonna, C. R., and Bellecci, C. (2010). The seasonal characteristics of the breeze circulation at a coastal Mediterranean site in South Italy. *Adv. Sci. Res.*, 4(1):47–56.

Goring, D. G. and Nikora, V. I. (2002). Despiking Acoustic Doppler Velocimeter Data. *Journal of Hydraulic Engineering*, 128(1):117–126.

Greenwood, B., Aagaard, T., and Nielsen, J. (2004). Swash Bar Morphodynamics in the Danish Wadden Sea: Sand Bed Oscillations and Suspended Sediment Flux during an Accretionary Phase of the Foreshore Cycle. *Geografisk Tidsskrift-Danish Journal of Geography*, 104(1):15–29.

Guard, P. A. and Baldock, T. E. (2006). The influence of seaward boundary conditions on swash zone hydrodynamics. *Coastal Engineering*, 54(4):321–331.

Guza, R. T. and Feddersen, F. (2012). Effect of wave frequency and directional spread on shoreline runup. *Geophysical Research Letters*, 39(11).

Guza, R. T. and Inman, D. L. (1975). Edge waves and beach cusps. *J. Geophys. Res.*, 80(21):2997–3012.

Guza, R. T. and Thornton, E. B. (1982). Swash oscillations on a natural beach. *J. Geophys. Res.*, 87(C1):483–491.

Hardisty, J. (1983). An assessment and calibration of formulations for Bagnold's bed-load equation. *Journal of Sedimentary Research*, 53(3):1007–1010.

Holland, K., Holman, R., Lippmann, T., Stanley, J., and Plant, N. (1997). Practical use of video imagery in nearshore oceanographic field studies. *IEEE Journal of Oceanic Engineering*, 22(1):81–92.

Holland, K. T. and Holman, R. A. (1993). The statistical distribution of swash maxima on natural beaches. *J. Geophys. Res.*, 98(C6):10271–10278.

Holland, K. T. and Holman, R. A. (1997). Video Estimation of Foreshore Topography Using Trinocular Stereo. *Journal of Coastal Research*, 13(1):81–87.

Holland, K. T. and Puleo, J. A. (2001). Variable swash motions associated with foreshore profile change. *J. Geophys. Res.*, 106(C3):4613–4623.

Holland, K. T., Raubenheimer, B., Guza, R. T., and Holman, R. A. (1995). Runup kinematics on a natural beach. *J. Geophys. Res.*, 100(C3):4985–4993.

Holman, R. A. (1986). Extreme value statistics for wave run-up on a natural beach. *Coastal Engineering*, 9(6):527–544.

Holman, R. A. and Sallenger, A. H. (1985). Setup and swash on a natural beach. *J. Geophys. Res.*, 90(C1):945–953.

Holman, R. A. and Stanley, J. (2007). The history and technical capabilities of Argus. *Coastal Engineering*, 54(67):477–491.

Horn, D. P. and Mason, T. (1994). Swash zone sediment transport modes. *Marine Geology*, 120(34):309–325.

Houser, C. and Barrett, G. (2009a). Bed Elevation Changes in the Upper-Swash Zone. *Journal of Coastal Research*, pages 64–68.

Houser, C. and Barrett, G. (2009b). Bed elevation changes in the upper-swash zone. *J. Coast. Res. Journal of Coastal Research*, (SPEC. ISSUE 56):64–68.

Houser, C. and Barrett, G. (2010). Divergent behavior of the swash zone in response to different foreshore slopes and nearshore states. *Marine Geology*, 271(12):106–118.

Houser, C. and Greenwood, B. (2007). Onshore Migration of a Swash Bar during a Storm. *Journal of Coastal Research*, 23(1):1–14.

Hsu, T.-J. and Hanes, D. M. (2004). Effects of wave shape on sheet flow sediment transport. *Journal of Geophysical Research*, 109(C05025).

Hsu, T.-J. and Raubenheimer, B. (2006). A numerical and field study on inner-surf and swash sediment transport. *Continental Shelf Research*, 26(5):589–598.

Hughes, M. G., Aagaard, T., and Baldock, T. E. (2007). Suspended Sediment in the Swash Zone: Heuristic Analysis of Spatial and Temporal Variations in Concentration. *Journal of Coastal Research*, pages 1345–1354.

Hughes, M. G., Aagaard, T., Baldock, T. E., and Power, H. E. (2014). Spectral signatures for swash on reflective, intermediate and dissipative beaches. *Marine Geology*, 355:88–97.

Hughes, M. G. and Baldock, T. E. (2004). Eulerian flow velocities in the swash zone: Field data and model predictions. *J. Geophys. Res.*, 109(C8):C08009.

Hughes, M. G., Masselink, G., and Brander, R. W. (1997). Flow velocity and sediment transport in the swash zone of a steep beach. *Marine Geology*, 138(12):91–103.

Hughes, M. G. and Moseley, A. S. (2007). Hydrokinematic regions within the swash zone. *Continental Shelf Research*, 27(15):2000–2013.

Hurther, D., Thorne, P. D., Bricault, M., Lemmin, U., and Barnoud, J.-M. (2011). A multi-frequency Acoustic Concentration and Velocity Profiler (ACVP) for boundary layer measurements of fine-scale flow and sediment transport processes. *Coastal Engineering*, 58(7):594–605.

Inch, K., Masselink, G., Puleo, J. A., Russell, P., and Conley, D. C. (2015). Vertical structure of near-bed cross-shore flow velocities in the swash zone of a dissipative beach. *Continental Shelf Research*.

Inman, D. L. and Filloux, J. (1960). Beach Cycles Related to Tide and Local Wind Wave Regime. *The Journal of Geology*, 68(2):225–231.

Iribarren, R. and Nogales, M. (1949). Protection des ports. In *XVIIth International Navigation Congress, Section II, Communication*, pages 31–80.

Jackson, N. L., Masselink, G., and Nordstrom, K. F. (2004). The role of bore collapse and local shear stresses on the spatial distribution of sediment load in the uprush of an intermediate-state beach. *Marine Geology*, 203(12):109–118.

Jamal, M. H., Simmonds, D. J., and Magar, V. (2014). Modelling gravel beach dynamics with XBeach. *Coastal Engineering*, 89:20–29.

Kana, T. and Ward, L. (1980). Nearshore Suspended Sediment Load During Storm and Post-Storm Conditions. In *Coastal Engineering 1980*, pages 1158–1174. American Society of Civil Engineers.

Kelly, D. M. and Dodd, N. (2010). Beach-face evolution in the swash zone. *Journal of Fluid Mechanics*, 661:316–340.

Kikkert, G. A., O'Donoghue, T., Pokrajac, D., and Dodd, N. (2012). Experimental study of bore-driven swash hydrodynamics on impermeable rough slopes. *Coastal Engineering*, 60:149–166.

Kikkert, G. A., Pokrajac, D., O'Donoghue, T., and Steenhauer, K. (2013). Experimental study of bore-driven swash hydrodynamics on permeable rough slopes. *Coastal Engineering*, 79:42–56.

Kobayashi, N. and Johnson, B. D. (2001). Sand suspension, storage, advection, and settling in surf and swash zones. *J. Geophys. Res.*, 106(C5):9363–9376.

Komar, P. D. (1976). *Beach processes and sedimentation*. Prentice-Hall, Englewood Cliffs, N.J. OCLC: 1975318.

Kulkarni, C. D., Levoy, F., Monfort, O., and Miles, J. (2004). Morphological variations of a mixed sediment beachface (Teignmouth, UK). *Continental Shelf Research*, 24(11):1203–1218.

Lanckriet, T., Puleo, J., and Waite, N. (2013). A Conductivity Concentration Profiler for Sheet Flow Sediment Transport. *IEEE Journal of Oceanic Engineering*, 38(1):55–70.

Lanckriet, T. and Puleo, J. A. (2013). Near-bed turbulence dissipation measurements in the inner surf and swash zone. *J. Geophys. Res. Oceans*, 118(12):6634–6647.

Lanckriet, T. and Puleo, J. A. (2015). A semianalytical model for sheet flow layer thickness with application to the swash zone. *J. Geophys. Res. Oceans*, 120(2):1333–1352.

Lanckriet, T., Puleo, J. A., Masselink, G., Turner, I., Conley, D., Blenkinsopp, C., and Russell, P. (2014). Comprehensive Field Study of Swash-Zone Processes. II: Sheet Flow Sediment Concentrations during Quasi-Steady Backwash. *Journal of Waterway, Port, Coastal, and Ocean Engineering*, 140(1):29–42.

Longo, S., Petti, M., and Losada, I. J. (2002). Turbulence in the swash and surf zones: a review. *Coastal Engineering*, 45(34):129–147.

MacVicar, B. J., Beaulieu, E., Champagne, V., and Roy, A. G. (2007). Measuring water velocity in highly turbulent flows: field tests of an electromagnetic current meter (ECM) and an acoustic Doppler velocimeter (ADV). *Earth Surface Processes and Landforms*, 32:1412–1432.

Malarkey, J., Davies, A. G., and Li, Z. (2003). A simple model of unsteady sheet-flow sediment transport. *Coastal Engineering*, 48(3):171–188.

Masselink, G. (1998). The effect of sea breeze on beach morphology, surf zone hydrodynamics and sediment resuspension. *Marine Geology*, 146(14):115–135.

Masselink, G., Evans, D., Hughes, M. G., and Russell, P. (2005). Suspended sediment transport in the swash zone of a dissipative beach. *Marine Geology*, 216(3):169–189.

Masselink, G. and Hughes, M. (1998). Field investigation of sediment transport in the swash zone. *Continental Shelf Research*, 18(10):1179–1199.

Masselink, G. and Pattiaratchi, C. B. (2001). Seasonal changes in beach morphology along the sheltered coastline of Perth, Western Australia. *Marine Geology*, 172(34):243–263.

Masselink, G. and Puleo, J. A. (2006). Swash-zone morphodynamics. *Continental Shelf Research*, 26(5):661–680.

Masselink, G. and Russell, P. (2005). Field Measurements of Flow Velocities on a Dissipative and Reflective Beach Implications for Swash Sediment Transport. In *Coastal Dynamics 2005*, pages 1–13. American Society of Civil Engineers.

Masselink, G. and Russell, P. (2006). Flow velocities, sediment transport and morphological change in the swash zone of two contrasting beaches. *Marine Geology*, 227(34):227–240.

Masselink, G., Russell, P., Blenkinsopp, C., and Turner, I. (2010). Swash zone sediment transport, step dynamics and morphological response on a gravel beach. *Marine Geology*, 274(14):50–68.

Masselink, G., Russell, P., Turner, I., and Blenkinsopp, C. (2009). Net sediment transport and morphological change in the swash zone of a high-energy sandy beach from swash event to tidal cycle time scales. *Marine Geology*, 267(12):18–35.

Meyer-Peter, E. and Müller, R. (1948). Formulas for Bed-Load transport. Stockhold, Sweden.

Mihoubi, M. K., Blorgey, M., and Kettab, A. (2012). Determination of the interstitial velocity field in the swash zone by Ultrasonic Doppler Velocimetry (UDV). *Comptes Rendus Geoscience*, 344(5):312–318.

Miles, J., Butt, T., and Russell, P. (2006). Swash zone sediment dynamics: A comparison of a dissipative and an intermediate beach. *Marine Geology*, 231(14):181–200.

Mohrholz, V., Prandke, H., and Lass, H. U. (2008). Estimation of TKE dissipation rates in dense bottom plumes using a Pulse Coherent Acoustic Doppler Profiler (PC-ADP)Structure function approach. *Journal of Marine Systems*, 70(3):217–239.

Mori, N., Suzuki, T., and Kakuno, S. (2007). Noise of Acoustic Doppler Velocimeter Data in Bubbly Flows. *Journal of Engineering Mechanics*, 133(1):122–125.

Mory, M., Abadie, S., Mauriet, S., and Lubin, P. (2011). Run-up flow of a collapsing bore over a beach. *European Journal of Mechanics - B/Fluids*, 30(6):565–576.

Nielsen, P. (2002). Shear stress and sediment transport calculations for swash zone modelling. *Coastal Engineering*, 45(1):53–60.

O'Donoghue, T., Pokrajac, D., and Hondebrink, L. J. (2010). Laboratory and numerical study of dambreak-generated swash on impermeable slopes. *Coastal Engineering*, 57(5):513–530.

O'Donoghue, T. and Wright, S. (2004). Concentrations in oscillatory sheet flow for well sorted and graded sands. *Coastal Engineering*, 50(3):117–138.

Othman, I. K., Baldock, T. E., and Callaghan, D. P. (2014). Measurement and modelling of the influence of grain size and pressure gradient on swash uprush sediment transport. *Coastal Engineering*, 83:1–14.

Packwood, A. R. (1983). The influence of beach porosity on wave uprush and backwash. *Coastal Engineering*, 7(1):29–40.

Pattiaratchi, C., Hegge, B., Gould, J., and Eliot, I. (1997). Impact of sea-breeze activity on nearshore and foreshore processes in southwestern Australia. *Continental Shelf Research*, 17(13):1539–1560.

Pedrozo-Acuna, A., de Alegra-Arzaburu, A. R., Torres-Freyermuth, A., Mendoza, E., and Silva, R. (2011). Laboratory investigation of pressure gradients induced by plunging breakers. *Coastal Engineering*, 58(8):722–738.

Pedrozo-Acuna, A., Simmonds, D. J., Otta, A. K., and Chadwick, A. J. (2006). On the cross-shore profile change of gravel beaches. *Coastal Engineering*, 53(4):335–347.

Peregrine, D. H. and Williams, S. M. (2001). Swash overtopping a truncated plane beach. *Journal of Fluid Mechanics*, 440:391–399.

Petti, M. and Longo, S. (2001). Turbulence experiments in the swash zone. *Coastal Engineering*, 43(1):1–24.

Petti, M., Longo, S., and others (2001). Hydrodynamics in the swash zone. *International Journal of Offshore and Polar Engineering*, 11(03).

Pintado-Patiño, J. C., Torres-Freyermuth, A., Puleo, J. A., and Pokrajac, D. (2015). On the role of infiltration and exfiltration in swash zone boundary layer dynamics. *J. Geophys. Res. Oceans*.

Pope, S. B. (2000). *Turbulent Flows*. Cambridge University Press, Cambridge ; New York, 1st edition.

Postacchini, M., Othman, I. K., Brocchini, M., and Baldock, T. E. (2014). Sediment transport and morphodynamics generated by a dam-break swash uprush: Coupled vs uncoupled modeling. *Coastal Engineering*, 89:99–105.

Pritchard, D. (2009). Sediment transport under a swash event: the effect of boundary conditions. *Coastal Engineering*, 56(9):970–981.

Pritchard, D. and Hogg, A. J. (2005). On the transport of suspended sediment by a swash event on a plane beach. *Coastal Engineering*, 52(1):1–23.

Puleo, J. A. (2009). Tidal variability of swash-zone sediment suspension and transport. *Journal of Coastal Research*, 25(4):937–948.

Puleo, J. A., Beach, R. A., Holman, R. A., and Allen, J. S. (2000). Swash zone sediment suspension and transport and the importance of bore-generated turbulence. *J. Geophys. Res.*, 105(C7):17021–17044.

Puleo, J. A., Blenkinsopp, C., Conley, D., Masselink, G., Turner, I., Russell, P., Buscombe, D., Howe, D., Lanckriet, T., McCall, R., and Poate, T. (2014a). Comprehensive Field Study of Swash-Zone Processes. I: Experimental Design with Examples of Hydrodynamic and Sediment Transport Measurements. *Journal of Waterway, Port, Coastal, and Ocean Engineering*, 140(1):14–28.

Puleo, J. A. and Butt, T. (2006). The first international workshop on swash-zone processes. *Continental Shelf Research*, 26(5):556–560.

Puleo, J. A., Farhadzadeh, A., and Kobayashi, N. (2007). Numerical simulation of swash zone fluid accelerations. *J. Geophys. Res.*, 112(C7):C07007.

Puleo, J. A., Farquharson, G., Frasier, S. J., and Holland, K. T. (2003a). Comparison of optical and radar measurements of surf and swash zone velocity fields. *J. Geophys. Res.*, 108(C3):3100.

Puleo, J. A. and Holland, K. T. (2001). Estimating swash zone friction coefficients on a sandy beach. *Coastal Engineering*, 43(1):25–40.

Puleo, J. A., Holland, K. T., Plant, N. G., Slinn, D. N., and Hanes, D. M. (2003b). Fluid acceleration effects on suspended sediment transport in the swash zone. *J. Geophys. Res.*, 108(C11):3350.

Puleo, J. A., Johnson, R. V., Butt, T., Kooney, T. N., and Holland, K. T. (2006). The effect of air bubbles on optical backscatter sensors. *Marine Geology*, 230(12):87–97.

Puleo, J. A., Lanckriet, T., and Blenkinsopp, C. (2014b). Bed level fluctuations in the inner surf and swash zone of a dissipative beach. *Marine Geology*, 349:99–112.

Puleo, J. A., Lanckriet, T., Conley, D., and Foster, D. (2015). Sediment transport partitioning in the swash zone of a large-scale laboratory beach. *Coastal Engineering*.

Puleo, J. A., Lanckriet, T., and Wang, P. (2012). Near bed cross-shore velocity profiles, bed shear stress and friction on the foreshore of a microtidal beach. *Coastal Engineering*, 68:6–16.

Puleo, J. A. and Torres-Freyermuth, A. (2016). The second international workshop on swash-zone processes. *Coastal Engineering*, 115:1–7.

Raubenheimer, B. (2002). Observations and predictions of fluid velocities in the surf and swash zones. *J.Geophys.Res.*, 107(C11):3190.

Raubenheimer, B., Elgar, S., and Guza, R. T. (2004). Observations of swash zone velocities: A note on friction coefficients. *J. Geophys. Res.*, 109(C1):C01027.

Roy, A. G., Biron, P. M., and Lapointe, M. F. (1997). Implications of low-pass filtering on power spectra and autocorrelation functions of turbulent velocity signals. *Math Geol*, 29(5):653–668.

Ruessink, B. G., Blenkinsopp, C., Brinkkemper, J. A., Castelle, B., Dubarbier, B., Grasso, F., Puleo, J. A., and Lanckriet, T. (2016). Sandbar and beach-face evolution on a prototype coarse sandy barrier. *Coastal Engineering*, 113:19–32.

Ruessink, B. G., Kleinhans, M. G., and van den Beukel, P. G. L. (1998). Observations of swash under highly dissipative conditions. *J. Geophys. Res.*, 103(C2):3111–3118.

Ruggiero, P., Holman, R. A., and Beach, R. A. (2004). Wave run-up on a high-energy dissipative beach. *J. Geophys. Res.*, 109(C6):C06025.

Ruju, A., Conley, D., Masselink, G., and Puleo, J. (2016). Sediment transport dynamics in the swash zone under large-scale laboratory conditions. *Continental Shelf Research*, 120:1–13.

Ruju, A., Lara, J. L., and Losada, I. J. (2014). Numerical analysis of run-up oscillations under dissipative conditions. *Coastal Engineering*, 86:45–56.

Russell, P., Masselink, G., Blenkinsopp, C., and Turner, I. (2009). A Comparison of Berm Accretion in the Swash Zone on Sand and Gravel Beaches at the Timescale of Individual Waves. *Journal of Coastal Research*, pages 1791–1795.

Senechal, N., Coco, G., Bryan, K. R., and Holman, R. A. (2011). Wave runup during extreme storm conditions. *J. Geophys. Res.*, 116(C7):C07032.

Shanehsazzadeh, A. and Holmes, P. (2007). Field investigation on the results of non-linear shallow water equations in the Swash Zone. *Coastal Engineering*, 54(11):835–855.

Shi, F., Kirby, J. T., Harris, J. C., Geiman, J. D., and Grilli, S. T. (2012). A high-order adaptive time-stepping TVD solver for Boussinesq modeling of breaking waves and coastal inundation. *Ocean Modelling*, 4344:36–51.

Shin, S. and Cox, D. (2006). Laboratory observations of inner surf and swash-zone hydrodynamics on a steep slope. *Continental Shelf Research*, 26(5):561–573.

Smith, N. D. and Rogers, J. (2009). *Fluvial Sedimentology VI (Special Publication 28 of the IAS)*. John Wiley & Sons.

Sonu, C. J., Murray, S. P., Hsu, S. A., Suhayda, J. N., and Waddell, E. (1973). Sea breeze and coastal processes. *Eos Trans. AGU*, 54(9):820–833.

Sou, I. M., Cowen, E. A., and Liu, P. L.-F. (2010). Evolution of the turbulence structure in the surf and swash zones. *Journal of Fluid Mechanics*, 644:193–216.

Sou, I. M. and Yeh, H. (2011). Laboratory study of the cross-shore flow structure in the surf and swash zones. *J. Geophys. Res.*, 116(C3):C03002.

Steenhauer, K., Pokrajac, D., O'Donoghue, T., and Kikkert, G. A. (2011). Subsurface processes generated by bore-driven swash on coarse-grained beaches. *J. Geophys. Res.*, 116(C4):C04013.

Stevens, C. and Coates, M. (1994). Applications of a maximised cross-correlation technique for resolving velocity fields in laboratory experiments. *J. of Hydraulic Res. Journal of Hydraulic Research*, 32(2):195–212.

Stockdon, H. F., Holman, R. A., Howd, P. A., and Sallenger Jr., A. H. (2006). Empirical parameterization of setup, swash, and runup. *Coastal Engineering*, 53(7):573–588.

Stockdon, H. F., Sallenger Jr., A. H., Holman, R. A., and Howd, P. A. (2007). A simple model for the spatially-variable coastal response to hurricanes. *Marine Geology*, 238(14):1–20.

Stoker, A. and Dodd, N. (2006). Evolution of Beach Cusps. In *Coastal Dynamics 2005*, pages 1–11, Barcelona, Spain. American Society of Civil Engineers.

Sumer, B. M., Kozakiewicz, A., Fredse, J., and Deigaard, R. (1996). Velocity and Concentration Profiles in Sheet-Flow Layer of Movable Bed. *Journal of Hydraulic Engineering*, 122(10):549–558.

Sumer, B. M., Sen, M. B., Karagali, I., Ceren, B., Fredse, J., Sottile, M., Zilioli, L., and Fuhrman, D. R. (2011). Flow and sediment transport induced by a plunging solitary wave. *J. Geophys. Res.*, 116(C1):C01008.

Svendsen, I. A. (1987). Analysis of surf zone turbulence. *J. Geophys. Res.*, 92(C5):5115–5124.

Svendsen, I. A., Madsen, P. A., and Hansen, J. B. (1978). Waves characteristics in the surf zone. volume 1, pages 520–539.

Svendsen, I. A., Veeramony, J., Bakunin, J., and Kirby, J. T. (2000). The flow in weak turbulent hydraulic jumps. *Journal of Fluid Mechanics*, 418:25–57.

Swart, D. H., Bijker, E. W., TU Delft: Civil Engineering and Geosciences, and TU Delft, Delft University of Technology (1974). Offshore sediment transport and equilibrium beach profiles.

Tehranirad, B., Shi, F., Kirby, J. T., Harris, J. C., and Grilli, S. T. (2011). Tsunami benchmark results for fully nonlinear Boussinesq wave model FUNWAVE-TVD. Technical report, Version 1.0. Technical report, No. CACR-11-02, Center for Applied Coastal Research, University of Delaware.

Tinker, J., OHare, T., Masselink, G., Butt, T., and Russell, P. (2009). A cross-shore suspended sediment transport shape function parameterisation for natural beaches. *Continental Shelf Research*, 29(16):1948–1960.

Torres-Freyermuth, A., Puleo, J. A., DiCosmo, N., Allende-Arandia, M., Chardón-Maldonado, P., Lopez, J., and Figueroa, B. (2016). Nearshore circulation on a sea breeze dominated beach during intense wind events. *In Preparation*.

Trowbridge, J. and Elgar, S. (2001). Turbulence Measurements in the Surf Zone. *Journal of Physical Oceanography*, 31(8):2403–2417.

Turner, I. L. and Masselink, G. (1998). Swash infiltration-exfiltration and sediment transport. *J. Geophys. Res.*, 103(C13):30813–30824.

Turner, I. L., Russell, P. E., and Butt, T. (2008). Measurement of wave-by-wave bed-levels in the swash zone. *Coastal Engineering*, 55(12):1237–1242.

van der Zanden, J., Alsina, J. M., Caceres, I., Buijsrogge, R. H., and Ribberink, J. S. (2015). Bed level motions and sheet flow processes in the swash zone: Observations with a new conductivity-based concentration measuring technique (CCM+). *Coastal Engineering*, 105:47–65.

van Rijn, L. C. (2007). *Manual sediment transport measurements in rivers, estuaries and coastal seas*. Aqua publications.

Veron, F. and Melville, W. K. (1999). Pulse-to-pulse coherent Doppler measurements of waves and turbulence. *Journal of Atmospheric and Oceanic Technology*, 16(11):1580–1597.

Vousdoukas, M. I. (2012). Erosion/accretion patterns and multiple beach cusp systems on a meso-tidal, steeply-sloping beach. *Geomorphology*, 141142:34–46.

Vousdoukas, M. I. (2014). Observations of wave run-up and groundwater seepage line motions on a reflective-to-intermediate, meso-tidal beach. *Marine Geology*, 350:52–70.

Vousdoukas, M. I., Almeida, L. P. M., and Ferreira, . (2012). Beach erosion and recovery during consecutive storms at a steep-sloping, meso-tidal beach. *Earth Surf. Process. Landforms*, 37(6):583–593.

Vousdoukas, M. I., Kirupakaramoorthy, T., Oumeraci, H., de la Torre, M., Wbbold, F., Wagner, B., and Schimmels, S. (2014). The role of combined laser scanning and video techniques in monitoring wave-by-wave swash zone processes. *Coastal Engineering*, 83:150–165.

Vousdoukas, M. I., Wziatek, D., and Almeida, L. P. (2011). Coastal vulnerability assessment based on video wave run-up observations at a mesotidal, steep-sloped beach. *Ocean Dynamics*, 62(1):123–137.

Wang, Y.-H. and Yu, G.-H. (2007). Velocity and concentration profiles of particle movement in sheet flows. *Advances in Water Resources*, 30(5):1355–1359.

Weir, F. M., Hughes, M. G., and Baldock, T. E. (2006). Beach face and berm morphodynamics fronting a coastal lagoon. *Geomorphology*, 82(34):331–346.

Whipple, A. C. and Luettich Jr, R. A. (2009). A comparison of acoustic turbulence profiling techniques in the presence of waves. *Ocean dynamics*, 59(5):719–729.

Wiberg, P. L. and Smith, J. D. (1991). Velocity distribution and bed roughness in high-gradient streams. *Water Resour. Res.*, 27(5):825–838.

Wiles, P. J., Rippeth, T. P., Simpson, J. H., and Hendricks, P. J. (2006). A novel technique for measuring the rate of turbulent dissipation in the marine environment. *Geophys. Res. Lett.*, 33(21):L21608.

Wilson, K. C. (1987). Analysis of BedLoad Motion at High Shear Stress. *Journal of Hydraulic Engineering*, 113(1):97–103.

Wright, L. D. and Short, A. D. (1984). Morphodynamic variability of surf zones and beaches: A synthesis. *Marine Geology*, 56(14):93–118.

Yeh, H. H. and Ghazali, A. (1988). On bore collapse. *J. Geophys. Res.*, 93(C6):6930–6936.

Zhang, Q. and Liu, P. L. F. (2008). A numerical study of swash flows generated by bores. *Coastal Engineering*, 55(12):1113–1134.

Zhu, F. and Dodd, N. (2013). Net beach change in the swash zone: A numerical investigation. *Advances in Water Resources*, 53:12–22.

Zhu, F. and Dodd, N. (2015). The morphodynamics of a swash event on an erodible beach. *Journal of Fluid Mechanics*, 762:110–140.

Appendix

COPYRIGHT NOTES

Chapter 1 (*in part*) and Chapter 2 are reproduced and modified, with permission from Elsevier, from Chardón-Maldonado, P., Pintado-Patiño, J. C., and Puleo, J. A. (2016). Advances in swash-zone research: Small-scale hydrodynamic and sediment transport processes. Coastal Engineering, 115, 825. https:// doi.org/ 10.1016/ j.coastaleng.2015.10.008. Statement from Elsevier: